Deciphering the Mechanism of Action of the Proapoptotic Protein BOK

Dissertation

der Mathematisch-Naturwissenschaftlichen Fakultät

der Eberhard Karls Universität Tübingen

zur Erlangung des Grades eines

Doktors der Naturwissenschaften

(Dr. rer. nat.)

vorgelegt von

Raed Shalaby

aus Gharbeya, Ägypten

Tübingen

2023

Gedruckt mit Genehmigung der Mathematisch-Naturwissenschaftlichen Fakultät der Eberhard Karls Universität Tübingen.

Tag der mündlichen Qualifikation:	14.06.2023
Dekan:	Prof. Dr. Thilo Stehle
1. Berichterstatter/-in:	Prof. Dr. Ana Garcia-Saez
2. Berichterstatter/-in:	Prof. Dr. Thilo Stehle

Table of Contents

I. Acknowledgments **3**

II. Summary **4**

III. Deutsche Zusammenfassung **5**

IV. List of publications **7**

V. List of abbreviations **8**

1. Introduction **9**

Regulated Cell death 9

Apoptosis 9

BCL-2 proteins 10

BCL-2 proteins interaction network 11

BOK 12

BOK structure 13

BOK activity regulation 14

BOK and MCL-1 15

Non-Apoptotic Functions of BOK 16

Calcium Signaling 16

Mitochondrial Morphology 16

BOK and cancer 17

Single-molecule imaging of membrane proteins 17

2. Objectives of the thesis **19**

Objective 1 19

Objective 2 20

3. Results **21**

3.1. Visualization of BOK pores independent of BAX and BAK reveals a similar mechanism with differing regulation 21

3.2. DeepSinse: deep learning-based detection of single molecules 22

3.3. Systematic Assessment of the Accuracy of Subunit Counting in Biomolecular Complexes Using Automated Single-Molecule Brightness Analysis 23

4. Discussion **24**

The BCL-2 effectors 24

Is BOK a true BCL-2 effector? 24

How BOK thermostability is linked to pore formation? 25

The interaction between BOK and cBID 26

The topology of BOK-induced pores 27

The mechanism of BOK oligomerization 28

Pro-apoptotic activity of BOK 28

BOK limited mitochondrial localization and its activity regulation 29
BOK assemblies revealed by super-resolution microscopy 30

5. References **31**

6. Appendix **38**
Accepted publications 38

I. Acknowledgments

First, I would like to express my sincere gratitude to my supervisor, Prof. Dr. Ana Garcia-Saez for giving me the opportunity to work on this project. She was always there when I needed her support, reviewing my progress constantly, and guiding me through my PhD thesis. Her support, monitoring and suggestions were invaluable. Also, I must thank all my current and past lab colleagues (in Tübingen and Köln) for the great working environment in the lab. I would like to thank Katia Cosentino for her support and guidance during my first year of PhD. Special thanks to Uris Ros for her help and support. I would also like to extend my thanks to John Danial for his help and suggestions. I would deeply express my thanks to Hector Flores-Romero for all the great time we had in the lab. I want to thank Arzoo Diwan for helping me with the experiments in cells. My work would not be possible without the assistance of Sabine, Caroline, Julia and Annika. They have been really supportive with all the technical and administrative stuff. Furthermore, I would like to thank the CECAD imaging facility for their continuous help with light and electron microscopy experiments. I want to give my deepest appreciation to my wife for her patience and encouragement. I cannot forget to thank my family and friends for all the unconditional support during my PhD years. Finally, many thanks to all participants that took part in the study and enabled this research to be possible.

II. Summary

BCL-2 family members are the main regulators of the mitochondrial pathway of apoptosis. The Bcl-2 family includes both pro-apoptotic and pro-survival proteins. The proapoptotic effectors BAX and BAK oligomerize upon activation to form pores in the mitochondrial outer membrane which is regarded as the point-of-no-return in intrinsic apoptosis. BOK is a poorly understood member of the BCL-2 family of proteins which is classified as a pro-apoptotic protein based on structural homology and the ability to induce apoptosis upon overexpression. BOK is currently proposed to function as a pro-apoptotic BAX-like effector, even if the molecular mechanism and structural properties of BOK pores are still unclear. In contrast to most BCL-2 proteins which are localized to the mitochondria, BOK is mainly localized to the membranes of the endoplasmic reticulum (ER) and the Golgi apparatus. BOK is also known to be overexpressed in several types of cancer, including ovarian cancer and cervical cancer, and is being studied as a potential cancer prognostic marker. In the present work, we directly visualized BOK-induced pores in liposomes using negative staining electron microscopy. The pores were similar to the ones induced by BAX, which suggests that both proteins have related oligomerization properties. This was also backed by single-molecule imaging, which demonstrated that BOK can oligomerize in membranes containing cardiolipin. In addition, we found that the thermal stability of BOK can explain its pore-forming activity, in agreement with previous reports. We also found that BOK apoptotic activity is analogous to and independent of BAX and BAK, and unaffected by other BCL-2 proteins. Interestingly, we show that apoptosis induction by BOK is restricted by its limited mitochondrial localization. Finally, Super resolution STED imaging was used to visualize BOK organization in apoptotic mitochondria, which appeared to form dots and ring-shaped assemblies, similar to what have been reported for BAX and BAK.

III. Deutsche Zusammenfassung

Die Mitglieder der BCL-2-Proteinfamilie sind die wichtigsten Regulatoren des mitochondrialen Apoptosewegs. Die Bcl-2-Familie umfasst sowohl pro- als auch anti-apoptotische Proteine. Die pro-apoptotischen Effektorproteine BAX und BAK oligomerisieren nach Aktivierung und bilden Poren in der äußeren Mitochondrienmembran, was als nicht umkehrbarer Schritt im intrinsischen Apoptose-Signalweg gilt. BOK ist ein weniger gut untersuchtes Mitglied der BCL-2-Proteinfamilie, das aufgrund struktureller Homologie und der Fähigkeit, bei Überexpression Apoptose auszulösen, als pro-apoptotisches Protein eingestuft wird. Derzeit wird angenommen, dass BOK als BAX-ähnliches Effektor-Protein fungiert, auch wenn der molekulare Mechanismus der Bildung sowie die strukturellen Eigenschaften von BOK-Poren noch unklar sind. Im Gegensatz zu den meisten BCL-2-Proteinen, welche in den Mitochondrien lokalisiert sind, ist BOK hauptsächlich an den Membranen des endoplasmatischen Retikulums (ER) und des Golgi-Apparats lokalisiert. Es ist bekannt, dass BOK bei verschiedenen Krebsarten, darunter Eierstockkrebs und Gebärmutterhalskrebs, überexprimiert ist, weshalb es mitunter als potenzieller prognostischer Marker für Krebs untersucht wird. In der vorliegenden Arbeit haben wir BOK-Poren in Liposomen mit Hilfe von Negativfärbung-Elektronenmikroskopie direkt sichtbar gemacht. Strukturell ähneln die Poren denen, die durch BAX gebildet werden, was auf vergleichbare Oligomerisierungseigenschaften beider Proteine bei der Porenbildung schließen lässt. Diese Beobachtung wurde zusätzlich durch Einzelmolekül-Mikroskopie bestätigt, welche zeigte, dass BOK in cardiolipinhaltigen Membranen oligomerisieren kann. In Übereinstimmung mit vorangegangenen Untersuchungen haben wir festgestellt, dass die porenbildende Aktivität von BOK durch dessen thermische Stabilität erklärt werden kann. Außerdem fanden wir heraus, dass die apoptotische Aktivität von BOK analog zu, jedoch unabhängig von BAX und BAK ist und von anderen BCL-2-Proteinen nicht beeinflusst wird. Interessanterweise konnten wir zeigen, dass die Fähigkeit von BOK, den apoptotischen Zelltod einzuleiten, durch dessen begrenzte mitochondriale Lokalisierung eingeschränkt ist. Schließlich wurde hochauflösende STED-Mikroskopie verwendet, um die molekulare Organisation von BOK in apoptotischen Mitochondrien zu visualisieren. Wir konnten zeigen, dass BOK

punktartige und ringförmige Anordnungen bildet, ähnlich derer, die für BAX und BAK beschrieben wurden.

IV. List of publications

1. **Shalaby R**, Flores-Romero H, García-Sáez AJ. The Mysteries around the BCL-2 Family Member BOK. Biomolecules. 2020 Dec 4;10(12):1638. doi: 10.3390/biom10121638. PMID: 33291826.

2. Danial JSH, **Shalaby R**, Cosentino K, Mahmoud MM, Medhat F, Klenerman D, Garcia Saez AJ. DeepSinse: deep learning based detection of single molecules. Bioinformatics. 2021 May 8:btab352. doi: 10.1093/bioinformatics/btab352. PMID: 33964131.

3. Danial JSH, Quintana Y, Ros U, **Shalaby R**, Margheritis EG, Chumpen Ramirez S, Ungermann C, Garcia-Saez AJ, Cosentino K. Systematic Assessment of the Accuracy of Subunit Counting in Biomolecular Complexes Using Automated Single-Molecule Brightness Analysis. J Phys Chem Lett. 2022 Jan 27;13(3):822-829. doi: 10.1021/acs.jpclett.1c03835. Epub 2022 Jan 19. PMID: 35044771.

4. **Shalaby R**, Diwan A, Flores-Romero H, Hertlein V, Garcia-Saez AJ. Visualization of BOK pores independent of BAX and BAK reveals a similar mechanism with differing regulation. Cell Death Differ. 2022 Oct 26:1–11. doi: 10.1038/s41418-022-01078-w. PMID: 36289446.

Book chapters

Jenner A, **Shalaby R**, Cosentino K. Quantitative single-molecule imaging of protein assembly in membranes. Advances in Biomembranes and Lipid Self-Assembly 31, 81-128

V. List of abbreviations

5-FU	5-Fluorouracil
AML	Acute myeloid leukemia
BCL-2	B-cell lymphoma-2
BH	BCL-2 homology
CLL	Chronic lymphocytic leukemia
CRC	Colorectal cancer
DISC	Death-inducing signaling complex
ERAD	ER-associated degradation
MEFs	Mouse Embryonic Fibroblasts
MOM	Mitochondrial outer membrane
MOMP	Mitochondrial outer membrane permeabilization
NMR	Nuclear magnetic resonance
NSCLC	Non-small-cell lung carcinoma
STED	Stimulated emission depletion
TMD	Transmembrane domain
TNF	Tumor necrosis factors

1. Introduction

Regulated Cell death

Cell death is not just an inevitable consequence of cellular life, but it also has the role of the targeted elimination of the less fit cells (Galluzzi et al. 2018). The process is central to homeostasis in multicellular life forms (Fuchs and Steller 2011; Galluzzi et al. 2016). For instance, cellular turnover rate in adult humans is estimated to be around 330 billion cells per day (Sender and Milo 2021). Therefore, a proper balance between cell proliferation and death must be established, especially in tissues with high turnover like the haematopoietic system and intestinal epithelium (Czabotar et al. 2014). In contrast to necrosis (accidental cell death that happens due to physical, chemical or mechanical insults), regulated cell death employs closely integrated signaling cascades and dedicated molecular machinery (Galluzzi et al. 2018). The classification of regulated cell death routes is continuously evolving, and it is getting more complicated as several cell death mechanisms have overlapping features (Kroemer et al. 2009). Currently, the most well-defined forms of regulated cell death are: apoptosis, ferroptosis, pyroptosis, autophagy and necroptosis (Cui et al. 2021).

Apoptosis

Apoptosis accounts for almost half of the cellular turnover in the human body, and is considered to be the best understood form of regulated cell death (Sender and Milo 2021). It is a highly orchestrated process that plays a pivotal role in physiological and pathological conditions (Wong 2011). The imbalance in apoptosis has been linked to various disorders, where downregulation is observed in cancer while excessive apoptosis can lead to degenerative diseases such as Alzheimer and Huntington disease (Ghavami et al. 2014). Apoptosis was first recognized based on morphological attributes: DNA fragmentation, blebbing of the plasma membrane, cell shrinkage and the formation of apoptotic bodies that wrap cell contents (Taylor et al. 2008). These apoptotic bodies are promptly cleared by nearby phagocytic cells and digested in their lysosomes. This process is very efficient and silent to avoid secondary necrosis, leading to a clean and non-inflammatory removal of unwanted cells (Szondy et al. 2017). Apoptosis can be triggered via two pathways: The

extrinsic and intrinsic. Extrinsic pathway is activated upon binding of tumor necrosis factors (TNF) to death receptors on the plasma membrane resulting in oligomerization of the death receptors to form the death-inducing signaling complex (DISC) leading to caspase 8 activation (Strasser et al. 2009). On the other hand, the intrinsic (or mitochondrial) pathway is triggered by internal cellular stress or damage and is controlled by the B-cell lymphoma-2 (BCL-2) family of proteins. Both pathways converge in the activation of the executioner caspases (caspase 3, 6, and 7), a family of proteases that cleaves various target proteins leading to the characteristic apoptotic breakdown of the cell (Miles and Hawkins 2017; Julien and Wells 2017).

BCL-2 proteins

The intrinsic pathway of apoptosis is regulated by the BCL-2 family proteins through a complex network of interactions in the cytosol and in the lipid membrane that determines cell fate (Kale et al. 2018). Therefore, they play an essential role in carcinogenesis and resistance to cancer treatment (Kalkavan and Green 2018; Flores-Romero and García-Sáez 2019). The BCL-2 family is a group of globular proteins that contain up to four BCL-2 homology (BH) domains. The mitochondrial outer membrane (MOM) is the main playground where most of the interactions between the BCL-2 proteins take place. The critical step of apoptotic induction is the mitochondrial outer membrane permeabilization (MOMP) which is regarded as the point of no return in apoptosis (Kalkavan and Green 2018). Secondary to MOMP, apoptotic factors (SMAC and cytochrome c) are released from the mitochondria to the cytosol leading to apoptosome formation, followed by the activation of executioner caspases (Bock and Tait 2020). In addition, the mitochondrial inner membrane is also permeabilized during apoptosis which allows the release of mitochondrial DNA, followed by the activation of an inflammatory response that is normally depressed by caspase activity (McArthur et al. 2018; Riley et al. 2018; Cosentino et al. 2022).

The BCL-2 family members are commonly classified based on their role in apoptosis into three groups: (1) the pro-apoptotic effectors (BAX, BAK, and BOK) which form pores in the MOM, (2) the anti-apoptotic (pro-survival) members (BCL-XL, BCL-W, BFL-1, BCL-2, MCL-1 and BCL-B) and (3) the BH3-only proteins (BID, BIK, BAD,

BMF, HRK, NOXA, BIM and PUMA). The BH3-only proteins act as "sensors" that detect cellular stress or damage and then activate the intrinsic apoptotic pathway. They exert their function either by activating the pro-apoptotic proteins (BAX and BAK) or by inhibiting the activity of the anti-apoptotic proteins. Interestingly, even if they have the complete opposite role in apoptosis, both pro-survival members and pro-apoptotic effectors share four BH domains (BH1-BH4) and fold into a similar globular structure which contains two hydrophobic helices (α5 and α6) forming a central hairpin structure surrounded by six amphipathic helices (Shamas-Din et al. 2013). This fold leads to the formation of a hydrophobic groove outlined by the helices α2–α5 which provides an important interface for the interactions with the BH3 domain of other family members (Bleicken et al. 2017). The localization of the BCL-2 proteins to the MOM is mainly driven by a C-terminal α-helical transmembrane domain (TMD), which acts as a membrane anchor (Wilfling et al. 2012; Czabotar et al. 2014). In addition, other functions are attributed to the TMDs such as: retrotranslocation of proapoptotic members to the cytosol, mitochondrial morphology and metabolism modulation (Edlich et al. 2011; Williams et al. 2016; Schulman et al. 2019; Lucendo et al. 2020). On the other hand, the majority of the BH3-only proteins are intrinsically disordered except for BID which has a fold similar to that of the multi-BH domain members (Chou et al. 1999; McDonnell et al. 1999; Hinds et al. 2007). Frequently, cancer cells exhibit upregulation of the prosurvival proteins leading to resistance against chemotherapy. For this, specific inhibitors of the anti-apoptotic proteins have been developed for the treatment of cancer (Campbell and Tait 2018; Montero and Letai 2018). The most important of these are the “BH3 mimetics” that are designed to bind to- and inhibit the pro-survival proteins, which lead to apoptosis induction in cancer cells (Townsend et al. 2021). Venetoclax is the only BH3-mimetic that has been approved by FDA to be used for the treatment of chronic lymphocytic leukemia (CLL) and acute myeloid leukemia (AML) in adults.

BCL-2 proteins interaction network

The BH3-only proteins have different affinities for binding to different pro-apoptotic and anti-apoptotic BCL-2 members. For example, BID has a higher binding affinity for BAX and BCL-xL, whereas BIM has a higher binding affinity for BAK and BCL-2 (Happo et al. 2012). When BID is cleaved by caspase 8, the active truncated form

with exposed BH3 domain (tBID) is released (Huang et al. 2016). Apoptosis is then triggered via two mechanisms: inhibition of the anti-apoptotic proteins or direct activation of pro-apoptotic effectors. In addition, the BH3-only proteins have differential selectivity towards different pro-survival proteins. This is due to structural differences in their BH3 domains and in the grooves of the pro-survival proteins (Czabotar et al. 2014). Apart from BH3-into-groove interactions, the modulation of BCL-2 proteins can be controlled through other non-canonical surfaces (N-terminal helix, rear binding site and anchoring tail) (Gavathiotis et al. 2008; Barclay et al. 2015). Upon activation, the pro-apoptotic effector proteins exhibit conformational changes that give rise to the membrane-bound form. This is believed to occur through TM dislodgement and N-terminal exposure followed by BH3 exposure and then further oligomerization in the membrane which leads to pore formation (Flores-Romero et al. 2020). The pores formed by BAX and BAK are now very well studied, and it is believed that both proteins can form toroidal pores of tunable size (Cosentino and García-Sáez 2017). Recently, it was reported that BAK can oligomerize faster than BAX to form lines, arcs, and rings, and it is able to recruit BAX to co-assemble into the same supra-molecular apoptotic structures (Cosentino et al. 2022).

BOK

BCL2-related ovarian killer (BOK) is a BCL-2 family member that was discovered using a yeast 2-hybrid screen of a rat ovarian fusion cDNA library, using MCL-1 protein as the bait (Hsu et al. 1997). BOK was first categorized as an effector pro-apoptotic protein as it, like BAX and BAK, contains the four BH motifs and induces apoptosis upon overexpression in cells. However, BOK has some distinctive characteristics that always made it clustered alone. The protein was shown to be widely expressed in different tissues with higher levels in reproductive tissues (Gao et al. 2005; Ke et al. 2012). Interestingly, BOK was found to have affinity to the pro-survival proteins MCL-1 and BFL-1, but not BCL-2 or BCL-XL (Inohara et al. 1998). In addition, the protein has an atypical subcellular distribution, where it localizes to the membranes of the ER more than mitochondria (Echeverry et al. 2013). In contrast to BAX and BAK, BOK is not induced by the BH3-only proteins and its mechanism of regulation has been always questioned. The first $BOK^{-/-}$ mice

were produced in 2012, and developed normally with no observed tissue anomalies (Ke et al. 2012). This indicated that BOK role overlaps with that of other BCL-2 family members or may have a function restricted to specific stress stimuli. BOK is becoming more accepted as a pro-apoptotic effector of the BCL-2 family due to the accumulation of evidence that support that BOK overexpression induces MOMP, caspase-3 activation, and apoptosis (Rodriguez et al. 2006; Llambi et al. 2016). It was also shown that recombinant BOK can permeabilize liposomes with a composition that mimics the mitochondrial outer membrane, like BAX and BAK (Fernández-Marrero et al. 2017). In that study, BOK pores were reported to be large enough to pass large molecules like cytochrome c (12 kDa) and allophycocyanin (104 kDa). Still, more detailed information about BOK oligomerization in the membrane is lacking.

BOK structure

The earliest structural information about BOK only emerged in 2018, and it provided some clue to the activity control of BOK. Two studies were published reporting BOK structure using both x-ray crystallography and nuclear magnetic resonance (NMR) (Zheng et al. 2018; Ke et al. 2018). In the x-ray crystallography study, chicken BOK was used and the first 18 residues and the C-terminal helix were removed to facilitate the protein production process. As expected, BOK structure was similar to the typical BCL-2 fold shared by BAX, BAK and the pro-survival members. However, the hydrophobic groove of BOK was partially obstructed by the residues Q92 and Q113 in one of the molecules in the asymmetric unit. Moreover, the B-factor values of the groove residues were higher than average, indicating larger flexibility in this region (Sun et al. 2019). The structure of BOK was also solved in the same year using NMR spectroscopy, and the additional structural information of BOK provided by this study further explained its auto-activation and the distinct pattern of binding to other BCL-2 family members (Zheng et al. 2018). This can be summarized into two factors: (1) an atypical hydrophobic groove architecture that hinders binding to BH3 domains of other proteins and (2) a glycine residue (G35) which acts as a helix breaker in the middle of the α1 helix. The hydrophobic groove is collapsed and made up of mostly loop structures which are believed to have high dynamics and conformational flexibility. The small hydrophobic pockets P0 and P1 are occluded by

the helix α3, limiting the access by the residues of the BH3 domain. In addition, the residue K122 has a less positive charge than the conserved arginine in all other BCL-2 family members and makes a less stable salt bridge with the conserved aspartate of the BH3 ligand. These attributes may reduce the affinity of the BH3-into-groove interaction of BOK. In addition, the glycine residue (G35) probably acts as a helix breaker in the α1 helix , leading to reduced stability of the protein fold (Zheng et al. 2018). This makes BOK more susceptible to the conformational changes required for the activation. To prove this, A BOK mutant G35A was produced and was shown to have significantly higher melting temperature and induced less permeabilization of liposomes than the wild type protein (Zheng et al. 2018). We have also noticed that GFP-BOK G35A is inducing apoptosis to less extent than GFP-BOK when expressed in HCT116 cells. All of these can give insights of the structural features of BOK that enables its permeabilizing activity without the need of activation by BH3-only proteins.

BOK activity regulation

For a long time, BAX and BAK were considered to be the only MOMP effectors of the mitochondrial apoptotic pathway. This was mainly because $BAX^{-/-}$ $BAK^{-/-}$ cells were not able to execute apoptosis upon exposure to many different apoptotic stimuli (Wang and Youle 2012). Still, BOK was clustered with the pro-apoptotic effectors because of the high sequence similarity to BAX and BAK but the exact role of BOK in apoptosis remained not fully understood, and until recently it was still debated if BOK can act as a MOMP effector (Moldoveanu and Czabotar 2020). In the early studies, BOK was shown to induce mitochondrial apoptosis upon transient overexpression in cells that contain BAX and BAK (Yakovlev et al. 2004; Rodriguez et al. 2006). In line with this, BOK-induced cell death was significantly reduced in the absence of BAX and BAK, which may point that BOK induces MOMP upstream of BAX/BAK (Echeverry et al. 2013; Carpio et al. 2015). In contrast to this, it was also reported that BOK is able to induce MOMP in $BAX^{-/-}$ $BAK^{-/-}$ cells, leading to apoptotic cell death, which indicates that BOK has a genuine effector role and is capable of executing the permeabilization (Einsele-Scholz et al. 2016; Zheng et al. 2018). Importantly, some of $BAX^{-/-}BAK^{-/-}$ mice could survive to adulthood with normal tissue morphology which means that either apoptosis is executed by another

protein or a different cell death pathway is compensating for apoptosis (Lindsten et al. 2000). Furthermore, the hypothesis that BOK can act like BAX was further supported when it was observed that $BOK^{-/-}BAX^{-/-}BAK^{-/-}$ mice had more severe defects and died earlier than $BAX^{-/-}BAK^{-/-}$ mice (Ke et al. 2018). Importantly, neither extrinsic apoptosis, necroptosis, pyroptosis or autophagy were upregulated in these mice.

Being not induced by cBID or inhibited by the pro-survival proteins, a model of BOK regulation has emerged that links ER stress to apoptosis (Carpio et al. 2015). According to this hypothesis, BOK has an inherent instability because of the residue G35 that acts as a helix breaker (Zheng et al. 2018). As a result, BOK has the capacity to spontaneously translocate to the mitochondrial membrane and to induce MOMP. BOK activity is then regulated via controlling the level of the protein in the cell via ER-associated degradation (ERAD) after ubiquitination. Upon ER stress, the proteasome function is compromised, leading to an increase in BOK levels and apoptosis induction. This model also conforms to the atypical subcellular localization of BOK to the ER and can partially explain the induction of apoptosis by ER stress (Urra et al. 2013; Chipuk and Luna-Vargas 2016). Upon knocking BOK out, cells had less ability to die with mitochondrial apoptosis induced by ER stress but no differences in response to staurosporine or ultraviolet irradiation were observed (Carpio et al. 2015). In other reports, BOK was detected in Mouse Embryonic Fibroblasts (MEFs) only upon treatment with proteasome inhibitors (Llambi et al. 2016). In the latter study, different lysine residues in BOK were identified to be ubiquitination sites. In summary, based on these studies, a hypothesis of BOK regulation was that BOK is continuously degraded by the ERAD system leading to undetected cellular levels. Upon ER stress, the ERAD system is saturated which results in BOK stabilization and subsequent translocation to the MOM to induce apoptosis.

BOK and MCL-1

When BOK was first discovered, it was shown that it interacts with MCL-1 and BFL-1, but not BCL-2 and BCL-XL (Hsu et al. 1997). In line with this, It was reported that MCL-1 can inhibit BOK proapoptotic activity (Stehle et al. 2018). However, other studies showed that the interaction between BOK and MCL-1 does not affect

BOK-mediated apoptosis (Llambi et al. 2016). A recent study has shown that BOK and MCL-1 form heterodimers via the TMD of both proteins in the mitochondrial membrane (Lucendo et al. 2020). They hypothesized that this interaction helps in the tethering of BOK TMD to the mitochondria. MCL-1 TMD was able to induce apoptosis upon transfection to $BAX^{-/-}BAK^{-/-}$ cells, and this effect was strongly reduced upon gene silencing of endogenous BOK indicating that MCL-1 TMD apoptosis induction is BOK dependent. Based on this, MCL-1 keeps a fraction of BOK in an off state at the mitochondria, waiting for the cell death signal.

Non-Apoptotic Functions of BOK

Apart from its contribution in the regulation of intrinsic apoptosis pathways, BOK has been found to be involved in other cellular processes. Some examples of these non-apoptotic roles are discussed below.

Calcium Signaling

Different BCL-2 proteins have been already linked to the regulation of calcium homeostasis (Hardwick and Soane 2013). As mentioned above, BOK has been shown to localize preferentially to the ER and Golgi (Ke et al. 2012). In the ER, BOK binds to inositol 1,4,5-trisphosphate receptors (IP3Rs), which are involved in intracellular calcium signaling (Ivanova et al. 2014). It was reported that the BH4 domain of BOK is a key mediator in the interaction with IP3R, as indicated by site-directed mutagenesis studies (Schulman et al. 2016). In a recent study, BOK was shown to potentiate ER-mitochondrial contact sites, and to act as an effector of IP3R-mediated calcium transfer from the ER to the mitochondria (Carpio et al. 2021). Accordingly, BOK can control apoptosis by calcium transfer through ER-mitochondrial contact sites.

Mitochondrial Morphology

The overall mitochondrial morphology is usually determined by two opposing processes: mitochondrial fusion and fission. It was found that the deletion of BOK gene leads to mitochondrial fragmentation in cultured MEFs (Schulman et al. 2019). The observed phenotype was a consequence of reduced fusion rate, and could be reversed by the stable expression of BOK. It is still questionable whether the effect of

BOK on mitochondrial morphology is direct or indirect. At least, it has been shown that this effect is not through IP3R (Schulman et al. 2019), but other possibilities are still to be investigated.

BOK and cancer

It was found that the genomic locus containing BOK gene is deleted in many types of human cancers, opening the possibility of using BOK as a cancer prognostic marker (Beroukhim et al. 2010a). Interestingly, among the pro-apoptotic family members, BOK was found to be one of the most frequently deleted genes in cancer cells (Naim and Kaufmann 2020). Apart from somatic copy-number variations, BOK was also shown to be epigenetically repressed in non-small-cell lung carcinoma (NSCLC) cell lines (Moravcikova et al. 2017). This may indicate that BOK has a tumor-suppressing function and can be used for estimating the prognosis of late-stage NSCLC patients where high BOK levels could predict longer patient survival (Fernandez-Marrero et al. 2018). In addition, BOK was reported to be downregulated in colorectal cancer (CRC) (Carberry et al. 2018). In this line, it was also shown that BOK-deficient CRC cells exhibit increased resistance to 5-Fluorouracil (5-FU) (Srivastava et al. 2019). This can be attributed to the ability of BOK to enhance the enzymatic activity of Uridine monophosphate synthase (UMPS), which is important for the conversion of 5-FU into its active metabolites. However, in other cancers, a high level of BOK expression was correlated with reduced survival and disease recurrence (Beroukhim et al. 2010b). This means that BOK has complex roles in tumor establishment and recurrence, as it is involved in various cell regulation processes in addition to apoptosis (Shalaby et al. 2020).

Single-molecule imaging of membrane proteins

Studying the mechanisms of protein complexes assembly is important for understanding their structure and function. This requires gaining information at the single-molecule level, as many processes are overlooked by ensemble measurements. Membrane proteins are involved in many key biological processes such as ion channels, receptors and pore forming proteins (Cournia et al. 2015). The latters, including BOK, are central to the execution of regulated cell death pathways. For studying the behavior of these proteins, it is advantageous to perform the

characterization in the native membrane environment. For doing this, the protein has to be produced in good yield and purity followed by fluorescent labeling. The membrane systems should be chosen to mimic the biological membrane under investigation, and an appropriate way to reconstitute the protein into the membrane is normally followed. Using single-molecule imaging for stoichiometry determination yields relevant information on the mechanism of action of membrane protein complexes. This has been possible because of a number of methodological improvements (novel fluorophores having bright and photostable emission, new labeling methods and advances in the field of microscopy). The technique has been previously applied for studying the mechanism of BAX oligomerization in the membrane environment (Subburaj et al. 2015). When the protein is incubated at the right concentration, particles can be visualized as diffraction-limited isolated spots which are bigger in size than the real structure. However, it is possible to measure their intensity and localize them with acceptable accuracy. Different algorithms can be then utilized to detect single molecules followed by fitting the intensity to a 2D Gaussian. The brightness of the particle is measured from the area under the 2D Gaussian followed by background subtraction. Afterwards, the brightness values of all detected particles can be used for the determination of subunit stoichiometry.

2. Objectives of the thesis

Objective 1

Until now, BOK continues to be an enigmatic member of the BCL-2 family. Controversial reports emerged in recent years which provided puzzling results regarding the ability of BOK to act as a pro-apoptotic effector. The role of BOK in apoptosis remains difficult to identify as it is not activated with typical intrinsic apoptotic inducers that converge in BAX and BAK mediated MOMP. BOK has been shown to induce pore formation in liposomes with a composition that mimics the mitochondrial outer membrane. These pores were large, stable and toroidal in nature, but direct visualization is still lacking. There is still to be known about the behavior of BOK in the membrane environment and its ability to oligomerize for pore formation. This will provide more information about the exact position of BOK among the BCL-2 proteins and the mechanisms of the regulation of its activity. Here, we wanted to investigate if BOK can act as a MOMP effector like BAX and BAK. To evaluate this, these are the aims of my thesis:

1. To characterize the relationship between the thermostability of BOK and its pore forming activity in liposomes.
2. To directly visualize the pores induced by BOK in liposomes and compare it with BAX-induced pores.
3. To study the oligomerization mechanism of BOK in supported lipid bilayers using single-molecule microscopy.
4. To study the proapoptotic activity of BOK in cells and to find out if it is dependent on BAX and BAK, and to investigate how the proapoptotic activity of BOK is regulated and how it is related to its intracellular localization.
5. To characterize BOK assemblies in the mitochondria of apoptotic cells using super-resolution microscopy.

Objective 2

Single-molecule imaging is a powerful tool especially in the field of membrane proteins. Our objective was to develop a fully automated pipeline for the accurate detection of single molecules of fluorescently-labeled proteins in the membrane environment, followed by the subunit counting to decipher the stoichiometry of the oligomeric species. To reduce bias, the method needs to be performed with minimal human intervention. In addition, it is important to make sure that the method is fast and can function accurately at low signal to noise ratios. To accomplish this, I have contributed to two publications that had the following aims:

1. To develop a trainable deep neural network for the detection of single molecules (Deepsinse).
2. To build a pipeline for the subunit counting of biomolecular complexes using single-molecule brightness analysis.

3. Results

3.1. Visualization of BOK pores independent of BAX and BAK reveals a similar mechanism with differing regulation

Raed Shalaby, Arzoo Diwan, Hector Flores-Romero, Vanessa Hertlein & Ana J. Garcia-Saez

Cell Death and Differentiation. 2022 Oct 26:1–11. doi: 10.1038/s41418-022-01078-w.

3.1.1. Synopsis

In this paper, we aimed to gain more insights about the poorly understood protein BOK. We have performed direct visualization of BOK-induced pores in liposomes using negative staining EM. The pores were similar to the ones formed by BAX. We observed that the C-terminal tail of BOK is related to its thermal stability and pore forming activity. Using single molecule imaging, we quantified the stoichiometry of BOK particles in the membrane, which was also in line with previous reports about BAX oligomerization. We have studied the regulation of BOK proapoptotic activity and found it to be independent of other BCL-2 proteins. Interestingly, BOK activity appeared to be controlled by limiting its localization to the mitochondria. In addition, we used super-resolution STED imaging to visualize BOK assemblies in cells. It revealed that BOK forms dots and ring-shaped particles in the apoptotic mitochondria. In summary, the results of this paper propose that BOK is a genuine MOMP effector like BAX and BAK, but it is controlled by its subcellular localization instead of interaction with BCL-2 family members.

3.1.2. Own contribution

I designed and performed all the experiments with the help of my colleagues. I estimate my contribution at 70%.

3.2. DeepSinse: deep learning-based detection of single molecules

John S H Danial, **Raed Shalaby**, Katia Cosentino, Marwa M Mahmoud, Fady Medhat, David Klenerman & Ana J Garcia Saez

Bioinformatics, Volume 37, Issue 21, 1 November 2021, Pages 3998–4000

3.2.1. Synopsis

In this paper, we have developed a trainable neural network for the detection of single molecules (DeepSinse), which can be applied to a wide range of signal-to-noise ratios. To construct the training dataset, images of 200 by 200 pixels in size were generated with 100 particles randomly scattered. The particles appeared as bursts which were convoluted with a 2D Gaussian Kernel. Images that contain bursts were simulated with the intensities ranging from 50 to 100 counts which gives signal-to-noise ratios from 24.85 to 45.81. From each image, ROIs were extracted and intensity was scaled between 0 and 1. The network was validated on the detection of single particles in experimental data and simulations. The accuracy of the network to detect single molecules was tested on experimental and simulated data. DeepSinse proved to have 4-5 times lower false positive and negative rates compared to available domain specific detection software. The speed of the network was tested on a mid-class Graphical Processing Unit (GPU), and was capable of being trained using 10,000 ROIs for 12 s. Using the same GPU, the network needs 40 s for processing 1000 frames which are 200 by 200 pixels in size.

3.2.2. Own contribution

I performed the experiments to test and validate the code and contributed to writing the manuscript. I estimate my contribution at 30%.

3.3. Systematic Assessment of the Accuracy of Subunit Counting in Biomolecular Complexes Using Automated Single-Molecule Brightness Analysis

John S. H. Danial, Yuri Quintana, Uris Ros, **Raed Shalaby**, Eleonora G. Margheritis, Sabrina Chumpen Ramirez, Christian Ungermann, Ana J. Garcia-Saez, & Katia Cosentino.

J Phys Chem Lett. 2022 Jan 27;13(3):822-829. doi: 10.1021/acs.jpclett.1c03835.

3.3.1. Synopsis

The aim of this paper was to establish a computational pipeline for the accurate quantification of the stoichiometry of biomolecular complexes imaged by fluorescence microscopy. To accomplish this, we developed an automated software (Stoichiometry Analysis Software or SAS) for single-molecule brightness analysis. The pipeline was then employed to quantify the accuracy of subunit counting using simulated and experimentally obtained data. Subunit counting is commonly performed either by stepwise photobleaching step counting or single-molecule brightness analysis. The latter approach has the advantage of applicability on a wide range of macromolecular complex sizes (stepwise counting is limited to about five subunits). The software uses a simple parameter-free algorithm for single-molecule particle detection, based on the DeepSinse neural network. SAS uses the calibration dataset for finding the brightness values of monomeric species. These data are then used to construct a Gaussian mixture that represents the distribution of the higher-order oligomeric species. The software achieves accuracy of counting above 85%, when applied on complex stoichiometric configurations.

3.3.2. Own contribution

I contributed to the assessment of the accuracy of the pipeline on experimentally-obtained and simulated data, and in writing the manuscript. I estimate my contribution at 10%.

4. Discussion

The BCL-2 effectors

Mitochondrial poration is the key step of intrinsic apoptosis, which leads to the release of caspase activators to the cytosol. This is executed by the effector BCL-2 family proteins (BAX, BAK and BOK) (Moldoveanu and Czabotar 2020). These proteins have different mechanisms of regulation, manifested in their subcellular localization and differential affinity to other BCL-2 proteins. BAX and BAK are commonly called the canonical effectors, and have been extensively studied over the past years. Still, as the apoptotic pores have not been isolated, direct investigation of the mechanism of assembly and pore formation is not complete (Moldoveanu 2023). Both canonical effectors are found in dormant conformation in normal conditions, waiting for activation by cellular stress signals. This leads to the translocation of BAX to the mitochondrial outer membrane (BAK is consistently localized on the mitochondria), followed by conformational changes (release of the α1 helix, exposure of BH3 domain and disengagement of core (α2–α5) from latch (α6–α8) regions) that allow pore formation (Llambi et al. 2011; Czabotar et al. 2013). However, the precise route by which BAX and BAK transform from monomers to oligomers on the mitochondrial membrane remains an open question. Furthermore, a number of hypotheses (backed by atomic force microscopy, electron tomography and superresolution microscopy) have been provided to explain the mechanism of pore formation by these oligomers, and the nature of the pore itself. In summary, it was shown that BAX and BAK assemble in different shapes (rings, arcs, lines and clusters) with variable sizes (Salvador-Gallego et al. 2016; Ader et al. 2019). It was further discovered that BAK oligomerizes faster than BAX into smaller structures, and can recruit BAX leading to co-assembly (Cosentino et al. 2022). Interestingly, pores formed by either BAK or BAX were able to release mitochondrial DNA, with BAK having faster dynamics.

Is BOK a true BCL-2 effector?

On the amino acid sequence level, BOK is the closest BCL-2 family member to BAX and BAK but its exact role in apoptosis remained unclear in contrast to the canonical effectors (Naim and Kaufmann 2020). In addition, it is predominantly localized to the

membranes of the ER (in complex with IP3 receptors) and Golgi rather than the mitochondria. BOK has been widely considered to be a pro-apoptotic protein, but its ability to work as an effector independent of BAX and BAK remained controversial. Over the years, evidence has been accumulating to support the MOMP effector role of BOK. In summary, it was found that mitochondrial apoptosis defects are more exacerbated in $BAX^{-/-}BAK^{-/-}BOK^{-/-}$ mice than in $BAX^{-/-}BAK^{-/-}$ mice (Ke et al. 2018). In addition, it was shown that BOK can be upregulated through proteasome inhibition, using ER stress drugs, which led to protein stabilization and apoptosis execution (Llambi et al. 2016). Structurally, BOK was shown to be susceptible to spontaneous conformational changes, which can explain its constitutive activity without the need for direct activation (Zheng et al. 2018). Furthermore, in-vitro studies have shown that BOK (like BAX and BAK) can form toroidal pores in liposomes which are large enough to pass cytochrome c (Fernández-Marrero et al. 2017).

How BOK thermostability is linked to pore formation?

Here, we have studied the molecular mechanism and regulation of BOK pore forming activity both in vitro and in cells and performed direct visualization of BOK pores in liposomes. We have employed a protocol for the expression and purification of recombinant BOK that ensured the purity and homogeneity of the produced protein. In addition, the separation of monomeric and oligomeric species was performed using size-exclusion chromatography. We could produce both Full-length BOK (FL-BOK) and a c-terminally truncated version (BOKΔC). Because FL-bok had a high tendency to aggregate during the purification process, we could not produce it in a reliable and reproducible manner. Accordingly, BOKΔC was used for most of the subsequent experiments and was also used for fluorescent labeling. For this, we have utilized Sortase enzyme to attach an Atto488-tagged peptide to the N-terminus of BOKΔC (Theile et al. 2013). This reaction proved to be efficient and almost complete, and importantly it guaranteed that the protein is tagged with only one dye molecule in its N-terminus. This feature is crucial for the accurate estimation of the stoichiometry of the protein assemblies in the subsequent single-molecule experiments. The C-terminal tail of the BCL-2 proteins is important for protein targeting to different membranes in the cell. This applies also to BOK, as its C-terminal tail was shown to be essential to its characteristic subcellular localization.

However, we found that BOK tail was not essential for the permeabilization activity of the protein in liposomes.

We found that BOK thermostability can be an important factor for explaining the membrane permeabilization activity of BOK. Compared to BAX and BAK, we observed that BOK melting temperature is significantly lower. The melting temperature of BOK is further lowered by deleting the C-terminal tail, which can be explained by the formation of domain-swapped dimers by full length BOK, which could stabilize the globular BCL-2 fold in solution. Such a dimer has been previously reported to be an inhibitory mechanism for BAX (Garner et al. 2016), which could be associated with such stabilization of the inactive conformation. In line with this, we found that BOK activity in liposomes can be promoted with heat which agrees with earlier reports that BAX and BAK can be activated by increasing the temperature (Pagliari et al. 2005). This can increase the probability of partial protein unfolding and exposure of helices involved in interaction with the membrane, typically associated with the activation process. Accordingly, this partial instability of the protein can explain its autoactivity. This hypothesis was supported by a study in which the BOK mutant G35A was more stable than wild type BOK and induced less permeabilization of liposomes (Zheng et al. 2018). We have also observed that this mutant induces apoptosis in HCT cells to a lesser extent than wild type BOK. Accordingly, protein stability of BCL-2 proteins may be the main bottleneck that determines the pore forming activity. In line with this, the anti-apoptotic members were shown to induce pore formation upon proteolysis by caspase-3 (Kirsch et al. 1999; Basañez et al. 2001). We can then attribute the opposing activity of the anti-apoptotic and pro-apoptotic BCL-2 family members, at least partially, to the difference in the protein stability and the susceptibility to conformational changes upon binding to BH3-only proteins. In addition, we have found that liposome permeabilization of BOK is dependent on membrane composition, with increasing the ratio of the negatively-charged cardiolipin resulting in more permeabilization, in agreement to previous reports.

The interaction between BOK and cBID

It has been shown in cells and in-vitro experiments that cBID can activate both BAX and BAK (Ren et al. 2010). On the other hand, the ability of cBID to activate BOK

remained elusive for a long time. Fernández-Marrero et al. have reported that BOK-induced pore formation in liposomes was enhanced by the presence of cBID, but BOK failed to induce permeabilization of isolated mitochondria from $BAX^{-/-}BAK^{-/-}$ cells, even in the presence of cBID (Fernández-Marrero et al. 2017). In contrast to this, Llambi et. al have shown that cBID has no effect on liposome permeabilization by BOK (Llambi et al. 2016). In the latter study, BH3 peptides from six BH3-only proteins failed to activate BOK for membrane permeabilization. However, it was reported that BID binds to the hydrophobic groove of BOK with a very low affinity (Kd~2.6 mM) compared to BAX and BAK (Zheng et al. 2018). This low affinity was explained by structural features of the hydrophobic groove of BOK resolved by NMR. We have observed here that cBID does not enhance the permeabilization activity of BOK in liposomes. The low affinity between cBID and BOK can partially explain the discrepancy of results reported before, as the interaction between the two proteins might be only captured using certain concentration ratios and is sensitive to variability of recombinant protein production conditions. However, this would raise the question of how BOK can oligomerize to form pores, if its hydrophobic groove can not accommodate BH3 peptides. It is well established that BH3 helix-into-groove interaction is the main mechanism for the homo-oligomerization and subsequent pore formation by BAX and BAK (Dewson et al. 2012; Jeng et al. 2018). It is then worth investigating whether this is also the case for BOK, or whether there is an alternative mechanism that enables BOK oligomerization.

The topology of BOK-induced pores

We have directly visualized BOK-induced pores in liposomes using negative-stain EM. Electron microscopy allows the resolving of structural details in a very high resolution and has been previously employed for studying pore forming proteins including BAX (Gillies et al. 2015). Here, we have used negative staining to enhance the contrast of the acquired images of pores directly induced in liposomes. This overcomes the need to use nanogold labeling. We have observed that BOK forms pores in the membrane which are similar to those induced by BAX. These results go in line with earlier observations that BOK forms large and stable toroidal pores in liposomes (Fernández-Marrero et al. 2017). In addition, the pores exhibited the same diameter flexibility like BAX and BAK, and no protein density was detected on the pore rims. It is worth mentioning that the pores induced by BAX and BAK have a

heterogenous proteolipidic nature (the lumen is lined by both protein and lipid headgroups), and is resistant to being isolated and thoroughly studied (Flores-Romero et al. 2020; Moldoveanu 2023). This for example was not observed in gasdermin-induced pores, which had a much narrower diameter distribution with defined protein density around the pores. This characteristic feature of gasdermin pore allowed the resolving of the whole pore to a resolution of 4.2 Å using Cryo-EM (Ruan et al. 2018). We also observed that pores induced by BOK or BAX increased in size upon increasing the protein concentration. We also found that both FL-BOK and BOKΔC induced the formation of similar pores, which may indicate that both versions of the protein act similarly even if they have different levels of activity. In summary, these results provide direct evidence of BOK pore formation in liposomes, similar to BAX and BAK, which adds additional evidence for the MOMP effector activity of BOK.

The mechanism of BOK oligomerization

We have employed single-molecule stoichiometry analysis to study the assembly of BOK oligomers in supported lipid bilayers composed of phosphatidylcholine:cardiolipin. We could detect the formation of a mixture of oligomeric species similar to what has been reported for BAX (Subburaj et al. 2015). In addition, the extent of BOK oligomerization increased with increasing the protein concentration. We can conclude that this oligomerization is specific because it was not detected when BOK was imaged on glass or when it was incubated with membranes formed from only phosphatidylcholine. This indicates that BOK oligomerization is related to its permeabilizing activity, where both are sensitive to the membrane composition. In contrast to BAX that has been shown to oligomerize based on dimer units, we could not confirm the same mechanism in the case of BOK despite detecting some enrichment of oligomeric species that are multiples of dimers.

Pro-apoptotic activity of BOK

In cells, we found that BOK can induce MOMP and apoptosis in the absence of BAX and BAK. The magnitude of apoptotic cell death was the same in WT HCT cells, HCT $BAX^{-/-}BAK^{-/-}$ cells and HCT AKO cells. This indicates that BOK doesn't act upstream of the classical effectors (BAX and BAK) and its pro-apoptotic activity is

not affected by the other BCL-2 proteins. Importantly, BOK induced-cell death is diminished in HCT casp9$^{-/-}$, implying that the protein kills cells through the mitochondrial pathway of apoptosis. It has been widely reported that most apoptotic stimuli cannot induce apoptosis in cells missing both BAX and BAK. This observation led to the identification of both proteins as the indispensable apoptotic effectors for a long time (Moldoveanu and Czabotar 2020). Still, it was reported that proteasome inhibitors can induce apoptosis in these cell lines. Additional evidence that supports the effector function of BOK emerged from a recent study that linked SARS-CoV-2 infection to mitochondrial apoptosis. In that study, BOK was shown to be upregulated by the SARS-CoV-2 membrane protein M, resulting in apoptosis that led to lung edema in mice (Yang et al. 2022). It was shown that SARS-CoV-2 M protein stabilizes BOK through inhibiting its ubiquitination which results in its translocation to the mitochondria. The interaction involved the endodomain of M protein and BH2 domain of BOK. Interestingly, M protein was able to trigger BOK-dependent apoptotic pathways in the absence of BAX and BAK. In contrast to this, it has been shown in a recent paper that endogenous BOK is not constitutively degraded by the proteasome, and proteasome inhibitor-induced apoptosis is not mediated by BOK (Bonzerato et al. 2022). These controversial findings indicate that the regulation of BOK activity is still a key open question. Furthermore, It was also shown that the TMDs of BOTH BOK and MCL-1 oligomerize at the mitochondrial membrane (Lucendo et al. 2020). The co-expression of Mcl-1 and BOK TMDs enhanced the formation of ER mitochondrial-associated membranes, which means that MCL-1 induced the mitochondrial targeting of BOK.

BOK limited mitochondrial localization and its activity regulation

We found that, in cells, BOK localizes to the mitochondria, ER and probably other cellular membranes, in agreement with previous reports (Echeverry et al. 2013). From here, we proposed that BOK activity is controlled through limiting its mitochondrial localization and subsequent MOMP. We then generated a BOK chimera where the C-terminal tail is replaced with the one from BCL-xL. As expected, the mutant was almost completely localized to the mitochondria in agreement with the typical localization of BCL-xL. Interestingly, this mutant induced apoptotic cell death with a potency similar to BAX. This indicates that BOK is a potent MOMP effector, and its activity is inhibited by the lack of mitochondrial

accumulation. However, once there, it has the capacity to induce MOMP and apoptosis like BAX. This model partially overlaps with the hypothesis of proteasomal degradation of BOK reported by (Llambi et al. 2016). Importantly, we decided to graft the tail from an antiapoptotic protein (BCL-xL) but not from BAK (which is also typically localized to the mitochondria) to exclude the probability that the tail contributes to the permeabilization activity of the protein. Our data suggest that the regulation of BOK activity is executed through mechanisms that affect its intracellular localization, which are yet to be discovered. This chimeric protein can be used to further study the role of BOK in mitochondrial apoptosis because it localizes to the mitochondria and it is constitutively active.

BOK assemblies revealed by super-resolution microscopy

STED is a super-resolution microscopy technique that allows for the imaging of structures at resolutions beyond the diffraction limit of light, which is around 200-300 nm. The technique has been employed before to study the localization and interactions of BCL-2 proteins within cells. Using STED microscopy, we could detect ring-shaped structures formed by BOK in the mitochondria of apoptotic cells. Similar structures have been reported before to be formed by BAX and BAK (Cosentino et al. 2022). This may indicate that BOK mediates MOMP through a common molecular mechanism with BAX and BAK. Still, at this point we cannot firmly conclude that the observed structures correspond to pores in the mitochondria. It is also noteworthy that these structures were detected upon transient overexpression of BOK, and confirmation by imaging of endogenous BOK is still needed. This is challenged by the low level of endogenous BOK expression and discrepancy among different cell lines.

5. References

Ader NR, Hoffmann PC, Ganeva I, et al (2019) Molecular and topological reorganizations in mitochondrial architecture interplay during Bax-mediated steps of apoptosis. Elife 8.: https://doi.org/10.7554/eLife.40712

Barclay LA, Wales TE, Garner TP, et al (2015) Inhibition of Pro-apoptotic BAX by a noncanonical interaction mechanism. Mol Cell 57:873–886

Basañez G, Zhang J, Chau BN, et al (2001) Pro-apoptotic cleavage products of Bcl-xL form cytochrome c-conducting pores in pure lipid membranes. J Biol Chem 276:31083–31091

Beroukhim R, Mermel CH, Porter D, et al (2010a) The landscape of somatic copy-number alteration across human cancers. Nature 463:899–905

Beroukhim R, Meyerson M, Garraway L, Prensner J (2010b) Abstract 5759: The landscape of copy-number changes across multiple human cancer types. Cancer Res 70:5759–5759

Bleicken S, Hantusch A, Das KK, et al (2017) Quantitative interactome of a membrane Bcl-2 network identifies a hierarchy of complexes for apoptosis regulation. Nat Commun 8:73

Bock FJ, Tait SWG (2020) Mitochondria as multifaceted regulators of cell death. Nat Rev Mol Cell Biol 21:85–100

Bonzerato CG, Keller KR, Schulman JJ, et al (2022) Endogenous Bok is stable at the endoplasmic reticulum membrane and does not mediate proteasome inhibitor-induced apoptosis. Frontiers in Cell and Developmental Biology 10

Campbell KJ, Tait SWG (2018) Targeting BCL-2 regulated apoptosis in cancer. Open Biology 8:180002

Carberry S, D'Orsi B, Monsefi N, et al (2018) The BAX/BAK-like protein BOK is a prognostic marker in colorectal cancer. Cell Death Dis 9:125

Carpio MA, Means RE, Brill AL, et al (2021) BOK controls apoptosis by Ca transfer through ER-mitochondrial contact sites. Cell Rep 34:108827

Carpio MA, Michaud M, Zhou W, et al (2015) BCL-2 family member BOK promotes apoptosis in response to endoplasmic reticulum stress. Proc Natl Acad Sci U S A 112:7201–7206

Chipuk JE, Luna-Vargas MP (2016) Cell Biology: ERADicating Survival with BOK. Curr. Biol. 26:R473–6

Chou JJ, Li H, Salvesen GS, et al (1999) Solution structure of BID, an intracellular amplifier of apoptotic signaling. Cell 96:615–624

Cosentino K, García-Sáez AJ (2017) Bax and Bak Pores: Are We Closing the Circle? Trends Cell Biol 27:266–275

Cosentino K, Hertlein V, Jenner A, et al (2022) The interplay between BAX and BAK tunes apoptotic pore growth to control mitochondrial-DNA-mediated inflammation. Mol Cell 82:933–949.e9

Cournia Z, Allen TW, Andricioaei I, et al (2015) Membrane Protein Structure, Function, and Dynamics: a Perspective from Experiments and Theory. The Journal of Membrane Biology 248:611–640

Cui J, Zhao S, Li Y, et al (2021) Regulated cell death: discovery, features and implications for neurodegenerative diseases. Cell Commun Signal 19:120

Czabotar PE, Lessene G, Strasser A, Adams JM (2014) Control of apoptosis by the BCL-2 protein family: implications for physiology and therapy. Nat Rev Mol Cell Biol 15:49–63

Czabotar PE, Westphal D, Dewson G, et al (2013) Bax crystal structures reveal how BH3 domains activate Bax and nucleate its oligomerization to induce apoptosis. Cell 152:519–531

Dewson G, Ma S, Frederick P, et al (2012) Bax dimerizes via a symmetric BH3:groove interface during apoptosis. Cell Death & Differentiation 19:661–670

Echeverry N, Bachmann D, Ke F, et al (2013) Intracellular localization of the BCL-2 family member BOK and functional implications. Cell Death Differ 20:785–799

Edlich F, Banerjee S, Suzuki M, et al (2011) Bcl-x(L) retrotranslocates Bax from the mitochondria into the cytosol. Cell 145:104–116

Einsele-Scholz S, Malmsheimer S, Bertram K, et al (2016) Bok is a genuine multi-BH-domain protein that triggers apoptosis in the absence of Bax and Bak. J Cell Sci 129:3054

Fernandez-Marrero Y, Bachmann D, Lauber E, Kaufmann T (2018) Negative Regulation of BOK Expression by Recruitment of TRIM28 to Regulatory Elements in Its 3′ Untranslated Region. iScience 9:461–474

Fernández-Marrero Y, Bleicken S, Das KK, et al (2017) The membrane activity of BOK involves formation of large, stable toroidal pores and is promoted by cBID. The FEBS Journal 284:711–724

Flores-Romero H, García-Sáez AJ (2019) The Incomplete Puzzle of the BCL2 Proteins. Cells 8.: https://doi.org/10.3390/cells8101176

Flores-Romero H, Ros U, Garcia-Saez AJ (2020) Pore formation in regulated cell death. The EMBO Journal 39

Fuchs Y, Steller H (2011) Programmed Cell Death in Animal Development and Disease. Cell 147:1640

Galluzzi L, Pedro JMB-S, Kepp O, Kroemer G (2016) Regulated cell death and adaptive stress responses. Cellular and Molecular Life Sciences 73:2405–2410

Galluzzi L, Vitale I, Aaronson SA, et al (2018) Molecular mechanisms of cell death: recommendations of the Nomenclature Committee on Cell Death 2018. Cell Death Differ 25:486–541

Gao S, Fu W, Dürrenberger M, et al (2005) Membrane translocation and oligomerization of hBok are triggered in response to apoptotic stimuli and Bnip3. Cell Mol Life Sci 62:1015–1024

Gavathiotis E, Suzuki M, Davis ML, et al (2008) BAX Activation is Initiated at a Novel Interaction Site

Ghavami S, Shojaei S, Yeganeh B, et al (2014) Autophagy and apoptosis dysfunction in neurodegenerative disorders. Progress in Neurobiology 112:24–49

Gillies LA, Du H, Peters B, et al (2015) Visual and functional demonstration of growing Bax-induced pores in mitochondrial outer membranes. Mol Biol Cell 26:339–349

Happo L, Strasser A, Cory S (2012) BH3-only proteins in apoptosis at a glance. Journal of Cell Science 125:1081–1087

Hardwick JM, Soane L (2013) Multiple Functions of BCL-2 Family Proteins. Cold Spring Harbor Perspectives in Biology 5:a008722–a008722

Hinds MG, Smits C, Fredericks-Short R, et al (2007) Bim, Bad and Bmf: intrinsically unstructured BH3-only proteins that undergo a localized conformational change upon binding to prosurvival Bcl-2 targets. Cell Death Differ 14:128–136

Hsu SY, Kaipia A, McGee E, et al (1997) Bok is a pro-apoptotic Bcl-2 protein with restricted expression in reproductive tissues and heterodimerizes with selective anti-apoptotic Bcl-2 family members. Proc Natl Acad Sci U S A 94:12401–12406

Huang K, Zhang J, O'Neill KL, et al (2016) Cleavage by Caspase 8 and Mitochondrial Membrane Association Activate the BH3-only Protein Bid during TRAIL-induced Apoptosis. J Biol Chem 291:11843–11851

Inohara N, Ekhterae D, Garcia I, et al (1998) Mtd, a novel Bcl-2 family member activates apoptosis in the absence of heterodimerization with Bcl-2 and Bcl-XL. J Biol Chem 273:8705–8710

Ivanova H, Vervliet T, Missiaen L, et al (2014) Inositol 1,4,5-trisphosphate receptor-isoform diversity in cell death and survival. Biochim Biophys Acta 1843:2164–2183

Jeng PS, Inoue-Yamauchi A, Hsieh JJ, Cheng EH (2018) BH3-dependent and independent activation of BAX and BAK in mitochondrial apoptosis. Current Opinion in Physiology 3:71–81

Julien O, Wells JA (2017) Caspases and their substrates. Cell Death Differ 24:1380–1389

Kale J, Osterlund EJ, Andrews DW (2018) BCL-2 family proteins: changing partners in the dance towards death. Cell Death Differ 25:65–80

Kalkavan H, Green DR (2018) MOMP, cell suicide as a BCL-2 family business. Cell Death Differ 25:46–55

Ke FFS, Vanyai HK, Cowan AD, et al (2018) Embryogenesis and Adult Life in the Absence of Intrinsic Apoptosis Effectors BAX, BAK, and BOK. Cell 173:1217–1230.e17

Ke F, Voss A, Kerr JB, et al (2012) BCL-2 family member BOK is widely expressed but its loss has only minimal impact in mice. Cell Death Differ 19:915–925

Kirsch DG, Doseff A, Chau BN, et al (1999) Caspase-3-dependent cleavage of Bcl-2 promotes release of cytochrome c. J Biol Chem 274:21155–21161

Kroemer G, Galluzzi L, Vandenabeele P, et al (2009) Classification of cell death: recommendations of the Nomenclature Committee on Cell Death 2009. Cell Death Differ 16:3–11

Lindsten T, Ross AJ, King A, et al (2000) The combined functions of proapoptotic Bcl-2 family members bak and bax are essential for normal development of multiple tissues. Mol Cell 6:1389–1399

Llambi F, Moldoveanu T, Tait SWG, et al (2011) A unified model of mammalian BCL-2 protein family interactions at the mitochondria. Mol Cell 44:517–531

Llambi F, Wang Y-M, Victor B, et al (2016) BOK Is a Non-canonical BCL-2 Family Effector of Apoptosis Regulated by ER-Associated Degradation. Cell 165:421–433

Lucendo E, Sancho M, Lolicato F, et al (2020) Mcl-1 and Bok transmembrane domains: Unexpected players in the modulation of apoptosis. Proc Natl Acad Sci U S A 117:27980–27988

McArthur K, Whitehead LW, Heddleston JM, et al (2018) BAK/BAX macropores facilitate mitochondrial herniation and mtDNA efflux during apoptosis. Science 359.: https://doi.org/10.1126/science.aao6047

McDonnell JM, Fushman D, Milliman CL, et al (1999) Solution structure of the proapoptotic molecule BID: a structural basis for apoptotic agonists and antagonists. Cell 96:625–634

Miles MA, Hawkins CJ (2017) Executioner caspases and CAD are essential for mutagenesis induced by TRAIL or vincristine. Cell Death & Disease 8:e3062–e3062

Moldoveanu T (2023) Apoptotic mitochondrial poration by a growing list of pore-forming BCL-2 family proteins. Bioessays e2200221

Moldoveanu T, Czabotar PE (2020) BAX, BAK, and BOK: A Coming of Age for the BCL-2 Family Effector Proteins. Cold Spring Harbor Perspectives in Biology 12:a036319

Montero J, Letai A (2018) Why do BCL-2 inhibitors work and where should we use them in the clinic? Cell Death Differ 25:56–64

Moravcikova E, Krepela E, Donnenberg VS, et al (2017) BOK displays cell death-independent tumor suppressor activity in non-small-cell lung carcinoma. Int J Cancer 141:2050–2061

Naim S, Kaufmann T (2020) The Multifaceted Roles of the BCL-2 Family Member BOK. Front Cell Dev Biol 8:574338

Pagliari LJ, Kuwana T, Bonzon C, et al (2005) The multidomain proapoptotic molecules Bax and Bak are directly activated by heat. Proc Natl Acad Sci U S A 102:17975–17980

Ren D, Tu H-C, Kim H, et al (2010) BID, BIM, and PUMA are essential for activation of the BAX- and BAK-dependent cell death program. Science 330:1390–1393

Riley JS, Quarato G, Cloix C, et al (2018) Mitochondrial inner membrane permeabilisation enables mtDNA release during apoptosis. EMBO J 37.: https://doi.org/10.15252/embj.201899238

Rodriguez JM, Glozak MA, Ma Y, Cress WD (2006) Bok, Bcl-2-related Ovarian Killer, Is Cell Cycle-regulated and Sensitizes to Stress-induced Apoptosis. J Biol Chem 281:22729–22735

Ruan J, Xia S, Liu X, et al (2018) Cryo-EM structure of the gasdermin A3 membrane pore. Nature 557:62–67

Salvador-Gallego R, Mund M, Cosentino K, et al (2016) Bax assembly into rings and arcs in apoptotic mitochondria is linked to membrane pores. EMBO J 35:389–401

Schulman JJ, Szczesniak LM, Bunker EN, et al (2019) Bok regulates mitochondrial fusion and morphology. Cell Death Differ 26:2682–2694

Schulman JJ, Wright FA, Han X, et al (2016) The Stability and Expression Level of Bok Are Governed by Binding to Inositol 1,4,5-Trisphosphate Receptors. J Biol Chem 291:11820–11828

Sender R, Milo R (2021) The distribution of cellular turnover in the human body. Nat Med 27:45–48

Shalaby R, Flores-Romero H, García-Sáez AJ (2020) The Mysteries around the BCL-2 Family Member BOK. Biomolecules 10.: https://doi.org/10.3390/biom10121638

Shamas-Din A, Kale J, Leber B, Andrews DW (2013) Mechanisms of action of Bcl-2 family proteins. Cold Spring Harb Perspect Biol 5:a008714

Srivastava R, Cao Z, Nedeva C, et al (2019) BCL-2 family protein BOK is a positive regulator of uridine metabolism in mammals. Proc Natl Acad Sci U S A 116:15469–15474

Stehle D, Grimm M, Einsele-Scholz S, et al (2018) Contribution of BH3-domain and Transmembrane-domain to the Activity and Interaction of the Pore-forming Bcl-2 Proteins Bok, Bak, and Bax. Sci Rep 8:12434

Strasser A, Jost PJ, Nagata S (2009) The many roles of FAS receptor signaling in the immune system. Immunity 30:180–192

Subburaj Y, Cosentino K, Axmann M, et al (2015) Bax monomers form dimer units in the membrane that further self-assemble into multiple oligomeric species. Nat Commun 6:8042

Sun Z, Liu Q, Qu G, et al (2019) Utility of B-Factors in Protein Science: Interpreting Rigidity, Flexibility, and Internal Motion and Engineering Thermostability. Chem Rev 119:1626–1665

Szondy Z, Sarang Z, Kiss B, et al (2017) Anti-inflammatory Mechanisms Triggered by Apoptotic Cells during Their Clearance. Frontiers in Immunology 8

Taylor RC, Cullen SP, Martin SJ (2008) Apoptosis: controlled demolition at the cellular level. Nat Rev Mol Cell Biol 9:231–241

Theile CS, Witte MD, Blom AEM, et al (2013) Site-specific N-terminal labeling of proteins using sortase-mediated reactions. Nat Protoc 8:1800–1807

Townsend PA, Kozhevnikova MV, Cexus ONF, et al (2021) BH3-mimetics: recent developments in cancer therapy. J Exp Clin Cancer Res 40:355

Urra H, Dufey E, Lisbona F, et al (2013) When ER stress reaches a dead end. Biochimica et Biophysica Acta (BBA) - Molecular Cell Research 1833:3507–3517

Wang C, Youle RJ (2012) Predominant requirement of Bax for apoptosis in HCT116 cells is determined by Mcl-1's inhibitory effect on Bak. Oncogene 31:3177–3189

Wilfling F, Weber A, Potthoff S, et al (2012) BH3-only proteins are tail-anchored in the outer mitochondrial membrane and can initiate the activation of Bax. Cell Death Differ 19:1328–1336

Williams A, Hayashi T, Wolozny D, et al (2016) The non-apoptotic action of Bcl-xL: regulating Ca(2+) signaling and bioenergetics at the ER-mitochondrion interface. J Bioenerg Biomembr 48:211–225

Wong RSY (2011) Apoptosis in cancer: from pathogenesis to treatment. Journal of Experimental & Clinical Cancer Research 30

Yakovlev AG, Di Giovanni S, Wang G, et al (2004) BOK and NOXA are essential mediators of p53-dependent apoptosis. J Biol Chem 279:28367–28374

Yang Y, Wu Y, Meng X, et al (2022) SARS-CoV-2 membrane protein causes the mitochondrial apoptosis and pulmonary edema via targeting BOK. Cell Death Differ 29:1395–1408

Zheng JH, Grace CR, Guibao CD, et al (2018) Intrinsic Instability of BOK Enables Membrane Permeabilization in Apoptosis. Cell Rep 23:2083–2094.e6

6. Appendix

Accepted publications

CDDpress

www.nature.com/cdd

ARTICLE OPEN

Check for updates

Visualization of BOK pores independent of BAX and BAK reveals a similar mechanism with differing regulation

Raed Shalaby[1], Arzoo Diwan[1], Hector Flores-Romero[1], Vanessa Hertlein[2] and Ana J. Garcia-Saez[1]✉

BOK is a poorly understood member of the BCL-2 family of proteins that has been proposed to function as a pro-apoptotic, BAX-like effector. However, the molecular mechanism and structural properties of BOK pores remain enigmatic. Here, we show that the thermal stability and pore activity of BOK depends on the presence of its C-terminus as well as on the mitochondrial lipid cardiolipin. We directly visualized BOK pores in liposomes by electron microscopy, which appeared similar to those induced by BAX, in line with comparable oligomerization properties quantified by single molecule imaging. In addition, super-resolution STED imaging revealed that BOK organized into dots and ring-shaped assemblies in apoptotic mitochondria, also reminiscent of those found for BAX and BAK. Yet, unlike BAX and BAK, the apoptotic activity of BOK was limited by partial mitochondrial localization and was independent of and unaffected by other BCL-2 proteins. These results suggest that, while BOK activity is kept in check by subcellular localization instead of interaction with BCL-2 family members, the resulting pores are structurally similar to those of BAX and BAK.

- BOK-induced pores were directly visualized in liposomes using negative staining EM.
- BOK apoptotic activity is comparable to and independent of BAX and BAK, including formation of rings in apoptotic mitochondria.
- Apoptosis induction by BOK is limited by partial mitochondrial localization.

Cell Death & Differentiation; https://doi.org/10.1038/s41418-022-01078-w

INTRODUCTION

The mitochondrial pathway of apoptosis is controlled by the proteins of the BCL-2 family [1]. The effector proteins BAX and BAK directly mediate the key step of permeabilization of the mitochondrial outer membrane (MOM), which releases cytochrome c and Smac into the cytosol to induce the caspases activation leading to cell death [2–4]. The activity of BAX and BAK is counteracted by the prosurvival BCL-2 proteins, like BCL-2, BCL-xL and MCL-1 [5, 6]. The pro-apoptotic BH3-only proteins including tBID, BIM or PUMA, promote cell death by activating the effectors and/or blocking the anti-apoptotic family members [3].

BCL-2 related ovarian killer (BOK) is BCL-2 family member was initially categorized as a pro-apoptotic BCL-2 family member based on sequence similarity with BAX and BAK and on transient overexpression experiments [7]. This view was supported by studies reporting that overexpression of BOK can induce membrane permeabilization and mitochondrial apoptosis, independent of BAX and BAK [8]. The increased severity of the phenotype of $BAX^{-/-}$ $BAK^{-/-}$ $BOK^{-/-}$ mice compared to $BAX^{-/-}$ $BAK^{-/-}$ animals provided additional support for this model [9].

The structure of inactive, monomeric BOK in soluble form presents the typical BCL-2 fold [9, 10], with two central hydrophobic helices surrounded by amphipathic α-helices [11]. The two central helices of BCL-2 effector proteins become embedded in the membrane when the protein is activated, leading to permeabilization [12–14]. The structure of BOK additionally contained an occluded hydrophobic groove that could underlie the inability to interact with the BH3 domain of BH3-only proteins. It has been proposed that BOK can interact with MCL-1 and BFL-1 via its BH3-domain, but not with other antiapoptotic proteins [7, 15]. This is a distinct feature of BOK and suggests alternative regulatory mechanisms. Accordingly, BOK is maintained at low levels by proteasomal degradation, which upon ER stress lead to BOK accumulation and cell death induction [8].

Despite these recent advances, BOK remains an enigmatic protein far less understood than most BCL-2 family members. One key aspect is whether BOK is able to mediate mitochondrial permeabilization directly via the opening of membrane pores. Related to this, little is known about the molecular mechanism underlying the pore activity of BOK and how it compares to that of

[1]Institute for Genetics and Cologne Excellence Cluster on Cellular Stress Responses in Aging-Associated Diseases (CECAD), University of Cologne, Joseph-Stelzmann-Straße 26, 50931 Cologne, Germany. [2]Interfaculty Institute of Biochemistry, Eberhard-Karls-Universität Tübingen, Tübingen, Germany. ✉email: ana.garcia@uni-koeln.de

Edited by G Melino

Received: 24 April 2022 Revised: 5 October 2022 Accepted: 6 October 2022
Published online: 26 October 2022

Official journal of CDDpress

SPRINGER NATURE
CDDpress

BAX and BAK, especially regarding the role of protein oligomerization, as well as regulation of the pore activity.

Here, we studied the properties of BOK pores independent of BAX and BAK by combining experiments in chemically controlled systems with model membranes and in cells. We directly visualize BOK nanoscale assemblies and membrane pores, which presented similar properties to those of BAX and BAK, in line with comparable oligomerization properties. However, in contrast to BAX and BAK, the apoptotic activity of BOK was lower compared to them and was not affected by other pro- and anti-apoptotic BCL-2 proteins. Our data indicate that BOK can directly act as a BCL-2 effector independently of BAX and BAK, albeit with reduced efficiency due to limited mitochondrial localization.

RESULTS

The C-terminus of BOK determines thermostability and pore forming activity

To investigate the interaction of BOK with membranes, we produced recombinant, monomeric, human BOK lacking the last 24 amino acids corresponding to the C-terminal membrane anchor (hereafter BOKΔC) (Fig. 1A and S1), similar to [10, 16]. We also generated full length BOK (FL-BOK) using a similar strategy to BAX and BCL-xL [17, 18]. We obtained a much lower yield, with FL-BOK eluting as a mixture monomers and dimers (Fig. S1). BOKΔC was then fluorescently tagged using sortase A enzyme with 95% efficiency and 1:1 stoichiometry (Fig. S2 and Materials and methods).

We used liposome permeabilization assays to compare the pore forming activity of FL-BOK and BOKΔC in vitro. By monitoring calcein release from large unilamellar vesicles (LUVs), we found that BOKΔC could efficiently permeabilize liposomes, with a composition containing cardiolipin as a simplistic model of the MOM, in a concentration-dependent manner (Fig. 1B), in agreement with previous work [10, 16]. This indicates that the membrane permeabilizing activity of BOK does not require the transmembrane C-terminal region, even if it plays a role in membrane targeting in cells [19]. The extent of permeabilization correlated with the amount of the negatively charged lipid cardiolipin in the liposomes (Fig. 1C). Cardiolipin is a mitochondria-specific phospholipid containing four acyl chains that induces negative membrane curvature, which may also contribute to pore activity. It has been reported to be a key lipid in pore formation by BCL-2 proteins [16, 20–23], although other negatively charged lipids like phosphatidylglycerol can promote comparable pore activity in vitro [16].

BOKΔC was able to spontaneously relocate to liposomes and to induce their permeabilization at room temperature (Fig. 1B–D), unlike BAX (in full-length form), which required co-incubation with cBID for its activation. Neither for BAKΔC, as previous reports required the use of a histidine tag to drive its association with liposomes doped with nickel [24–26]. These results, together with the low effect of cBID on BOKΔC activation, suggested that recombinant BOKΔC was auto-active under our experimental conditions. However, the membrane permeabilizing activity of FL-BOK (dimer fraction) in vitro was similar to that of BAX alone and significantly lower than that of BOKΔC at room temperature (Fig. 1D). Still, cBID did not have a significant effect on FL-BOK activity, suggesting that it is not as efficient as direct activator as in the case of BAX.

Previous studies have proposed that these differences between BOKΔC and BAX (and BAK) could be attributed to the difference in their thermal stability [10]. To check whether the differences in the pore activity of FL-BOK and BOKΔC could be related to this, we determined the melting temperature of FL-BOK, which to our surprise, was higher than that of BOKΔC and close to that of BAX (Fig. 1E). We then compared the energetic threshold for BOKΔC, FL-BOK and BAX pore activity by quantifying the extent of LUV permeabilization at different temperatures. As shown in (Fig. 1F–H), both BAX and FL-BOK could be activated by increasing the temperature, as previously reported for BAX [27–29]. However, increasing temperature had no effect on BOKΔC.

Direct visualization of BOK pores in liposomes by electron microscopy

We then aimed at direct imaging of BOK pore formation in liposomes using negative staining electron microscopy (EM). We incubated BOKΔC, FL-BOK, FL-BAX (activated by cBID) and GSDMD (activated by Caspase11) with LUVs for 1 h using 1:100 and of 1:10000 protein:lipid molar ratios. As shown in (Fig. 2A, B), BOKΔC induced liposome alterations depending on protein concentration. Interestingly, almost all permeabilized liposomes had only one pore. At low protein amounts BOKΔC formed relatively well-defined pores with a ring shape, which became more irregular and seemingly associated with membrane invaginations at higher protein:lipid ratio. At lower concentration they adopted a broad distribution of diameters ranging between 20 and 50 nm, with the average around 35 nm (Fig. 2C). With increasing concentration of BOKΔC, the pore diameter increased and often led to complete rupture of the liposomes.

We could also efficiently detect FL-BOK pores in liposomes, which presented a similar shape to those of BOKΔC, although they also seemed to induce membrane invaginations at lower protein:lipid ratio (Fig. 2B). We did not observe a significant difference in the size of pores formed by BOKΔC and FL-BOK, although the distribution of diameters slightly increased for the full-length protein (Fig. 2C).

When compared to other pore forming proteins involved in cell death (Fig. 2B, C), similar results in terms of pore size and shape were obtained for BOK and BAX pores, suggesting that both proteins follow the same mechanisms of membrane permeabilization. Remarkably, the pores formed by GSDM-D were smaller and their size distribution was narrower. In addition, protein density at the pore edge was consistently seen only in the case of GSDM-D. Instead, in the case of BOK and BAX, no protein density could be observed around the pore rims, also in line with previous analysis of BAX pores by EM [13, 30].

BOK exists as a mixture of oligomeric species in the membrane

These results suggested that BOK follows a similar mechanism of membrane permeabilization to that of BAX and BAK, for which the formation of lipid/protein pores is accompanied by assembly into multiple oligomeric species [21, 28, 31–33]. To compare the oligomerization properties of BOK in the membrane with those of BAX, we used total internal reflection fluorescence (TIRF) single-molecule imaging as in our previous work [28]. We incubated fluorescently tagged BOKΔC 0.5 nM and 100 nM for 1 h with liposomes, allowing for protein binding and oligomerization [34]. The resulting proteoliposomes were then used to produce supported lipid bilayers (SLBs), which were imaged with TIRF microscopy (Fig. 3A).

The brightness of single BOKΔC-488 particles in the membrane showed a broad distribution typical of multiple, coexisting oligomeric species (Fig. 3B, F). The particle fluorescence intensity distribution for individual BOKΔC-488 particles in SLBs was then fitted to multiple Gaussians to calculate the relative fraction of each species (Fig. 3D, E, G, H). The results obtained showed that, in contrast to BAX and BAK [28, 33, 35], oligomerization took place without activation by BH3-only proteins or heat incubation. The size of the oligomers increased with protein concentration, following a similar trend like BAX but not BAK [35]. While at lower concentrations BOKΔC-488 particles existed as a mixture of mainly monomers and dimers, with increasing protein density in the membrane we detected higher oligomeric forms. Oligomeric species above octamers could not be quantified due to inherent

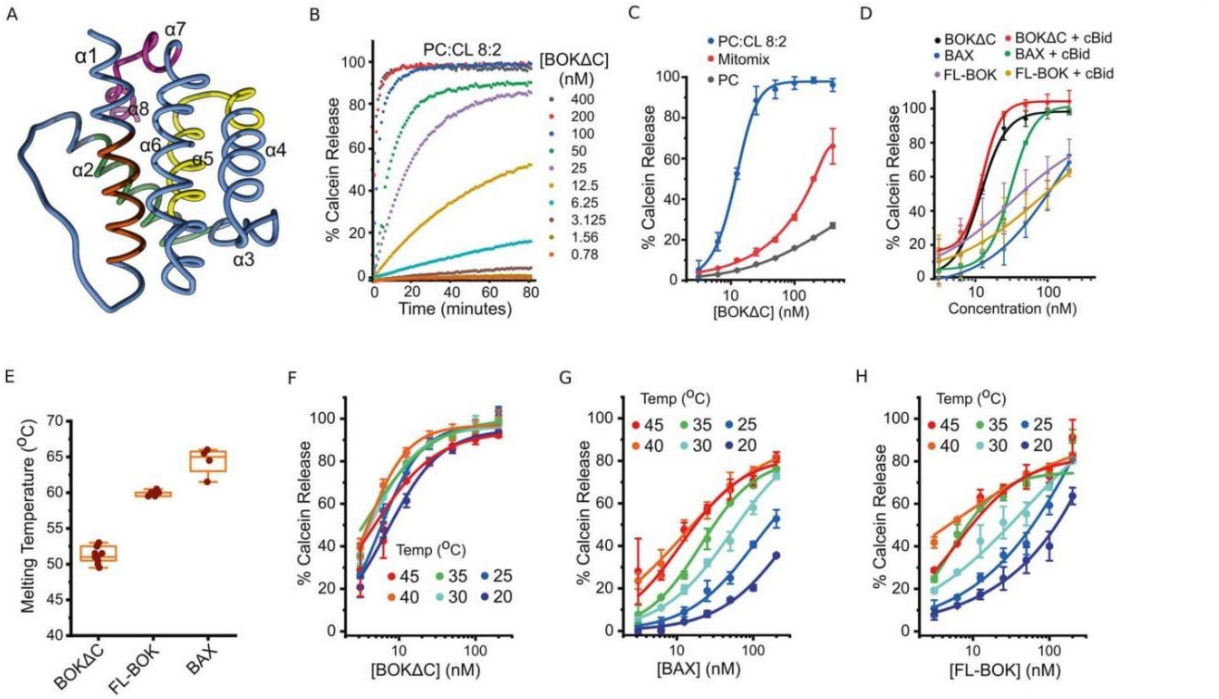

Fig. 1 Permeabilizing activity of recombinant BOK in lipid vesicles depends on the C-terminus and the membrane lipid composition. **A** Structure of human BOKΔC (PDB:6CKV) with the BH domains highlighted in different colors; BH1: orange, BH2: green, BH3: yellow and BH4: purple. BOKΔC structure contains 8 alpha-helices forming a typical BCL-2 fold, each individual helix is numbered. **B** The kinetics of calcein release from LUVs with the composition (PC:CL 8:2) induced by different concentrations of BOKΔC. Calcein release was normalized to the maximum release induced by Triton-X100. **C** Percentage of calcein release from LUVs with the lipid compositions: PC, PC:CL 8:2 and mitochondrial mixture (PC:PE:PI:PS:CL 49:27:10:10:4), induced by different concentration of BOKΔC. Calcein release was normalized to the maximum release induced by Triton-X100. **D** Effect of BAX, BOKΔC and FL-BOK recombinant proteins on LUVs (PC:CL 8:2) membrane permeability in the presence and absence of cBID (40 nM) assessed by calcein release and normalized to the maximum release induced by Triton-X100. **E** Estimated melting temperature of BAX, BOKΔC and FL-BOK derived from thermal shift assay experiments using SYPRO Orange dye. **F**, **G**, **H** Permeabilization activity of BAX, BOKΔC and FL-BOK on LUVs (PC:CL 8:2) at different temperatures, measured and calculated like in **B**. **C**–**H** Values correspond to mean ± SD from at least 3 individual experiments.

limitations of the technique (see Methods). Under these experimental conditions, less than 10% of BOKΔC-488 particles were in monomeric form. Together, these results indicate that BOK has the ability to autoactivate and to recruit additional BOK molecules to the complex, similar to reports for BAK and BAX [28, 35].

As controls, we confirmed that the particle brightness of BOKΔC-488 showed a narrow distribution corresponding to monomers when it was imaged on glass and that membrane binding and oligomerization were not efficient on SLBs made of PC only (Fig. S3). This suggests that cardiolipin, or a negatively charged lipid, is required for BOKΔC-488 binding and oligomerization in the membrane.

Apoptosis induction by BOK is comparable to and independent of BAX and BAK

To study BOK membrane pores in the complex environment of the cell, we analyzed its ability to induce apoptosis in living cells by transiently expressing BOK fused to GFP (GFP-BOK). We used HCT116 lines including wild type (WT HCT116), BAX/BAK double knock out (DKO HCT116), as well as a cell line lacking most BCL-2 proteins in which BOK was additionally knocked out, all BCL-2 knock out (AKO HCT116) [36, 37], which allowed us to evaluate the role of other BCL-2 proteins on the apoptotic activity of BOK. The extent of cell death was assessed by Annexin-V-Alexa647 staining and normalized to transfected (GFP-positive) cells (Fig. 4A).

Remarkably, GFP-BOK efficiently induced apoptotic cell death in AKO HCT116 cells (Fig. 4B), which we also confirmed with overexpression of an untagged version of BOK (Fig. 4C). This clearly demonstrates that BOK can directly mediate mitochondrial permeabilization, thus discarding any requirement for the effectors BAX and BAK, as well as the possibility that BOK killing activity is the result of it inducing a phenotypic switch in the anti-apoptotic BCL-2 members. As reported for BAX and BAK [36], BOK overexpression alone was also sufficient to induce cell death in AKO HCT116 cells, indicating that BH3-only proteins are not necessary for its activation either.

We recently showed that tBID can also mediate mitochondrial permeabilization in absence of BAX and BAK [37]. Indeed, both tBID-GFP and GFP-BOK induced a similar extent of cell death in AKO HCT116 cells. Yet, in contrast to BOK, tBID-induced apoptosis was significantly reduced in DKO HCT116 cells compared to AKO HCT116 cells, as we showed before [37]. This indicates strong inhibition of tBID, but not of BOK, by the anti-apoptotic BCL-2. In agreement with this, the extent of GFP-BOK induced cell death in WT, DKO and AKO HCT116 cell lines was comparable (20-30%). Since both DKO and WT cells harbor anti-apoptotic BCL-2 proteins, these results add to the evidence that the apoptotic activity of BOK is not affected by the antiapoptotic family members (Fig. 4B). Compared to AKO HCT116 cells, overexpression of tBID-GFP led to an increase in cell death in WT HCT116 cells expressing BAX and BAK (Fig. 4D), which underscores the role of tBID as an activator of

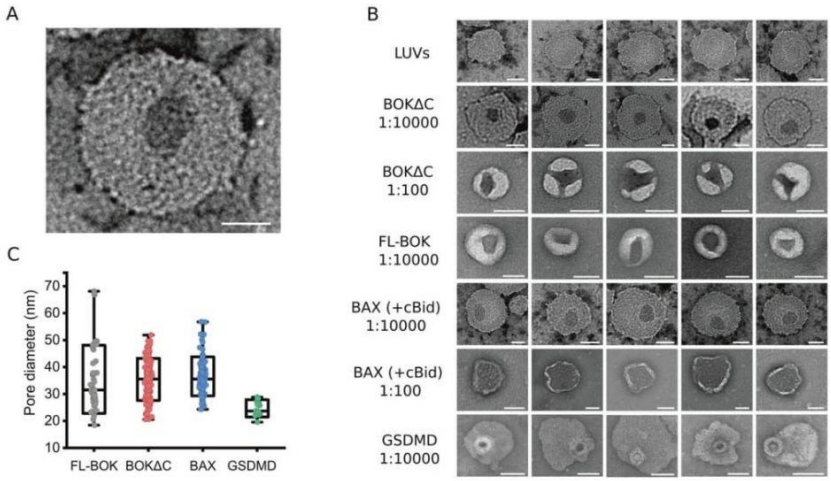

Fig. 2 Visualization of BOK pores in liposomes. A Representative negative staining EM image of a BOK pore in an LUV with the composition PC:CL 8:2. **B** Representative negative staining EM images from incubation of LUVs with different ratios of BAX, BOKΔC, FL-BOK and GSDM-D (activated by Caspase11). Scale bar for all images in **A**–**B**, 50 nm. **C** Quantification of pore size distribution of BAX, BOKΔC, FL-BOK and GSDM-D incubated with LUVs with protein:lipid molar ratio of 1:10000.

BAX and BAK. This effect was not observed for GFP-BOK overexpression, suggesting that BOK cannot act as BAX/BAK activator.

Intrinsic instability leading to auto-activation counteracted by proteasomal degradation has been proposed as an mechanism for regulation of BOK apoptotic activity. In agreement with this, the GFP-BOK G35A mutant, with increased protein stability, showed a slight reduction in apoptosis induction in AKO HCT116 cells (Fig. 4E). In contrast, the significantly impaired cytotoxic activity of GFP-BOKΔC highlights the key role of the C-terminal tail on BOK apoptotic function (Fig. 4E).

Remarkably, only a fraction of GFP-BOK localized to mitochondria, raising the question whether this could a reason for the lower apoptotic activity of BOK in cells (Fig. 4F). To test this hypothesis, we produced a chimeric protein with the C-terminal tail of BOK replaced by that of BCL-xL (GFP-BOK-xL), which almost exclusively localized to mitochondria (Fig. 4F). Importantly, GFP-BOK-xL presented enhanced apoptotic activity comparable to BAX (Fig. 4G). These results directly link the lack of effective mitochondrial localization with the limited BOK activity in cells.

The significant reduction in cell death in HCT caspase-9 knock out cells confirmed that BOK-mediated cell death is of apoptotic nature (Fig. 4B). As additional controls, we confirmed that the cytotoxic activities of BAX and BOK were reduced by the caspase inhibitor zVAD (Fig. 4E). Also, cells transfected with either GFP alone or with the anti-apoptotic GFP-BCL-xL showed minimal or insignificant cell death. We further confirmed loss of mitochondrial membrane potential (TMRE intensity) as a proxy for mitochondrial permeabilization in U2OS $BAX^{-/-}/BAK^{-/-}$ cells transfected with GFP-BOK (Fig. 4H). Finally, we tested the ability of recombinant BOKΔC to permeabilize isolated mitochondria from DKO HCT116 and AKO HCT116 cells. As shown in (Fig. 4I), BOKΔC released cytochrome c in a concentration dependent manner, with an activity comparable to cBID but significantly lower than recombinant FL-BAX. These results indicate that BOK can directly induce mitochondrial permeabilization independently of BAX, BAK and other BCL-2 proteins.

BOK forms ring-like structures in apoptotic mitochondria

Previous studies reported that BOK, in contrast to BAX and BAK, mainly localizes to the ER and Golgi [19] and that it accumulates at the contact sites between the ER and mitochondria, where it plays a role in regulating calcium fluxes between the two organelles [38, 39]. This is in agreement with our data in Fig. 4F. Yet, to mediate mitochondrial permeabilization in absence of other BCL-2 proteins, we reasoned that at least a fraction of BOK localized to mitochondria should assemble there into oligomers responsible for the opening of apoptotic pores.

To address this question in more detail, we explored the subcellular localization BOK in U2OS $BAX^{-/-}/BAK^{-/-}$ cells with respect to mitochondria and/or ER using GFP or Halotag fusion proteins (Fig. 5). In agreement with the lack of apoptotic activity, we found that GFP-BOKΔC presented a diffuse cytosolic distribution, which underscores the key role of the C-terminal anchor for membrane targeting in cells (Fig. 5A). GFP-BOK instead constitutively accumulated in clusters reminiscent of the apoptotic foci formed by BAX and BAK [40, 41] in absence of apoptotic triggers (Fig. 5B). These GFP-BOK clusters presented partial co-localization with mitochondria (dyed with Mitotracker-644) as well as with the ER network (stained with GFP-SEC61), which in some occasions coincided with overlapping points between the two organelles (Fig. 5C–H). 16 h after transfection, only a fraction of the cells expressing BOK had undergone mitochondrial permeabilization measured by Smac release, although the subcellular distribution of BOK was comparable between cells in the population with permeabilized mitochondria or not (Fig. 5I).

We then used super-resolution STED microscopy to image the assemblies of Halo-BOK in the mitochondria of cells that had undergone Smac release (Figs. 5I and 6A). As shown in (Fig. 6b), we found that BOK organized into a mixture of structures, among which, in addition to dots, we could identify rings, arcs and lines. The resolved structures have a mean area around 0.2 μm^2, which corresponds to an average diameter of 0.5 µm assuming a circular shape (Fig. 6C). Remarkably, these BOK assemblies were similar to those observed for BAX and BAK involved in mitochondrial permeabilization, suggesting that all three proteins follow a similar mechanism to permeabilize mitochondria.

DISCUSSION

Even after more than 20 years of its discovery, the exact role of BOK in apoptosis continues to be puzzling [7, 42]. A body of

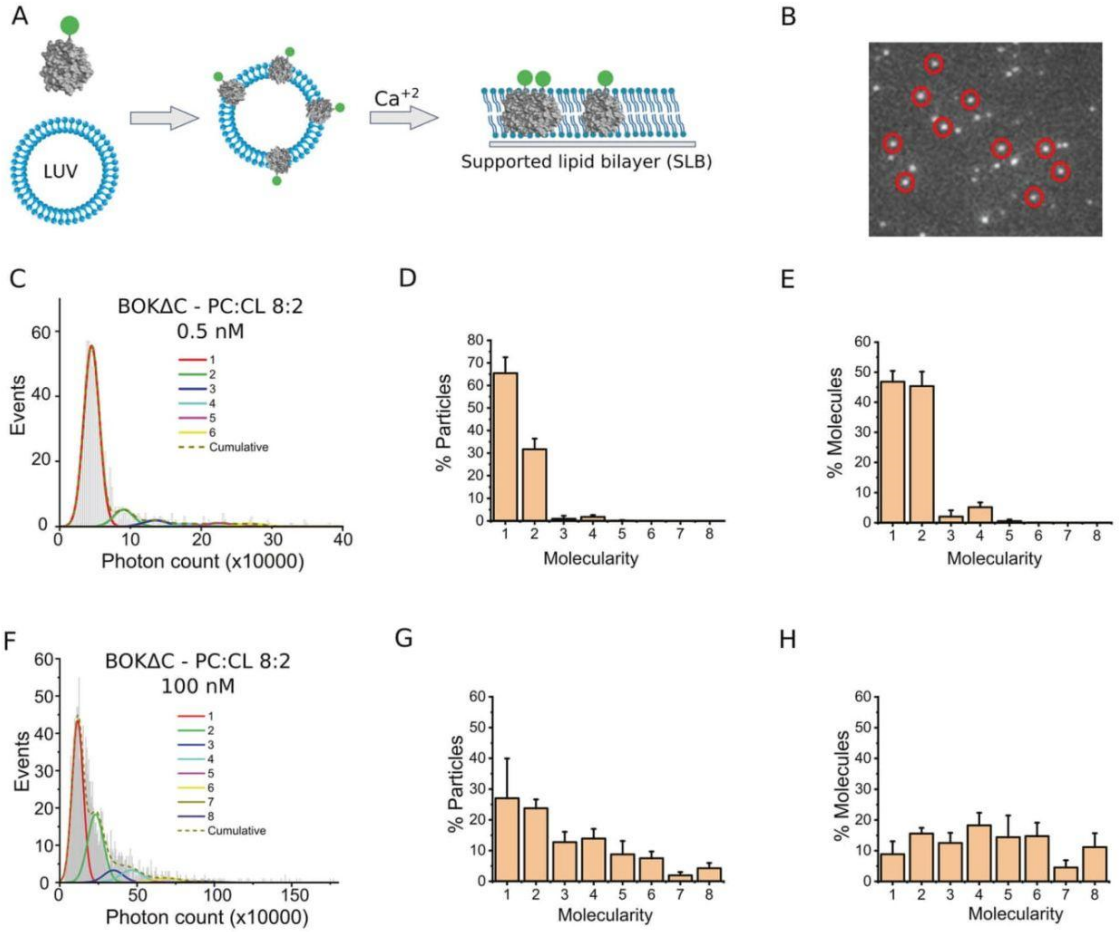

Fig. 3 BOKΔC oligomerizes into multiple coexisting species in SLB. A, **B** Schematic representation of the single-molecule stoichiometry analysis. (**A**) BOKΔC labelled with Atto488 dye was incubated with the LUVs with the composition PC:CL 8:2, followed by the formation of SLB on coverslip using calcium chloride. **B** Single particles of BOKΔC labelled with Atto488 dye bound to SLB formed from PC:CL 8:2 liposomes resolved with TIRF microscope. **C**–**H** Analysis of Atto488-BOKΔC oligomerization in the membrane. Particle fluorescence intensity distribution from different experiments were fitted with a linear combination of eight Gaussians to estimate the abundance of different molecularities. The cumulative fit is shown as a dashed line. The percentage of each species is derived from the area under each fitted Gaussian. The error bars correspond to the average error for each oligomeric species from three independent experiments with Particles >500 per condition per experiment.

evidence has now accumulated supporting the classification of BOK as an effector of the BCL-2 family. Here, we provide direct visualization of BOK pores and compare their properties to those of BAX and BAK.

Using in vitro and in cell experiments, we found that BOK can induce membrane permeabilization independent of BAX and BAK. While the C-terminal anchor involved in membrane targeting was not necessary for membrane permeabilization, it contributed to protein thermostability. A possible explanation to the increased thermostability of FL-BOK is the formation of domain-swaped dimers that were shown before to inhibit BAX [43]. It is generally accepted that BAX and BAK can be activated by cBID to form pores in cells and artificial membranes [33], while this has remained less clear in the case of BOK [10, 16]. Yet, in vitro, both BAX and BAK, as well as FL-BOK shown here, can be activated by temperature, without the need for direct activators [29, 44]. This effect of temperature might be explained by promoting protein unfolding and exposure of helices involved in interaction with the membrane, which then would drive membrane insertion and pore formation. The lack of the C-terminal helix of BOK could cause decreased stability, manifested in lower melting temperature and pore activity at room temperature.

BOK has been considered a pro-apoptotic member of the BCL-2 family based on the structural homology with both BAX and BAK and on genetic studies [15]. While the majority of apoptotic stimuli cannot induce apoptosis in cell lacking BAX and BAK [41, 42], apoptosis could be triggered in these cell lines by proteasome inhibitors which correlated with BOK stabilization [13]. Accordingly, we found that overexpression of GFP-BOK induced apoptosis not only in cells knock out for both BAX and BAK, but also in cells lacking the most relevant BCL-2 family members. This indicates that the pro-apoptotic activity of BOK in cells not only does not require BAX and BAK, but also discards any potential mechanism involving a phenotypic switch of anti-apoptotic BCL-2 proteins. Since the extent of BOK-induced cell death was not affected by the presence pro-survival family members, they cannot inhibit BOK pores either.

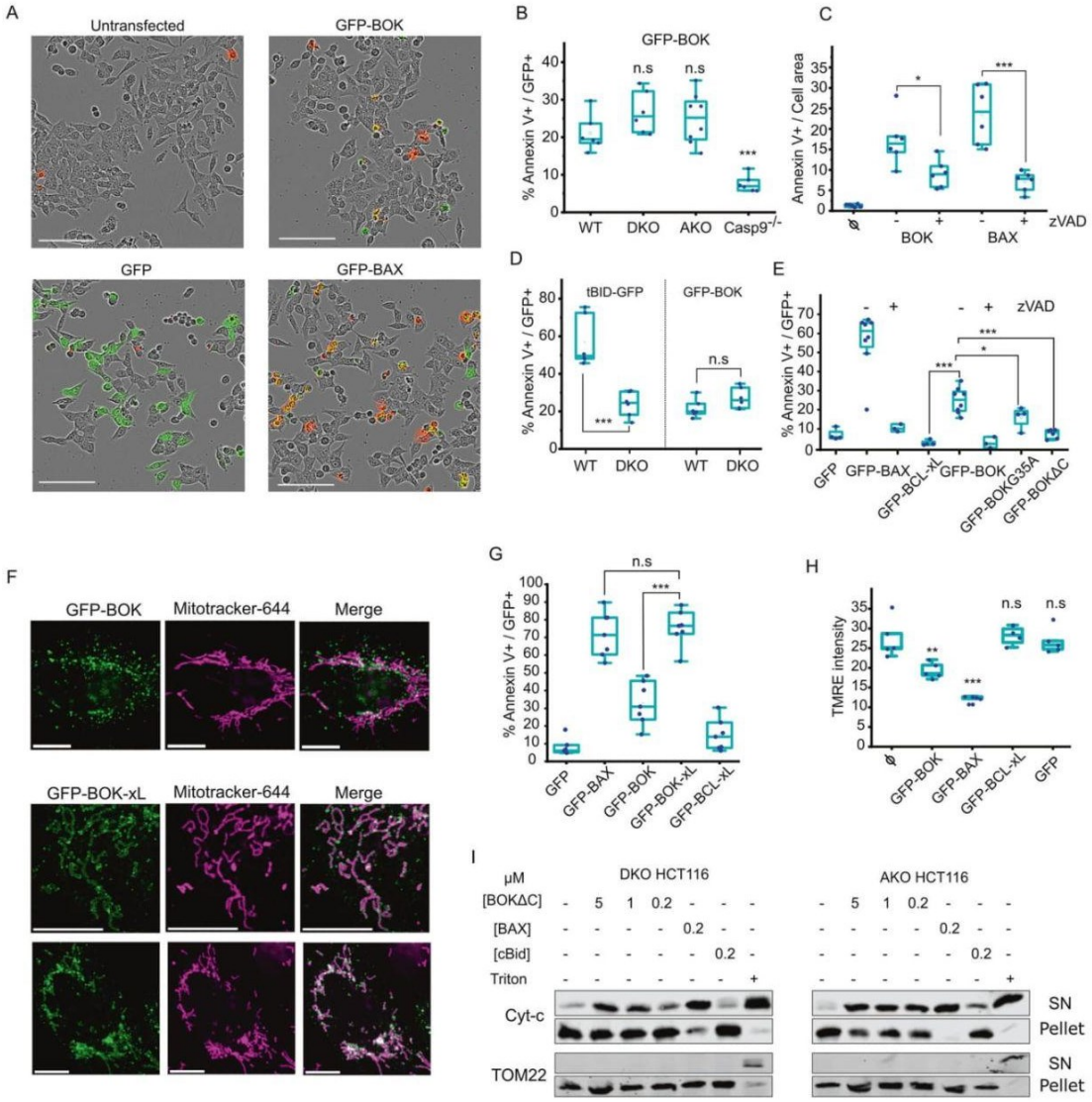

Fig. 4 Apoptosis induction by BOK is comparable to and independent of BAX and BAK. A Representative images of HCT-AKO cells expressing GFP-BAX, GFP-BOK and GFP 16 h after transfection. Transfected cells and annexin V+ cells appear in green and red respectively. Scale bar; 100 μm. **B** Effect of GFP-BOK overexpression on cell death in different cell lines (HCT-WT, DKO, AKO and Casp9 KO), measured as percentage of cells with Annexin V from the total transfected cells (Annexin V+/GFP+). **C** Effect of BAX and BOK overexpression on cell death in HCT AKO, in the presence or absence of ZVAD, measured as fraction of cells with Annexin V normalized to total cell area. **D** Effect of tBID-GFP and GFP-BOK overexpression on cell death in different cell lines (HCT-WT and DKO) quantified as in **B**. **E** Effect of GFP-BAX, GFP-BOK, GFP-BOK G35A, GFP-BOKΔC, GFP-BCL-xL and GFP overexpression on cell death in HCT AKO, in the presence or absence of ZVAD and calculated as in (**B**). ϕ: untransfected. **F** Representative images of GFP-BOK and GFP-BOK-xL subcellular localization 16 h after transfection in U2OS BAX$^{-/-}$/BAK$^{-/-}$ cells. BOK appears depicted in green and mitochondria (labelled with Mitotracker-644) in magenta. Scale bar, 10 μm. **G** Effect of GFP-BAX, GFP-BOK, GFP-BOK-xL, GFP-BCL-xL and GFP overexpression on cell death in HCT AKO quantified as in **B**. **H** Effect of GFP-BAX, GFP-BOK, GFP-BCL-xL and GFP overexpression on mitochondrial depolarization in U2OS DKO cells, measured as a decrease on TMRE signal. ϕ: untransfected. **I** Release of cytochrome c from isolated mitochondria from HCT116 cells was assessed by immunoblotting of pellet (mitochondria) and supernatant fractions. Antibody against TOM22 was used as a control. ***$P \leq 0.001$, **$P \leq 0.01$, *$P \leq 0.05$, ns not significant. Experiments were averages of at least three replicates.

We could directly visualize BOK-induced pores in liposomes using EM, whose features suggest that they are of toroidal (or lipidic) nature, as proposed for BAX and BAK [45]. Protein density could not be located at the pore edge [40] and the pore size was flexible and increased with protein density on the membrane. Also in agreement with a BAX-like toroidal pore, the single-molecule analysis of BOK stoichiometry revealed that BOK existed in membranes as a mixture of oligomeric species that grew into larger assemblies with protein density in the membrane.

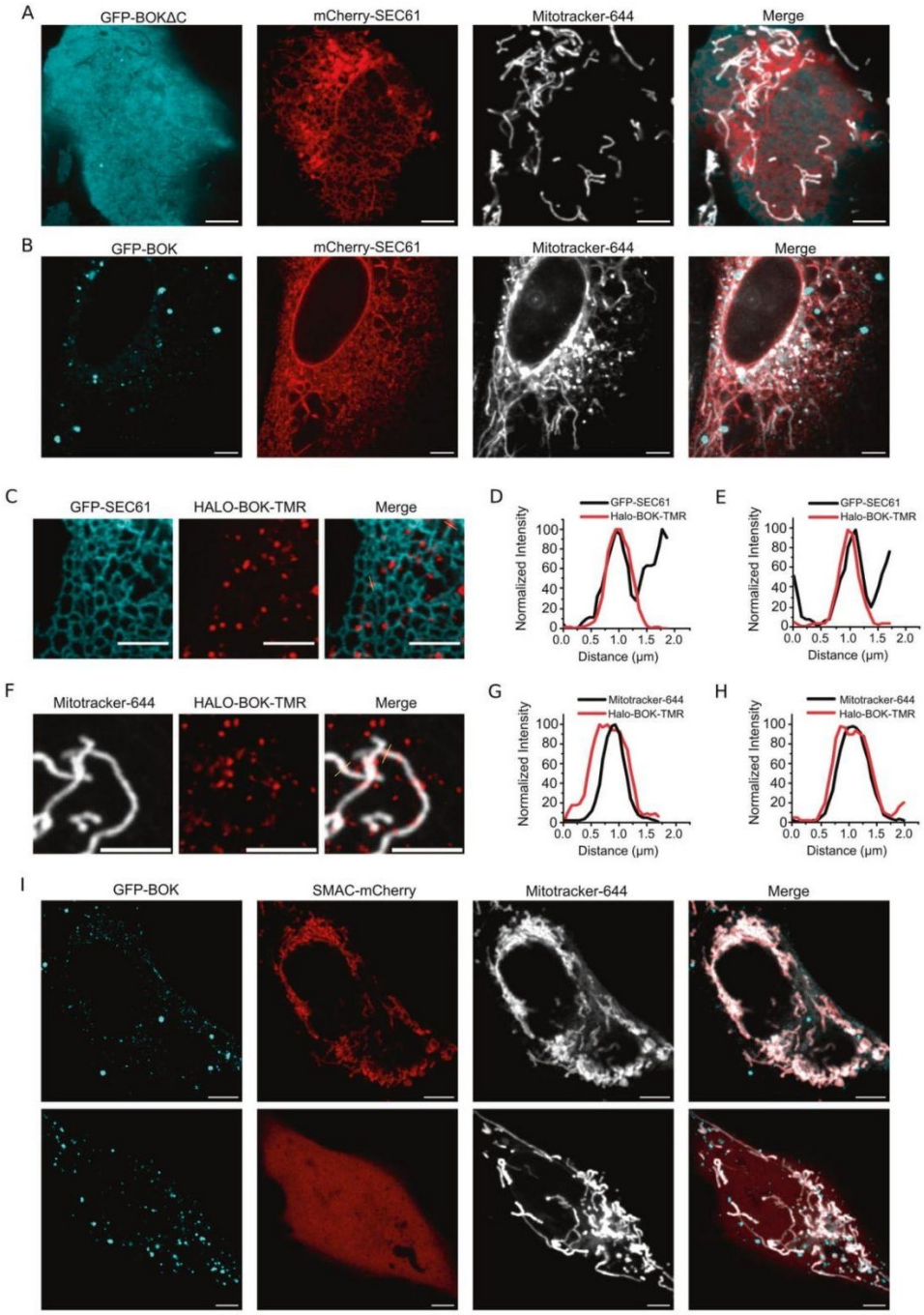

Fig. 5 BOK localizes partially to mitochondria and to the ER via its C-terminal anchoring domain. A, B Representative images of GFPBOKΔC and GFP-BOK subcellular localization 16 h after transfection in U2OS $BAX^{-/-}/BAK^{-/-}$ cells. BOK appears depicted in cyan, ER (marked with SEC-61) in red and mitochondria (labelled with Mitotracker-644) in grey. **C, F** Representative images of HALO-BOK subcellular localization. BOK appears depicted in red, ER (marked with SEC-61) in cyan and mitochondria (labelled with Mitotracker) in grey. **D–H** Line profile of HALO-BOK clusters signal together with the ER (**D, E**, SEC61) or mitochondrial signal (**G, H**, Mitoctracker-644). Lines are shown in **C, F**. Intensity was normalized to 100. **I** Representative images of GFP-BOK subcellular localization and MOMP induction. BOK appears depicted in cyan, Smac-mCherry in red and mitochondria in grey. Scale bar for all images, 5 μm.

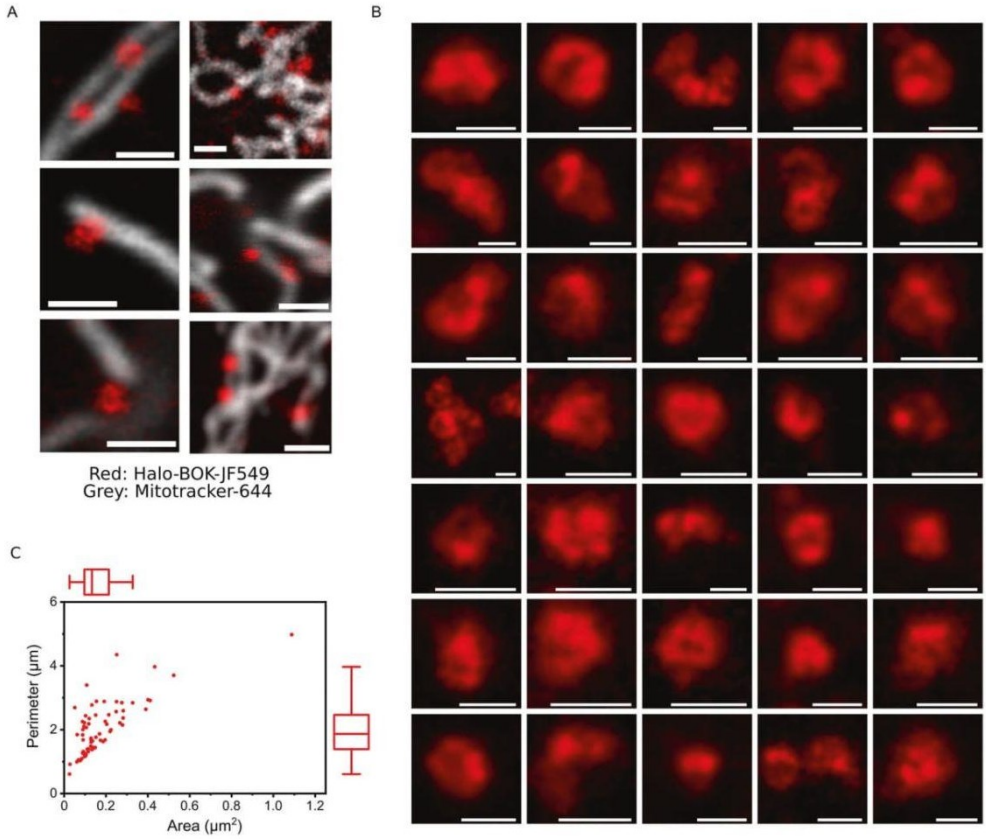

Fig. 6 BOK forms ring-like structures in apoptotic mitochondria. A Representative images of Halo-BOK-JF549 16 h after transfection in U2OS $BAX^{-/-}/BAK^{-/-}$ cells, localized to mitochondria (stained with Mitotracker) acquired by STED microscopy. Scale bar, 1 µm. **B** A gallery of the structures formed by BOK, acquired by STED microscopy. Scale bar, 400 nm. **C** Summary of the structures formed by BOK. Perimeter is plotted against Area after image binarization.

Importantly, we were able to detect ring-shaped nanostructures of BOK directly in the mitochondria of apoptotic cells with a similar organization to those found for BAX and BAK using super-resolution microscopy [35, 46]. This suggests that BOK induces mitochondrial permeabilization in cells via a common molecular mechanism with the effector BCL-2 proteins, even if its regulation differs from that of BAX and BAK.

Also in contrast to BAX and BAK, overexpressed BOK accumulated at discrete sites co-localizing with mitochondria, the ER and likely other cellular membranes. Considering that mitochondrial permeabilization requires localization to this organelle, we propose that limited BOK localization to mitochondria is a key mechanism to control BOK pore formation and apoptosis induction. We provide evidence supporting this model by using chimeras of BOK with the C-terminal of BCL-xL, which efficiently target to mitochondria and become as potent as BAX in inducing cell death. According to this model, BOK-mediated apoptosis would be regulated by its mitochondrial accumulation, for example via upregulation via proteosomal degradation as reported by Llambi et al. in [13], or by alternative mechanisms controlling BOK localization that remain to be explored. A recent study reported that BOK levels were upregulated by the SARS-CoV-2 membrane protein (M), leading to apoptosis and lung edema in mice [47], which may open opportunities for BOK targeted interventions against COVID-19.

In summary, here we provide direct visualization of BOK membrane pores that share mechanistic properties with the pores formed by the apoptotic effectors BAX and BAK. We also show that the regulation of BOK permeabilizing activity is however different from BAX and BAK, and independent of other BCL-2 proteins. Our data support a model in which BOK apoptotic activity is controlled by subcellular localization and membrane lipid composition.

MATERIALS AND METHODS

Recombinant protein expression and purification

BOK gene (Full length (FL-BOK) and a truncated version lacking the last 24 residues (BOKΔC)) were cloned into a pETM-11 plasmid (EMBL), containing an N-terminal 6xHis tag. To enable fluorescent labeling of BOKΔC using sortase A enzyme, three glycine residues were added to the N-terminus of the protein (^{3G}BOKΔC) and the gene was cloned into a pTYB21 plasmid (New England Biolabs), containing an N-terminal intein tag. BL21-(DE3)-RIPL *E. coli* (Agilent Technologies) were transformed with the expression plasmids, and was grown in LB media containing the corresponding resistance antibiotics. Protein expression was induced at OD = 1, using 1 mM isopropyl-β-D-thiogalactoside for 4 h at 18 °C. The bacteria were then retrieved by centrifugation, resuspended in Lysis buffer (20 mM Tris, 1 M NaCl, 1 mM PMSF, pH 8) and were then lysed by sonication. Afterwards, the lysate was cleared by centrifugation at 20,000 g for 1 h. The supernatant of 6xHis tag fusion proteins were incubated with Ni-NTA agarose beads (Qiagen) and eluted with 250 mM imidazole, While the supernatant of

intein-tagged ^{3G}BOKΔC was incubated with chitin beads (New England Biolabs) and eluted by incubation with 50 mM DTT for 40 h at 4 °C. The eluted fractions were then concentrated and injected on a Superedx 75 Increase 10/300 GL Size exclusion column (Cytiva). Protein purity was examined by SDS–polyacrylamide gel electrophoresis. Protein quantification was performed using Nanodrop and protein identity was further confirmed with Mass spectrometry. Cleaved Bid (cBID) and BAX were produced as previously described [18, 21].

Protein fluorescent labeling

^{3G}BOKΔC was fluorescently labeled using sortase A enzyme and an Atto488-conjugated peptide containing the sortase-recognition motif (LPRTG) [48]. This results in the conjugation of the dye only to the N-terminus of the protein, which is crucial for the accurate estimation of the stoichiometry of the protein. ^{3G}BOKΔC was incubated with sortase A (0.3 molar equivalent) and Atto488-peptide (20 molar equivalent) in sortase buffer (20 mM Tris, 150 mM NaCl, 5 mM $CaCl_2$, pH 7) at room temperature for 30 min. After that, the reaction mixture was passed through a desalting column (PD10, 25 G, GE healthcare) to remove unreacted peptide. Fractions containing protein were combined and then incubated with Ni-NTA agarose beads (Qiagen) for 30 min to remove the His-tagged sortase A. The labeled protein was then aliquoted and stored at −80 °C.

Liposome permeabilization assay

Lipids were purchased from Avanti Polar Lipids, and were dissolved in chloroform and mixed with the desired molar ratios. Chloroform was then evaporated under vacuum for 3 h. Large unilamellar vesicles (LUVs) were prepared using the extrusion method as described before [49, 50]. Briefly, the lipid film was hydrated with 80 mM solution of the fluorescent dye calcein, pH 7 for a final lipid concentration of 5 mg/mL followed by five cycles of freezing and thawing. The lipid solution was then extruded through a polycarbonate membrane with a pore size of 100 nm using glass syringes. Calcein-loaded LUVs were separated from free calcein using Sephadex-G50 beads and the lipid concentration was adjusted to 100 μM. LUVs were incubated with serial dilutions of the recombinant proteins in a 96-well plate and calcein release was monitored by fluorescence emission at 520 nm with excitation at 490 nm for 1 h using a microplate reader (Enspire, PerkinElmer). 0.1% Triton X-100 was used as a positive control (100% calcein release) and the percentage of calcein release was calculated as follows:

$$\%Calcein\ release = 100 \times \frac{[F_{Sample} - F_{Buffer}]}{[F_{Triton} - F_{Buffer}]}$$

Thermal shift assay

BOKΔC, FL-BOK and BAX were diluted to 4 μM in PBS (pH 7.4) in a total reaction volume of 20 μL with SYPRO Orange (Sigma-Aldrich) used as a probe. The reaction mixture was dispensed in Microamp Fast Optical 96-well reaction plates (ThermoFisher) and analyzed in a C1000 thermal cycler (Bio-Rad). Protein melting temperature was estimated from the first derivative of fluorescence emission with respect to temperature.

Negative staining electron microscopy

LUVs (PC:CL 8:2) were incubated with BOKΔC, FL-BOK, BAX (+40 nM cBID) and GSDMD (+20 nM caspase11) for 40 min. The protein:lipid molar ratio was adjusted to 1:100 or 1:10000. Afterwards, the proteoliposomes were placed onto a glow-discharged copper grid (Electron Microscopy Sciences) coated with a layer of thin carbon, washed twice with water, stained with 2% uranyl acetate for 5 min and then air-dried. The grids were imaged on a JEOL JEM2100PLUS electron microscope and recorded with a GATAN OneView camera (CECAD imaging Facility).

Supported lipid bilayers (SLBs)

For the formation of LUVs, lipid mixtures were rehydrated to a final concentration of 10 mg/mL in PBS, pH 7.4. 10 μL of the multilamellar vesicle suspension was then diluted in 140 μL of SLB buffer (10 mM HEPES, 150 mM NaCl, pH 7.4). The suspension was then subjected to five cycles of freezing-thawing and was then extruded through a polycarbonate membrane with 100 nm pore size using a glass syringe. Atto488-BOKΔC was first incubated at different concentrations with LUVs made of PC:CL (8:2) for 40 min at room temperature to form proteoliposomes. The proteoliposomes were then diluted with empty liposomes (to be in the single-molecule regime) and were incubated at 37 °C for 2 min with 3 mM $CaCl_2$ on plasma-cleaned glass slides (0.15 mm thickness). Afterwards, the SLB was rinsed several times with SLB buffer to remove non-fused vesicles. The SLB was then immediately imaged with TIRF microscopy. At least 500 particles were detected and analyzed per replica in each experiment.

TIRF Microscopy

SLBs were imaged using a modified Zeiss Axiovert 20 M epifluorescence microscope with a 488 nm laser equipped with a 100x/1.46 oil objective (Zeiss), a Laser-TIRF 3 Imaging System (Zeiss) and an EM-CCD camera (iXon 897, Andor). Exposure time was set to 35 ms with a delay time between frames of 25 ms and an intensity of 0.1 kW/cm2. The images acquired were used for the stoichiometry analysis based on the fluorescence intensity of the particles using an in-house algorithm implemented in Python.

Stoichiometry analysis

The images acquired were used for the stoichiometry analysis based on the fluorescence intensity of the particles. Bright spots were detected using the difference of Gaussians method and thresholding and were then fitted to two-dimensional (2D) Gaussians and the background was subtracted. Localized particles were filtered based on the distance and on the width of the 2D Gaussian, to avoid overlapping regions of interest (ROIs) or multiple particles in the same ROI. Brightness value for each particle was calculated from the area under the 2D Gaussian. The brightness of particles was used to decipher the stoichiometry of the proteins as previously described [28, 35]. Briefly, Atto488-BOKΔC was spread on a glass slide and individual particles with a single photobleaching step were detected and were fitted to a Gaussian to estimate the mean intensity (μ) and standard deviation (σ) of a monomer. Then, the mean brightness of different oligomers (N) was calculated from the equation: $\mu_N = N\mu_1 \pm \sigma_1\sqrt{N}$. The number of Gaussians that can be fitted to the distribution of fluorescence intensity was estimated according to equation [51]: $N_{max} = (\mu_1/\sigma_1)^2$.

Mitochondrial isolation and cytochrome c release assay

DKO HCT 116 and AKO HCT116 cells were harvested and resuspended in MB buffer (10 mm HEPES, 210 mm mannitol, 70 mm sucrose, 1 mm EDTA, pH 7.5) supplemented with Complete Protease Inhibitor Cocktail (Roche). Afterwards, the cells were disrupted by passing 20 times through a 27 G needle, and the debris was removed by centrifugation at 1500 g. Mitochondria were then obtained by centrifugation at 7000 g for 10 min. The pellet was then resuspended in MB buffer and protein concentration was determined by Bradford assay (Biorad). For the cytochrome c release assays, 30 μg of mitochondria was incubated with BOKΔC, BAX and cBID in RB buffer (10 mM HEPES, 125 mM KCl, 0.5 mM EGTA, pH 7.4) for 30 min at 37 °C. The samples were centrifuged for 10 min at 14,000 g and the presence of cytochrome c in the pellet and supernatant was determined by western blotting using a mouse monoclonal anti-cytochrome c antibody clone 7H8.2C12 (BD-Biosciences). Anti-TOM22 antibody (#:sc-101286, Santa Cruz) was used as a control.

Mammalian cell culture and transfection

HCT116 cells (WT, $BAX^{-/-}BAK^{-/-}$ (DKO), kindly provided by Prof. Schulze-Ohsthoff, and all Bcl-2 proteins knock out (AKO)) were used in the quantification of cell death activity using IncuCyte (Sartorius) and were grown in McCoy's 5 A modified medium (Sigma-Aldrich). Caspase-9 CRISPR/Cas9 knock out were generated in HCT116 WT cells. For CRISPR transfection, 1–2 × 105 cells were seeded in a 6-well plate 48 h before transfection. 500 ng of CRISPR construct was transfected with 1 μL of Lipofectamine 2000 (Thermo Fisher) according to manufacturer's instructions. 24 h after transfection cells were transferred to a 15 cm dish and selected for seven days with media supplemented with 0.5 μg/mL puromycin. Single colonies were picked and cultured for validation. Success of the knock out was validated using Western blotting and genotyping by Sanger's sequencing of the target region. The following guide RNA sequence were used for the generation of CASPASE-9 CRISPR/Cas9 knock out cell lines: CAACTTCTCACAGTCGATGTTtgg. Pairs of oligonucleotides containing the gRNA sequence were cloned into the pSpCas9(BB)-2A-Puro V2.0 (px459, Addgene #62988) using the restriction

enzyme BbsI (NEB). U2OS BAX$^{-/-}$BAK$^{-/-}$ cells were used for TMRE assay and for confocal and STED microscopy and were grown in low-glucose Dulbecco's modified Eagle's medium (DMEM) (Sigma-Aldrich). All media were supplemented with 10% fetal bovine serum (FBS) and 1% penicillin-streptomycin (Thermo Fisher). Cells were transfected with plasmid DNA using Lipofectamine 2000 (Invitrogen) according to the manufacturer's protocol.

IncuCyte cell death assays

Cell death assays were performed using IncuCyte S3 (Sartorius) at 37 °C 5% CO_2. Apoptotic cell death was measured by the binding of Annexin V Alexa 647 (Invitrogen) to cells, which indicates the exposure of Phosphatidylserine. HCT116 cells were seeded (5000 cells/well) in a 96 well plate for 24–48 h and then transfected with 25 ng/well of plasmid DNA using lipofectamine 2000 (Invitrogen) according to the manufacturer's protocol. Prior to transfection, the medium was replaced with medium containing 1:200 Annexin V Alexa. Four images per well were acquired every 1 h for 24 h. The images were then analyzed using IncuCyte basic analysis software module.

TMRE Mitochondrial Membrane Potential Assay

U2OS BAX$^{-/-}$BAK$^{-/-}$ cells were seeded (1000 cells/well) in a 48-well plate for 24–48 h and then transfected with 50 ng/well of plasmid DNA using lipofectamine 2000 (Invitrogen) according to the manufacturer's protocol. Prior to transfection, the medium was replaced with medium containing 100 nM TMRE dye (Invitrogen). Live cell imaging was performed using IncuCyte S3 (Sartorius) as described above. Nine images per well were aquired every 1 h for 24 h. The images were analyzed using IncuCyte Cell-by-Cell analysis software module. TMRE signal was calculated from the integrated intensity in each cell.

Confocal and STED microscopy

For Confocal imaging, U2OS BAX$^{-/-}$BAK$^{-/-}$ cells seeded on coverslips were transfected with (Halo-BOK, GFP-BOK or GFPBOKΔC) and (GFPSEC61 or mCherry-SEC61) and then treated with 10 µM QVD. 16 h after transfection, the cells were incubated with 150 nM MitoTracker Deep Red (Thermo Fisher) and HaloTag TMR Ligand (Promega) (when transfecting with Halo-BOK) for 20 min at 37 °C. The cells were then washed 3 times with fresh media and were fixed using Paraformaldehyde. Imaging was performed on a TCS SP8 confocal laser scanning microscope (Leica Microsystems) equipped with a PL Apo 63x/1.40 Oil CS2 objective and a tunable white light laser (470–670 nm). The signal was acquired with sensitive HyD detectors (Leica Microsystems).

For STED imaging, U2OS BAX$^{-/-}$BAK$^{-/-}$ cells seeded on coverslips were transfected with Halo-BOK and Smac-GFP and then treated with 10 µM QVD. 16 h after transfection, the cells were incubated with 0.3 µM Janelia Fluor 549 HaloTag Ligand (Promega) and 150 nM MitoTracker Deep Red (Thermo Fisher) for 20 min at 37 °C. The cells were then washed 3 times with fresh media and were fixed using Paraformaldehyde. Images were acquired using TCS SP8 gSTED microscope (Leica Microsystems) equiped with HL PL APO 100x/1.40 Oil STED, a tunable white light laser (470–670 nm) and 750 nm depletion laser. The signal was acquired with sensitive HyD detectors (Leica Microsystems).

DATA AVAILABILITY

The data that support the findings of this study are included in the article or uploaded as Supplementary Information and all original data are available from the corresponding author upon request.

REFERENCES

1. Singh R, Letai A, Sarosiek K. Regulation of apoptosis in health and disease: the balancing act of BCL-2 family proteins. Nat Rev Mol Cell Biol. 2019;20:175–93.
2. Czabotar PE, Lessene G, Strasser A, Adams JM. Control of apoptosis by the BCL-2 protein family: implications for physiology and therapy. Nat Rev Mol Cell Biol. 2014;15:49–63.
3. Flores-Romero H, García-Sáez AJ. The Incomplete Puzzle of the BCL2 Proteins. Cells 2019;8:10.
4. Kale J, Osterlund EJ, Andrews DW. BCL-2 family proteins: changing partners in the dance towards death. Cell Death Differ. 2018;25:65–80.
5. Edlich F, Banerjee S, Suzuki M, Cleland MM, Arnoult D, Wang C, et al. Bcl-x(L) retrotranslocates Bax from the mitochondria into the cytosol. Cell 2011;145:104–16.
6. Todt F, Cakir Z, Reichenbach F, Youle RJ, Edlich F. The C-terminal helix of Bcl-x(L) mediates Bax retrotranslocation from the mitochondria. Cell Death Differ. 2013;20:333–42.
7. Naim S, Kaufmann T. The Multifaceted Roles of the BCL-2 Family Member BOK. Front Cell Dev Biol. 2020;8:574338.
8. Llambi F, Wang Y-M, Victor B, Yang M, Schneider DM, Gingras S, et al. BOK Is a Non-canonical BCL-2 Family Effector of Apoptosis Regulated by ER-Associated Degradation. Cell 2016;165:421–33.
9. Ke FFS, Vanyai HK, Cowan AD, Delbridge ARD, Whitehead L, Grabow S, et al. Embryogenesis and Adult Life in the Absence of Intrinsic Apoptosis Effectors BAX, BAK, and BOK. Cell 2018;173:1217–30.e17.
10. Zheng JH, Grace CR, Guibao CD, McNamara DE, Llambi F, Wang Y-M, et al. Intrinsic Instability of BOK Enables Membrane Permeabilization in Apoptosis. Cell Rep. 2018;23:2083–94.e6.
11. Kvansakul M, Hinds MG. Structural biology of the Bcl-2 family and its mimicry by viral proteins. Cell Death Dis. 2013;4:e909.
12. Gavathiotis E, Reyna DE, Davis ML, Bird GH, Walensky LD. BH3-triggered structural reorganization drives the activation of proapoptotic BAX. Mol Cell. 2010;40:481–92.
13. Kuwana T, Olson NH, Kiosses WB, Peters B, Newmeyer DD. Pro-apoptotic Bax molecules densely populate the edges of membrane pores. Sci Rep. 2016;6:27299.
14. Flores-Romero H, Garcia-Porras M, Basanez G. Membrane insertion of the BAX core, but not latch domain, drives apoptotic pore formation. Sci Rep. 2017;7:16259.
15. Hsu SY, Kaipia A, McGee E, Lomeli M, Hsueh AJW. Bok is a pro-apoptotic Bcl-2 protein with restricted expression in reproductive tissues and heterodimerizes with selective anti-apoptotic Bcl-2 family members. Proc Natl Acad Sci. 1997;94:12401–6.
16. Fernández-Marrero Y, Bleicken S, Das KK, Bachmann D, Kaufmann T, Garcia-Saez AJ. The membrane activity of BOK involves formation of large, stable toroidal pores and is promoted by cBID. FEBS J. 2017;284:711–24.
17. Suzuki M, Youle RJ, Tjandra N. Structure of Bax: coregulation of dimer formation and intracellular localization. Cell 2000;103:645–54.
18. Bleicken S, Wagner C, García-Sáez AJ. Mechanistic differences in the membrane activity of Bax and Bcl-xL correlate with their opposing roles in apoptosis. Biophys J. 2013;104:421–31.
19. Echeverry N, Bachmann D, Ke F, Strasser A, Simon HU, Kaufmann T. Intracellular localization of the BCL-2 family member BOK and functional implications. Cell Death Differ. 2013;20:785–99.
20. Kuwana T, Mackey MR, Perkins G, Ellisman MH, Latterich M, Schneiter R, et al. Bid, Bax, and lipids cooperate to form supramolecular openings in the outer mitochondrial membrane. Cell 2002;111:331–42.
21. Bleicken S, Landeta O, Landajuela A, Basañez G, García-Sáez AJ. Proapoptotic Bax and Bak proteins form stable protein-permeable pores of tunable size. J Biol Chem. 2013;288:33241–52.
22. Flores-Romero H, Landeta O, Ugarte-Uribe B, Cosentino K, García-Porras M, García-Sáez AJ, et al. BFL1 modulates apoptosis at the membrane level through a bifunctional and multimodal mechanism showing key differences with BCLXL. Cell Death Differ. 2019;26:1880–94.
23. Landeta O, Garcia Valero J, Flores-Romero H, Bustillo-Zabalbeitia I, Landajuela A, Garcia-Porras M, et al. Lipid-dependent bimodal MCL1 membrane activity. ACS Chem Biol. 2014;9:2852–63.
24. Singh G, Guibao CD, Seetharaman J, Aggarwal A, Grace CR, McNamara DE, et al. Structural basis of BAK activation in mitochondrial apoptosis initiation. Nat Commun. 2022;13:250.
25. Sandow JJ, Tan IK, Huang AS, Masaldan S, Bernardini JP, Wardak AZ, et al. Dynamic reconfiguration of pro-apoptotic BAK on membranes. EMBO J. 2021;40:e107237.
26. Oh KJ, Singh P, Lee K, Foss K, Lee S, Park M, et al. Conformational Changes in BAK, a Pore-forming Proapoptotic Bcl-2 Family Member, upon Membrane Insertion and Direct Evidence for the Existence of BH3-BH3 Contact Interface in BAK Homo-oligomers. J Biol Chem. 2010;285:28924–37.
27. Bleicken S, Hofhaus G, Ugarte-Uribe B, Schröder R, García-Sáez AJ. cBid, Bax and Bcl-xL exhibit opposite membrane remodeling activities. Cell Death Dis. 2016;7:e2121.
28. Subburaj Y, Cosentino K, Axmann M, Pedrueza-Villalmanzo E, Hermann E, Bleicken S, et al. Bax monomers form dimer units in the membrane that further self-assemble into multiple oligomeric species. Nat Commun. 2015;6:8042.
29. Pagliari LJ, Kuwana T, Bonzon C, Newmeyer DD, Tu S, Beere HM, et al. The multidomain proapoptotic molecules Bax and Bak are directly activated by heat. Proc Natl Acad Sci USA. 2005;102:17975–80.
30. Landeta O, Landajuela A, Gil D, Taneva S, DiPrimo C, Sot B, et al. Reconstitution of proapoptotic BAK function in liposomes reveals a dual role for mitochondrial lipids in the BAK-driven membrane permeabilization process. J Biol Chem. 2011;286:8213–30.

31. Flores-Romero H, Ros U, Garcia-Saez AJ. Pore formation in regulated cell death. EMBO J. 2020:e105753.
32. Cowan AD, Smith NA, Sandow JJ, Kapp EA, Rustam YH, Murphy JM, et al. BAK core dimers bind lipids and can be bridged by them. Nat Struct Mol Biol. 2020;27:1024–31.
33. Terrones O, Antonsson B, Yamaguchi H, Wang H-G, Liu J, Lee RM, et al. Lipidic pore formation by the concerted action of proapoptotic BAX and tBID. J Biol Chem. 2004;279:30081–91.
34. Jenner A, Shalaby R, Cosentino K. Chapter Three - Quantitative single-molecule imaging of protein assembly in membranes. In: Iglič A, Rappolt M, García-SÁez AJ, eds. Advances in Biomembranes and Lipid Self-Assembly. 31: Academic Press; 2020. pp. 81-128.
35. Cosentino K, Hertlein V, Jenner A, Dellmann T, Gojkovic M, Peña-Blanco A, et al. The interplay between BAX and BAK tunes apoptotic pore growth to control mitochondrial-DNA-mediated inflammation. Mol Cell. 2022.
36. O'Neill KL, Huang K, Zhang J, Chen Y, Luo X. Inactivation of prosurvival Bcl-2 proteins activates Bax/Bak through the outer mitochondrial membrane. Genes Dev. 2016;30:973–88.
37. Flores-Romero H, Hohorst L, John M, Albert MC, King LE, Beckmann L. et al. BCL-2-family protein tBID can act as a BAX-like effector of apoptosis. EMBO J. 2022;41:e108690.
38. Carpio MA, Means RE, Brill AL, Sainz A, Ehrlich BE, Katz SG. BOK controls apoptosis by Ca transfer through ER-mitochondrial contact sites. Cell Rep. 2021;34:108827.
39. Means RE, Katz SG. Balancing life and death: BCL-2 family members at diverse ER-mitochondrial contact sites. FEBS J. 2021.
40. Nasu Y, Benke A, Arakawa S, Yoshida GJ, Kawamura G, Manley S, et al. In Situ Characterization of Bak Clusters Responsible for Cell Death Using Single Molecule Localization Microscopy. Sci Rep. 2016;6:27505.
41. Ader NR, Hoffmann PC, Ganeva I, Borgeaud AC, Wang C, Youle RJ, et al. Molecular and topological reorganizations in mitochondrial architecture interplay during Bax-mediated steps of apoptosis. Elife. 2019;8.
42. Shalaby R, Flores-Romero H, García-Sáez AJ. The Mysteries around the BCL-2 Family Member BOK. Biomolecules 2020;10:1638.
43. Garner TP, Reyna DE, Priyadarshi A, Chen HC, Li S, Wu Y, et al. An Autoinhibited Dimeric Form of BAX Regulates the BAX Activation Pathway. Mol Cell. 2016;64:431.
44. Westphal D, Dewson G, Czabotar PE, Kluck RM. Molecular biology of Bax and Bak activation and action. Biochim Biophys Acta. 2011;1813:521–31.
45. Flores-Romero H, Ros U, Garcia-Saez AJ. A lipid perspective on regulated cell death. Int Rev Cell Mol Biol. 2020;351:197–236.
46. Salvador-Gallego R, Mund M, Cosentino K, Schneider J, Unsay J, Schraermeyer U, et al. Bax assembly into rings and arcs in apoptotic mitochondria is linked to membrane pores. EMBO J. 2016;35:389–401.
47. Yang Y, Wu Y, Meng X, Wang Z, Younis M, Liu Y, et al. SARS-CoV-2 membrane protein causes the mitochondrial apoptosis and pulmonary edema via targeting BOK. Cell Death Differ. 2022.
48. Theile CS, Witte MD, Blom AEM, Kundrat L, Ploegh HL, Guimaraes CP. Site-specific N-terminal labeling of proteins using sortase-mediated reactions. Nat Protoc. 2013;8:1800–7.
49. García-Sáez AJ, Coraiola M, Serra MD, Mingarro I, Müller P, Salgado J. Peptides corresponding to helices 5 and 6 of Bax can independently form large lipid pores. FEBS J. 2006;273:971–81.
50. Menestrina G, Dalla Sera M. Pore-forming Peptides and Protein Toxins. CRC Press; 2003. p. 360.
51. Schmidt T, Schütz GJ, Gruber HJ, Schindler H. Local Stoichiometries Determined by Counting Individual Molecules. Anal Chem. 1996;68:4397–401.

ACKNOWLEDGEMENTS

We thank Christian Jüngst, Felix Babatz and Astrid Schauss from the CECAD Imaging Facility. We thank Xu Luo for providing AKO HCT116 cells and Jan Bierlmeier and Dirk Schwarzer for providing help with peptide synthesis and providing sortase A enzyme.

AUTHOR CONTRIBUTIONS

RS, AD and HF-R performed research and analyzed data. VH prepared materials. AJG-S conceived the project and supervised research. AJG-S and RS wrote the manuscript with the help of all other authors.

FUNDING

This project was funded by the Deutsche Forschungsgesellschaft (DFG, German Research foundation), SFB1403 – project no. 414786233, SFB1218 – project no. 269925409 and FOR2036 – project no. 232935877. Open Access funding enabled and organized by Projekt DEAL.

COMPETING INTERESTS

The authors declare no competing interests.

ETHICS APPROVAL

This study did not include animals, human participants, human data or human tissues.

ADDITIONAL INFORMATION

Supplementary information The online version contains supplementary material available at https://doi.org/10.1038/s41418-022-01078-w.

Correspondence and requests for materials should be addressed to Ana J. Garcia-Saez.

Reprints and permission information is available at http://www.nature.com/reprints

Publisher's note Springer Nature remains neutral with regard to jurisdictional claims in published maps and institutional affiliations.

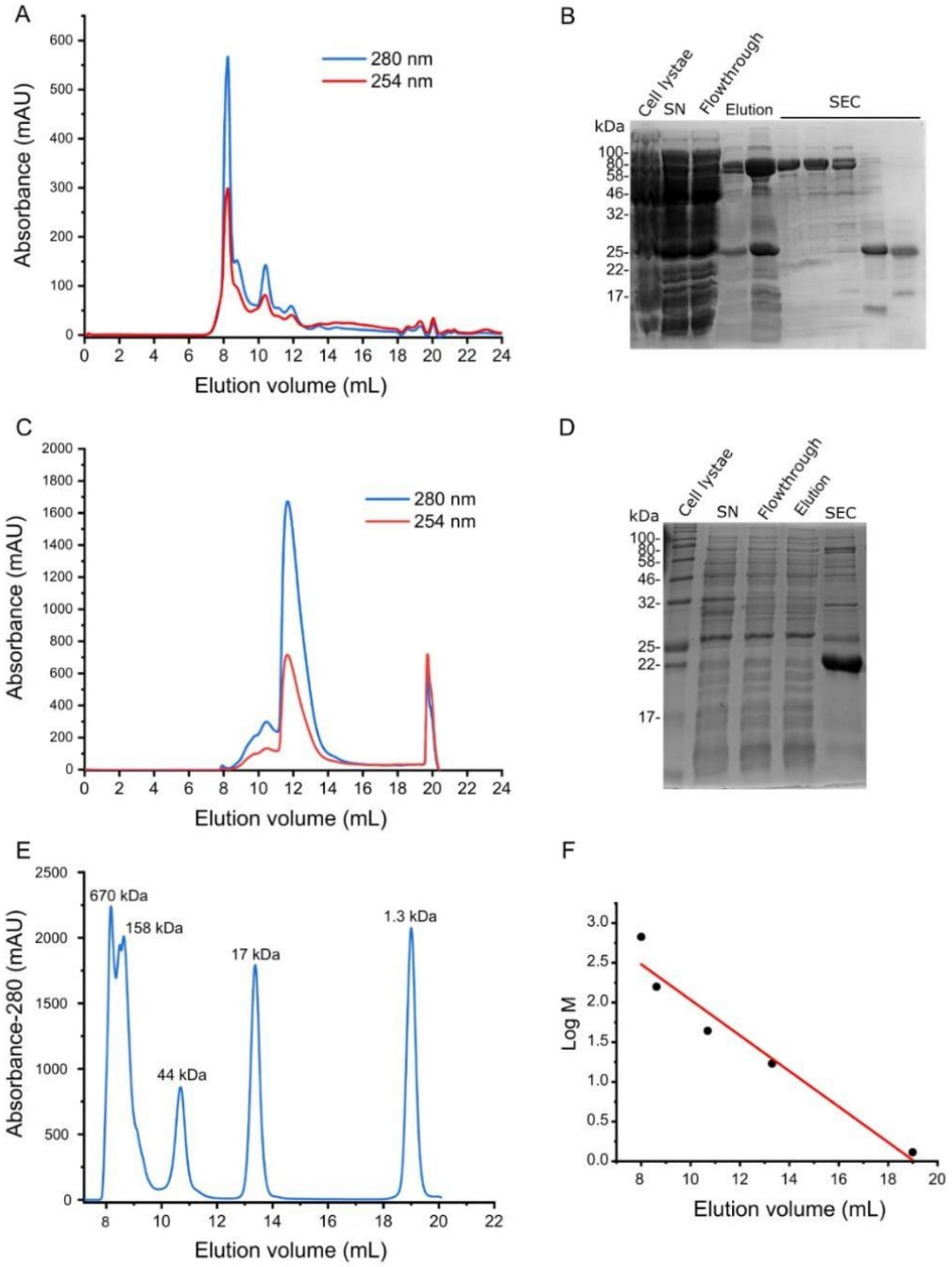

Figure S1. Purification of recombinant BOKΔC and FL-BOK

(A) SEC Chromatogram from Superdex75 column after injection of the elution fraction of FL-BOK (B) Representative Coomassie-stained SDS-PAGE gel for the steps of the purification process of recombinant FL-BOK. SN: supernatant after lysis and centrifugation, SEC: size-exclusion chromatography for fractions from 7 to 11 mL. (C,D): The same as in (A,B) but for the purification of BOKΔC. (SEC fraction in the SDS-PAGE corresponds to the peak with maxima at 12 mL). (E) SEC Chromatogram from Superdex75 column using a mixture of proteins with different molecular weights (Gel Filtration Standard, Bio-rad #1511901). (F) Calibration curve of Superdex75 column derived from elution profile in (E).

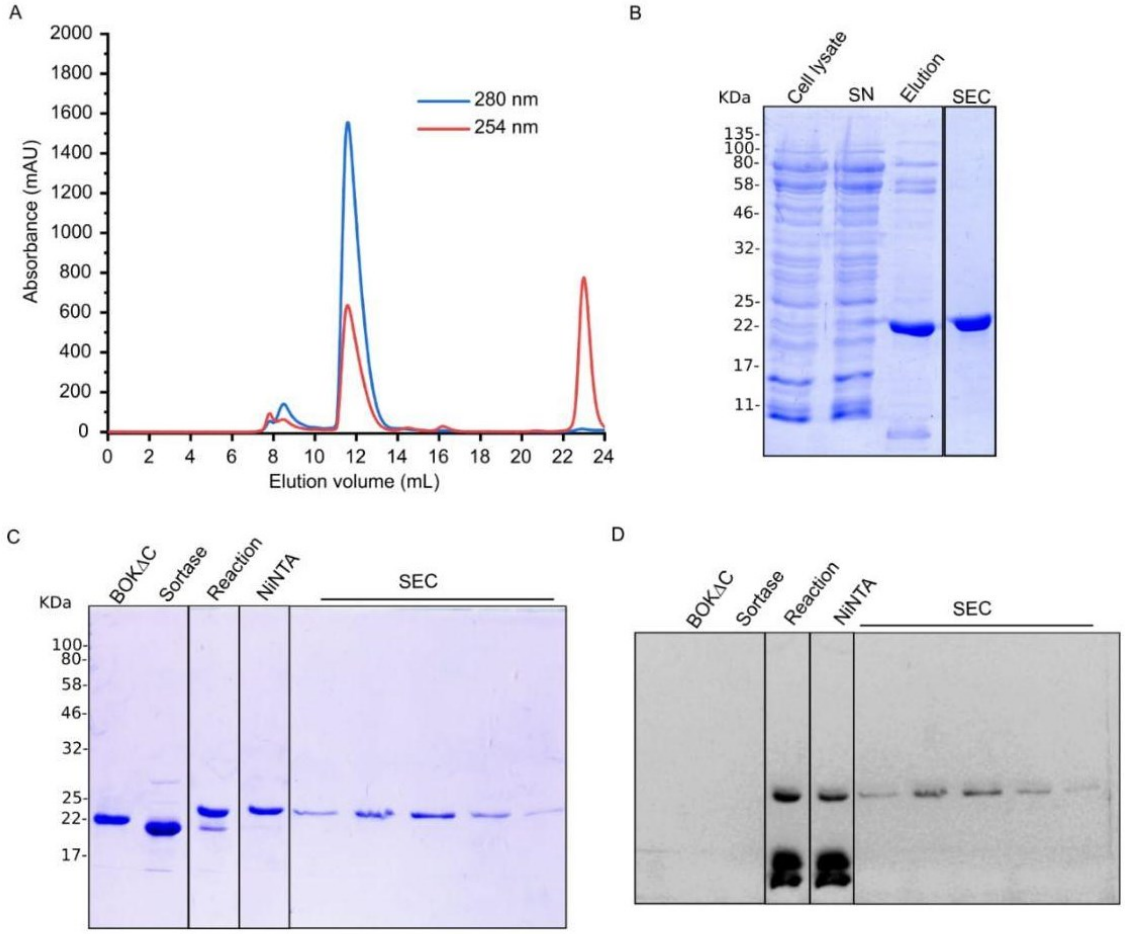

Figure S2. Purification and fluorescent labelling of recombinant 3G-BOKΔC

(A) Size-exclusion chromatogram from Superdex75 column after injection of the elution fraction of ^{3G}BOKΔC showing a dominant monomeric peak (B) Representative Coomassie-stained SDS-PAGE gel for the steps of the purification process of recombinant ^{3G}BOKΔC. SN: supernatant after lysis and centrifugation, SEC: size-exclusion chromatography (SEC fraction in the SDS-PAGE corresponds to the peak with maxima at 12 mL). (C,D): Representative SDS-PAGE gel for the steps of the fluorescent labelling of 3G-BOKΔC using an ATTO488-linked peptide and SortaseA enzyme. The same gel was Coomassie-stained (C) and visualized under UV irradiation (D). NiNTA: a fraction from the reaction mixture after incubation with NiNTA beads, SEC: size-exclusion chromatography using G25 desalting column.

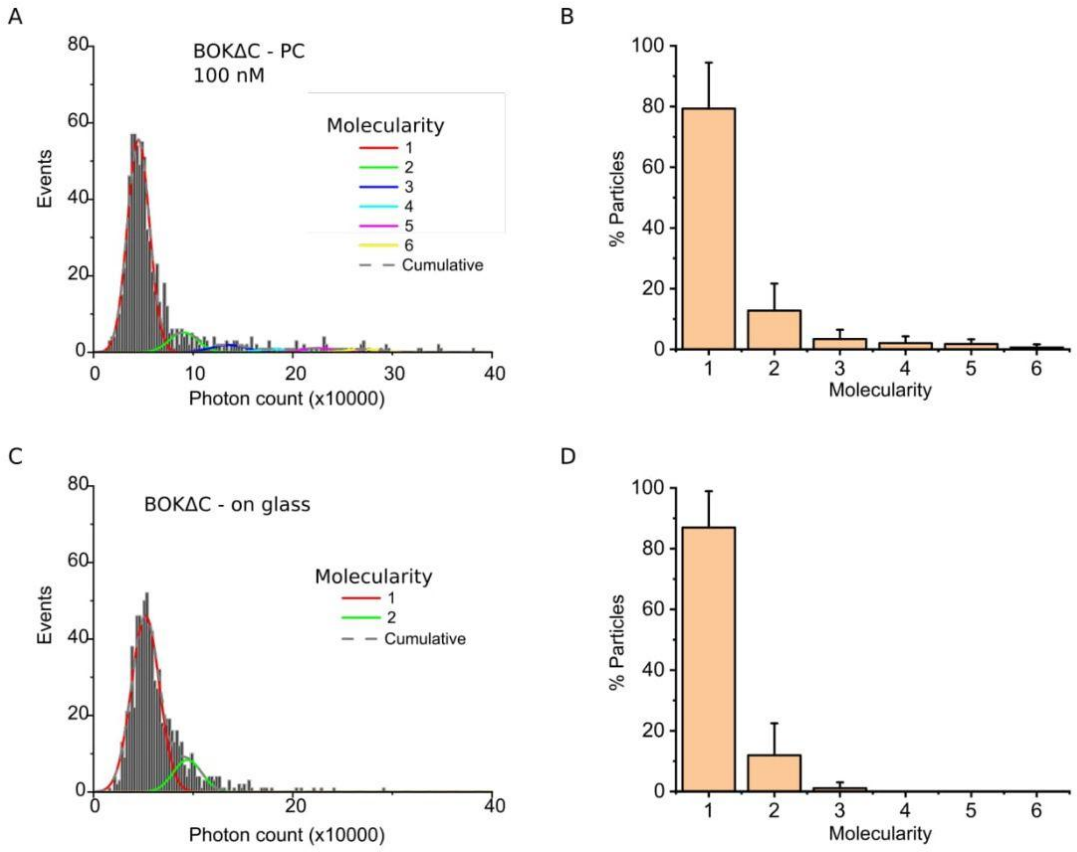

Figure S3. Characterization of BOKΔC oligomerization in SLB made from PC and on glass

(A,C) Particle fluorescence intensity distribution of BOKΔC-488 from different experiments were fitted with a linear combination of six Gaussians to estimate the abundance of different molecularities. The cumulative fit is shown as a dashed line. (B,D) The percentage of each species is derived from the area under each fitted Gaussian. The error bars correspond to the average error for each oligomeric species from three independent experiments with Particles>500 per condition per experiment.

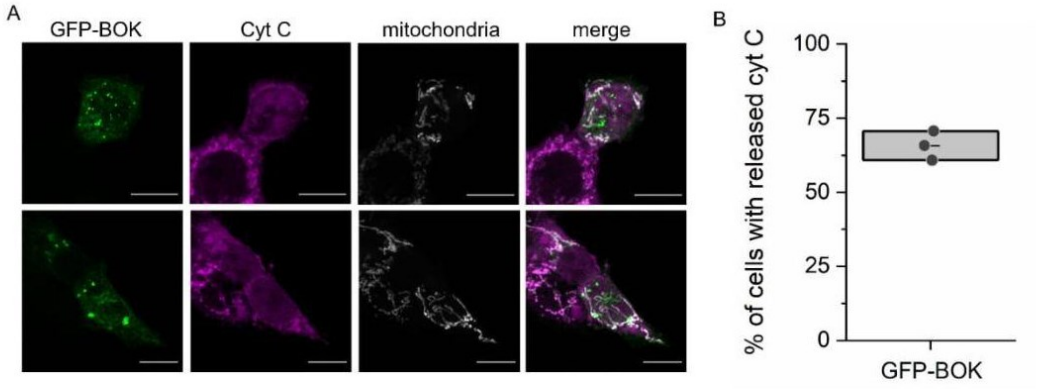

Figure S4. GFP-BOK overexpression induces cytochrome c release in HCT AKO cells.

(A) Representative confocal immunofluorescence images of subcellular localization of GFP-BOK (in green), mitochondria (grey) and cytochrome c (magenta). HCT AKO cells were transiently transfected with a GFP-BOK encoding plasmid using lipofectamine 2000 (Life Technologies) and incubated for 18–24 h. Cells were incubated with 200 nM MitoTracker 561 at 37 °C for 30 min and fixed with 3.8% paraformaldehyde in PBS. Samples were blocked with 3% bovine serum albumin (BSA)/0,1% Triton-X100 in PBS and immunoblotted with a primary anti-cyt c anti-body (1:200, BD-556432) and a secondary fluorescent anti-mouse 633 antibody (1:400, Life Technologies A-21126). Scale bars 10 µm. (B) Effect of GFP-BOK on MOMP, measured as percentage of cells showing released cyt c. Data correspond to three independent experiments, n>15 cells per condition per experiment.

Bioinformatics, 37(21), 2021, 3998–4000
doi: 10.1093/bioinformatics/btab352
Advance Access Publication Date: 8 May 2021
Applications Note

OXFORD

Bioimage informatics

DeepSinse: deep learning-based detection of single molecules

John S. H. Danial [1,2,*,†], Raed Shalaby[3,†], Katia Cosentino[4], Marwa M. Mahmoud[5], Fady Medhat[6], David Klenerman[1,2] and Ana J. Garcia Saez[3]

[1]Yusuf Hamied Department of Chemistry, University of Cambridge, Cambridge CB2 1EW, UK, [2]UK Dementia Research Institute, University of Cambridge, Cambridge CB2 0AH, UK, [3]Institute of Genetics, University of Cologne, Cologne D-50674, Germany, [4]Department of Biology, University of Osnabruck, Osnabruck 49076, Germany, [5]Department of Computer Science, University of Cambridge, Cambridge CB3 0FD, UK and [6]Department of Computer Science, University of York, York YO10 5GH, UK

*To whom correspondence should be addressed.
[†]The authors wish it to be known that, in their opinion, the first two authors should be regarded as Joint First Authors.
Associate Editor: Olga Vitek

Received on January 11, 2021; revised on April 14, 2021; editorial decision on May 3, 2021; accepted on May 6, 2021

Abstract

Motivation: Imaging single molecules has emerged as a powerful characterization tool in the biological sciences. The detection of these under various noise conditions requires the use of algorithms that are dependent on the end-user inputting several parameters, the choice of which can be challenging and subjective.
Results: In this work, we propose DeepSinse, an easily trainable and useable deep neural network that can detect single molecules with little human input and across a wide range of signal-to-noise ratios. We validate the neural network on the detection of single bursts in simulated and experimental data and compare its performance with the best-in-class, domain-specific algorithms.
Availabilityand implementation: Ground truth ROI simulating code, neural network training, validation code, classification code, ROI picker, GUI for simulating, training and validating DeepSinse as well as pre-trained networks are all released under the MIT License on www.github.com/jdanial/DeepSinse. The dSTORM dataset processing code is released under the MIT License on www.github.com/jdanial/StormProcessor.
Contact: js2494@cam.ac.uk
Supplementary information: Supplementary data are available at *Bioinformatics* online.

1 Introduction

The detection of single molecules is a fundamental step in the computational pipeline dedicated to processing single molecule microscopy data. Counting (Das et al., 2007; Ulbrich and Isacoff, 2007), distancing (Ha, 2001; Kapanidis et al., 2005), localizing (Betzig *et al.*, 2006; Heilemann et al., 2008; Hess *et al.*, 2006; Jungmann *et al.*, 2010; Rust et al., 2006) and tracking (Dahan *et al.*, 2003; Lowe *et al.*, 2010; Yildiz, 2003) single molecules require different imaging conditions and instrumentation resulting in fluorescent bursts characterized by low-to-high signal-to-noise ratios. This poses a challenge to the detection of single molecules using a universal algorithm. Segmentation of these molecules has, thus far, relied on user-chosen kernel functions, such as lowered Gaussians, Difference-of-Gaussians (DoG) or multi-order wavelets, and subjective, non-universal related parameters (Izeddin et al., 2012). All these inputs are not intuitive to the amateur user, would require careful tuning before changing the imaging conditions or modality and may fail to appropriately segment single molecules under various signal-to-noise ratios yielding unreliable performance.

Deep neural networks were recently used in calculating the background under noisy imaging conditions (Möckl et al., 2020), localizing single emitters at high spatial densities (Nehme et al., 2018, 2020) and accurately counting molecular stoichiometries by step-wise photobleaching (Xu et al., 2019). In this work, we developed and used DeepSinse, a simple, multi-layer Convolutional Neural Network (CNN) architecture to enable fast detection of single molecules using as few parameters as possible. Our neural network is composed of a CNN, a dense layer and a SoftMax (classification) layer. The neural network (Fig. 1a) was first trained to classify simulated ground-truth datasets of noise and Gaussian bursts in pre-labelled Regions Of Interest (ROIs), then validated on different, unseen, datasets of pre-labelled ROIs. We then tested it on ground-truth generated ROIs (Fig. 1b). The neural network is finally deployed by feeding an image into a peak-finding algorithm based on identifying regional maxima.

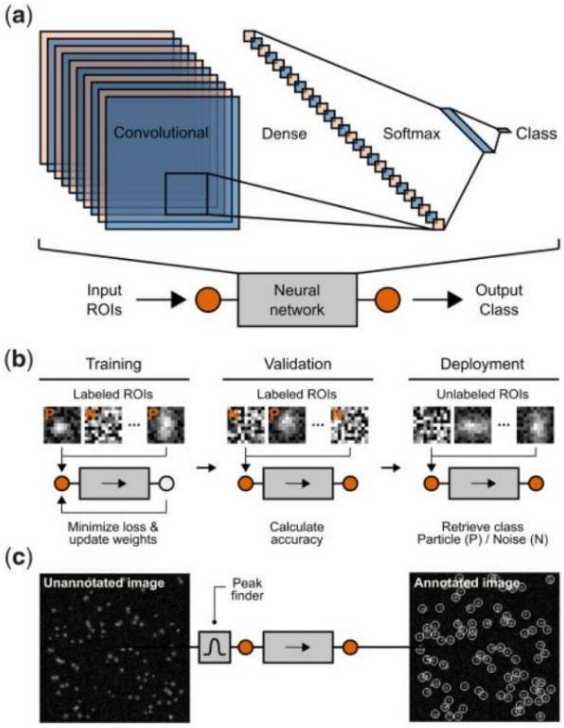

Fig. 1. Single molecule segmentation pipeline using DeepSinse. (**a**) Architecture of the neural network used in segmenting single molecule bursts from noise. The CNN layer is connected to a dense (i.e. fully connected) layer. The dense layer is connected to a SoftMax for normalization which, in turn, is connected to a classification layer. Number of trainable parameters is 21 802. (**b**) The neural network is first GPU-trained on ground-truth, pre-labelled (i.e. annotated) ROIs divided into two classes; particle (P) or Noise (N). The ROIs are fed-forward into the network and a loss function is evaluated every mini-batch of 10 ROIs. Following training on a complete dataset, the network is validated on unseen data and the classification accuracy is calculated based on the correspondence between the generated and network-output classes. The network is finally tested on the CPU or GPU on unlabelled ROIs and the class for each ROI is extracted. (**c**) The network is, finally, deployed by feeding an image into a peak-finding algorithm which identifies regional maxima based on their eight nearest neighbours' connectivity. The algorithm locates several hundred ROIs containing noise and particles and the ROIs are fed into the neural network which eventually segments the particles producing an annotated image

The peak-finding algorithm outputs hundreds of noise- and burst- containing ROIs which are then fed into the trained network for classification, thus, resulting in an annotated image (Fig. 1c).

2 Materials and methods

To construct the training dataset, 100 particles (bursts) were randomly scattered across images which are 200 by 200 pixels in size. The standard deviation of each burst was sampled using a random number generator confined between one and two pixels to simulate small and large particles. Each burst was convoluted with a 2D Gaussian Kernel. The produced images in counts I_c was modified as follows:

$$I_e = I_c * QE + DC + RO$$

where I_e is the image signal in electrons, QE is the quantum efficiency, DC is the dark current and RO is the read out noise. The quantum efficiency was set at 95%, dark current was set at 0.0002 electrons/second and read out noise was set to 1 electron. These values are typical of commercially available Electron-Multiplying Charge Coupled Detectors (EMCCDs). To simulate noise, I_e was modified as follows:

$$I_e = gamma\left(I_e, G - 1 + \frac{1}{I_e}\right) + O$$

where G is the camera gain (corrected for conversion factor) and O is the camera bias offset. The gain was set to 58.8 and offset to 400. This noise model was chosen to best replicate the electron-multiplication feature in emCCDs (Hirsch et al., 2013). Burst-containing, and pure-noise, images were simulated with the formers' peak burst intensities varying from 50 to 100 counts corresponding to signal-to-noise ratios from 24.85 to 45.81 and 100 images were simulated with pure noise. Pre-annotated ROIs were picked from each of these images, intensity scaled between 0 and 1 to ensure the user avoids subjective segmentation parameters such as the intensity threshold, shuffled and fed into the neural network for training. To optimize performance, the neural network was trained using different ROI radii (Fig. 2a) and number of ROIs (Fig. 2b). The lowest FNR (61.45%) and FPR (0.3%) were achieved at a ROI radius of 5 pixels and 10 000 training ROIs.

3 Results

To study the performance of DeepSinse at varying SNRs, we first simulated 100 burst-containing images with peak burst intensities varying from 1 to 100 counts corresponding to signal-to-noise ratios from 2.17 to 45.81. At the lowest simulated SNR of 2.17 (where the particles are visually undiscernible), the FNR is 91.1% and FPR is 0%. At the highest simulated SNR of 45.81, the FNR is 0% and FPR is 0.1% (Fig. 2c and e). We then tested the performance of DeepSinse with experimentally obtained images of fluorescent beads (see Supplementary Information). At the lowest acquired mean SNR of 2.88, the measured FNR is 76.5% and FPR is 0.01%, whilst at the highest acquired mean SNR of 4.5, the measured FNR is 13.76% and FPR is 1.25% (Fig. 2d and f). We compare these metrics with the best in-class, domain-specific algorithm used for the detection of single molecules which is based on image wavelet segmentation (Izeddin *et al.*, 2012). Wavelet analysis achieves a FNR of 75% and FPR of 2% at an SNR of 2.6. These figures are worse than those measured with DeepSinse, namely, a FNR of 15.5% (5× improvement) and FPR of 0.5% (4× improvement) and show the prominence of DeepSinse in detecting single molecules under extreme noise conditions and low SNRs reaching 2.17.

To ensure applicability on a real biological sample acquired at the single molecule level, we used an exemplary dataset of a U2OS cell expressing the GFP-tagged nucleoporin component (Nup96) of the nuclear pore complex labelled with Alexa647-tagged-Anti-GFP nanobody and imaged using dSTORM (Thevathasan et al., 2019) (see Data availability). Molecules detected in single molecule localization microscopy are subjected to strict filtering to ensure the localization precision is minimized (see Supplementary Information). We assessed the performance of DeepSinse and wavelet filtering by comparing the number of detected particles pre filtering (Fig. 3a) and the fraction of rejected particles post filtering (Fig. 3b) in 1000 frames. DeepSinse outperformed

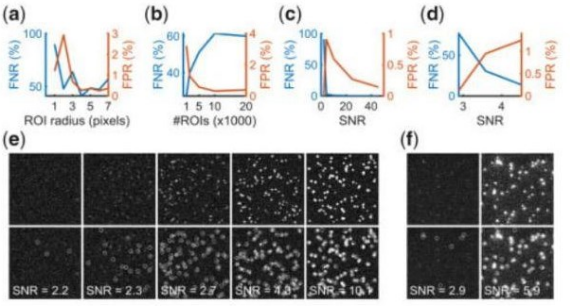

Fig. 2. Systematic analysis of the performance of the neural network for parameter-tuning and validation purposes. Measurement of the FNR and FPR against (**a**) the radius of ROIs and (**b**) number of ROIs. (**c**) SNR of simulated ROIs and (**d**) SNR of experimentally obtained ROIs. Exemplary (**e**) simulated and (**f**) experimentally obtained images of particles at different SNRs

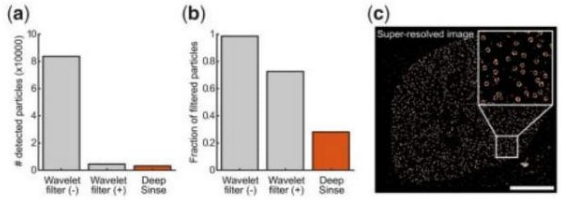

Fig. 3. Comparison of the performance of a wavelet filter with DeepSinse for blinking particles obtained from a publicly available exemplary dataset (see Data availability). (**a**) Number of detected particles and (**b**) fraction of rejected particles obtained using a wavelet filter and peak intensity threshold set to 0 photons [Wavelet filter (-)], wavelet filter and peak intensity threshold set to standard deviation of the first wavelet level [Wavelet filter (+)] and DeepSinse for 1000 frames of the entire dataset. (**c**) Super-resolved image of the exemplary dataset produced following detection of particles using DeepSinse and subsequent filtering

wavelet filtering, detecting 31 331 particles (8810 of which were filtered corresponding to 28%) compared to 45 131 for wavelet filtering with a peak intensity threshold applied (32 747 of which were filtered corresponding to 73%) and 837 129 without a peak intensity threshold applied (32 747 of which were filtered corresponding to 99%). We, subsequently, used DeepSinse to classify all ROIs extracted from 90 000 of the dataset and processed them in a similar fashion to that reported in Thevathasan *et al.* (2019) to produce a super-resolved image where the ring-like structure of the nucleoporin assembly organized into an oligomer of 8-mer configuration was clearly resolvable as per the original account (Fig. 3c).

There are two important factors characterizing the performance of DeepSinse: accuracy and speed. In the above, we provided an extensive comparison of the accuracy achieved by DeepSinse in detecting single molecules, even at extremely low SNRs across simulated and experimental data. Since the performance of DeepSinse is dependent on the simulated data resembling the experimental data, we expect the performance to be further improved if the training data is extracted from experimentally obtained images. For this reason, we have included a ROI-picker which the end user can utilize in selecting ROIs from experimental data to train the neural network (see Data availability). In terms of speed, DeepSinse can be trained using 10 000 ROIs on a mid-class Graphical Processing Unit (GPU) NVIDIA GeForce GTX 1650 for 12 s or an Intel Core i7-9750H CPU running at 2.60 GHz for 11 s. DeepSinse can be deployed in 40 s, for 1000 frames which are 200 by 200 pixels in size, using the named GPU or 1 min and 20 s on the named CPU. By comparison, Wavelet filtering with, and without, the application of a peak intensity threshold takes 9 min, and 10 s, respectively.

DeepSinse presents a novel paradigm in the detection of single molecules. The versatility, high selectivity, dependence on modest resources and speed in training and testing of the proposed neural network, as discussed above, are strong warrants for its adoption in all single molecule microscopy data processing pipelines. Importantly, our simple network does not depend on the application of any subjective peak intensity threshold and is capable of detecting single molecules under extreme noise conditions; therefore, pushing detection limits with current instrumentation to new heights. Our proposed network can be augmented with other, previously developed neural networks to migrate to smart and fully automated analysis pipelines for single molecule microscopy data. To facilitate this, we have built an easy-to-use Graphical User Interface (GUI) for generating simulated data, training the neural network and accessing the performance of the trained network. Furthermore, we made available a number of pre-trained networks at different camera gain values which can be integrated in any MATLAB© based code.

Data availability

Except for the exemplary nucleoporin dataset which is publicly available on the BioImage Archive (https://www.ebi.ac.uk/biostudies/files/S-BIAD8/Library/GFP/AB/raw/GFP_AB-AF647_190528_8.zip), ground-truth generated data and experimentally obtained data used for testing and validating the neural network are available as Supplementary Data.

Author contributions

J.S.H.D. conceived the project, R.S. performed the experiments, J.S.H.D., M.M.M. and F.M. developed the computational pipeline, R.S., K.C. and J.S.H.D. tested and validated the code, D.K. and A.J.G.S. provided experimental infrastructure and J.S.H.D. wrote manuscript with input from all authors.

Funding

J.S.H.D. was partially funded by a College Research Associateship (King's College, Cambridge) and a research from fellowship from EISAI and the UK Dementia Research Institute. K.C. acknowledges the Elite programme for Postdocs of the Baden-Wurttemberg Stiftung for financial support. M.M.M. was funded by a Junior Research Fellowship (King's College, Cambridge), D.K. was funded by an ERC advanced grant [669237]. A.J.G.S. and R.S. are funded by an ERC consolidator grant (APOSITE).

Conflict of Interest: none declared.

References

Betzig,E. *et al.* (2006) Imaging intracellular fluorescent proteins at nanometer resolution. *Science*, **313**, 1642–1645.

Dahan,M. *et al.* (2003) Diffusion dynamics of glycine receptors revealed by single-quantum dot tracking. *Science*, **302**, 442–445.

Das,S.K. *et al.* (2007) Membrane protein stoichiometry determined from the step-wise photobleaching of dye-labelled subunits. *ChemBioChem*, **8**, 994–999.

Ha,T. (2001) Single-molecule fluorescence resonance energy transfer. *Methods*, **25**, 78–86.

Heilemann,M. *et al.* (2008) Subdiffraction-resolution fluorescence imaging with conventional fluorescent probes. *Angew. Chem. Int. Ed.*, **47**, 6172–6176.

Hess,S.T. *et al.* (2006) Ultra-high resolution imaging by fluorescence photoactivation localization microscopy. *Biophys. J.*, **91**, 4258–4272.

Hirsch,M. *et al.* (2013) A stochastic model for electron multiplication charge-coupled devices – from theory to practice. *PLoS One*, **8**, e53671.

Izeddin,I. *et al.* (2012) Wavelet analysis for single molecule localization microscopy. *Opt. Express*, **20**, 2081–2095.

Jungmann,R. *et al.* (2010) Single-molecule kinetics and super-resolution microscopy by fluorescence imaging of transient binding on DNA origami. *Nano Lett.*, **10**, 4756–4761.

Kapanidis,A.N. *et al.* (2005) Alternating-laser excitation of single molecules. *Acc. Chem. Res.*, **38**, 523–533.

Lowe,A.R. *et al.* (2010) Selectivity mechanism of the nuclear pore complex characterized by single cargo tracking. *Nature*, **467**, 600–603.

Möckl,L. *et al.* (2020) Accurate and rapid background estimation in single-molecule localization microscopy using the deep neural network BGnet. *Proc. Natl. Acad. Sci. USA*, **117**, 60–67.

Nehme,E. *et al.* (2018) Deep-STORM: super-resolution single-molecule microscopy by deep learning. *Optica*, **5**, 458–464.

Nehme,E. *et al.* (2020) DeepSTORM3D: dense 3D localization microscopy and PSF design by deep learning. *Nat. Methods*, **17**, 734–740.

Rust,M.J. *et al.* (2006) Sub-diffraction-limit imaging by stochastic optical reconstruction microscopy (STORM). *Nat. Methods*, **3**, 793–796.

Thevathasan,J.V. *et al.* (2019) Nuclear pores as versatile reference standards for quantitative superresolution microscopy. *Nat. Methods*, **16**, 1045–1053.

Ulbrich,M.H. and Isacoff,E.Y. (2007) Subunit counting in membrane-bound proteins. *Nat. Methods*, **4**, 319–321.

Xu,J. *et al.* (2019) Automated stoichiometry analysis of single-molecule fluorescence imaging traces via deep learning. *J. Am. Chem. Soc.*, **141**, 6976–6985.

Yildiz,A. (2003) Myosin V walks hand-over-hand: single fluorophore imaging with 1.5-nm localization. *Science*, **300**, 2061–2065.

THE JOURNAL OF PHYSICAL CHEMISTRY LETTERS
A JOURNAL OF THE AMERICAN CHEMICAL SOCIETY

pubs.acs.org/JPCL Letter

Systematic Assessment of the Accuracy of Subunit Counting in Biomolecular Complexes Using Automated Single-Molecule Brightness Analysis

John S. H. Danial,* Yuri Quintana, Uris Ros, Raed Shalaby, Eleonora G. Margheritis, Sabrina Chumpen Ramirez, Christian Ungermann, Ana J. Garcia-Saez,* and Katia Cosentino*

Cite This: J. Phys. Chem. Lett. 2022, 13, 822−829 Read Online

ACCESS | Metrics & More | Article Recommendations | Supporting Information

ABSTRACT: Analysis of single-molecule brightness allows subunit counting of high-order oligomeric biomolecular complexes. Although the theory behind the method has been extensively assessed, systematic analysis of the experimental conditions required to accurately quantify the stoichiometry of biological complexes remains challenging. In this work, we develop a high-throughput, automated computational pipeline for single-molecule brightness analysis that requires minimal human input. We use this strategy to systematically quantify the accuracy of counting under a wide range of experimental conditions in simulated ground-truth data and then validate its use on experimentally obtained data. Our approach defines a set of conditions under which subunit counting by brightness analysis is designed to work optimally and helps in establishing the experimental limits in quantifying the number of subunits in a complex of interest. Finally, we combine these features into a powerful, yet simple, software that can be easily used for the analysis of the stoichiometry of such complexes.

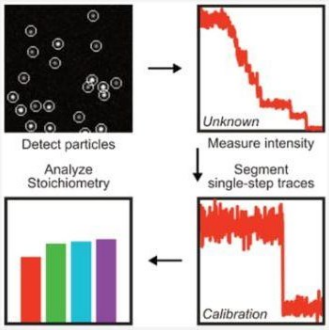

Assembly into nanoscopic oligomeric complexes is a common mechanism that allows biomolecules to perform their cellular activities.[1−3] Determining the structural organization of these complexes is paramount to understanding their functions. High-resolution structural characterization methods, such as X-ray diffraction or cryo-electron microscopy, provide angstrom-resolution atomic maps but require the biological complex under study to be purifiable with a high yield, to be preserved in its entirety along with, possibly, its native physiological environment during the purification step, and to be stoichiometrically homologous. Super-resolution microscopy methods can chart the architecture of many of these nanoscopic complexes directly inside their cellular environments with nanometer resolution;[4−7] however, precise molecular counting using super-resolution microscopies is a formidable task that remains challenging.[5,8−12]

Single-molecule fluorescence analysis has emerged as a powerful strategy for measuring the stoichiometry of small and large biomolecular complexes.[13−20] Two major approaches comprising subunit counting by this analytical toolkit are known as stepwise photobleaching[21] and single-molecule brightness analysis.[22] In stepwise photobleaching analysis, the number of photobleaching steps exhibited by a single oligomer is counted and correlated with the number of subunits contained within. Counting the number of photobleaching steps has, traditionally, been performed manually or by the use of some algorithms.[23] However, both approaches require trained users that are able to isolate actual photobleaching steps from artifacts derived from high noise levels, the presence of one or several photo-blinking steps, and temporal variations in the intensity of the excitation source. These problems were recently addressed by training and deploying convolutional and long−short-term memory deep learning neural network (CLDNN) to classify different oligomeric species on the basis of the number of photobleaching steps they exhibit.[24] Despite the high accuracy of this network in discerning oligomers with up to five subunits, automated and manual classification based on step counting remains extremely challenging for larger assemblies.

Single-molecule brightness analysis is not limited by the mentioned factors and has the potential to quantify the stoichiometry of small to medium-sized macromolecular complexes.[22] In this method, the number of underlying subunits of an oligomeric species is obtained by comparing its brightness to a calibration curve theoretically calculated from the measured average brightness of monomers. Monomers, selected on the basis of the stepwise photobleaching analysis, can be obtained by different strategies: from a sample with a mixture of different oligomers, from partial bleaching of protein complexes,[15] or from non-activated or

Received: November 22, 2021
Accepted: December 10, 2021
Published: January 19, 2022

https://doi.org/10.1021/acs.jpclett.1c03835
J. Phys. Chem. Lett. 2022, 13, 822−829

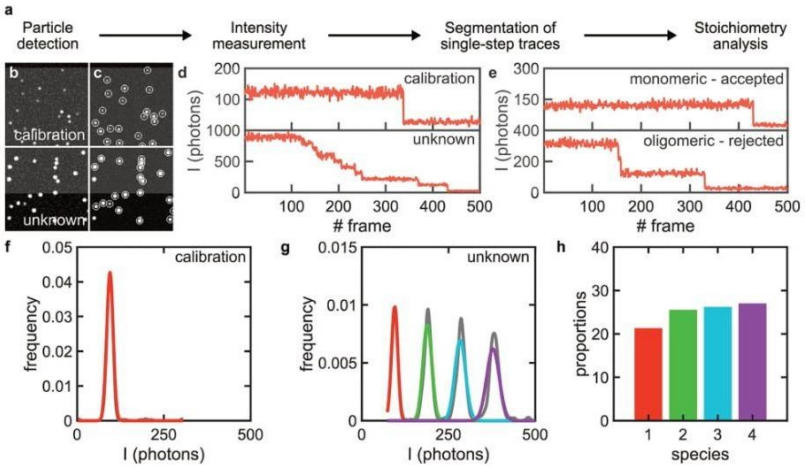

Figure 1. Overview of the mode of operation of SAS. (a) SAS workflow. (b,c) Exemplary simulated, ground-truth images of single molecules for a set of calibration (stoichiometry: 50% monomers, 25% dimers, and 25% trimers) and unknown (stoichiometry: equal proportions of monomers to 16-mer) species (b) before detection and (c) after detection where detected particles are encircled with white circles. (d) Exemplary intensity traces of two randomly chosen particles from the calibration and unknown data sets after conversion from signal counts to photons. (e) Examples of monomeric and oligomeric traces extracted from the calibration data set that are automatically annotated by SAS. (f) Kernel density function of the intensity distribution underlying the calibration data set (gray) and the Gaussian curve representing the monomeric population (red). (g) Kernel density function of the intensity distribution underlying the unknown data set (gray) and the Gaussian mixture representing the monomeric population (red, green, cyan, and purple). (h) Bar graph of the proportion of the species underlying the unknown data set (color code as in panel g).

mutant forms of the protein of interest, which are unable to oligomerize.[17] Paramount to the accurate quantification of stoichiometry is the selection of "clean" intensity traces of the monomeric species, which are not affected by any intensity variations other than imaging noise. Equally important is the accurate measurement of the brightness of oligomeric species, which is irrespective of high noise, early photobleaching, the presence of multiple photoblinking steps, and other non-specific intensity variations.

Despite the enormous power of single-molecule brightness analysis and the unique niche it occupies within the family of methods used to quantity absolute molecular copy numbers, it suffers from a number of important limitations.

(1) The fluorescence intensity of the monomeric and oligomeric particles may take a wide range of values. Detecting these particles with high fidelity (i.e., low false negative and positive rates) requires subjective changes of the detection parameters by the end user. This process hampers the automation of data processing and the accuracy of the eventual subunit counting.

(2) The maximum number of resolved oligomers is strictly connected to the quality of the monomer calibration. Therefore, the selection of clean, single-step intensity traces for monomer calibration is paramount for resolving higher-order oligomers; however, traditionally this step is performed manually. In addition to the potential introduction of human error during the classification process, this is a complicated task due to the need for tens to hundreds of such traces for appropriate calibration, which needs to be repeated for each data set due to any subtle change in the experimental setup or in the sample preparation.

(3) Although the theory behind single-molecule brightness analysis has been extensively scrutinized, the experimental conditions under which this method is designed to operate optimally have never been systematically navigated. This prevented the optimized application of this method and in some cases may have led to incorrect conclusions about the underlying biological system.

(4) The accuracy of this method in quantifying multiple stoichiometric occurrences (e.g., dimeric, trimeric, tetrameric, etc.) of protein complexes, as well as any change in the proportion of oligomeric species as a function of protein concentration, was not systematically assessed before. This prevented the end users from understanding the analytical limits of this approach and judging its applicability to the system of their interest.

(5) Fitting the intensity distributions to multiple Gaussians may not perfectly match the real data introducing false stoichiometry assessments.

To address these important limitations, we have developed SAS (Stoichiometry Analysis Software), a fully automated software pipeline for analyzing the stoichiometry of oligomeric complexes imaged by fluorescence microscopy. By employing SAS to quantify the number of complex subunits by brightness analysis, we could carefully assess the accuracy of this method and provide the users with guidelines for the optimal experimental and analytical conditions to employ for reliable and accurate stoichiometry measurements of protein complexes.

SAS uses a simple, but robust, parameter-free, single-molecule particle detection algorithm based on a multilayer convolutional neural network (DeepSinse), which was previously found to exhibit 4−5 times lower false positive and negative rates compared to the best-in-class, domain specific detection algorithm based on wavelet filtering on a remarkably wide range of signal-to-noise ratios (SNRs).[25] Importantly, SAS requires no human input for optimized detection (Figure 1a−c and Figure S1; see Methods). The

https://doi.org/10.1021/acs.jpclett.1c03835
J. Phys. Chem. Lett. 2022, 13, 822−829

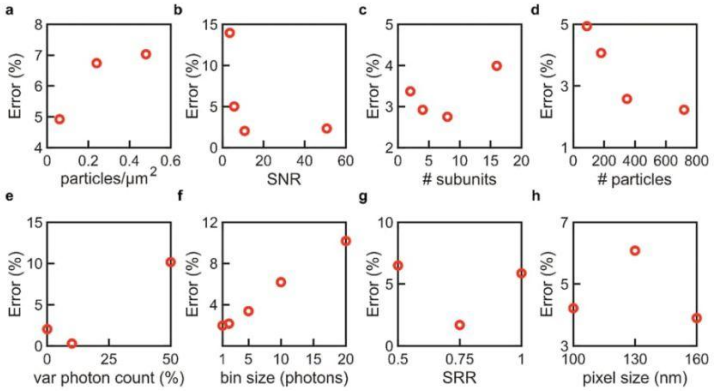

Figure 2. Assessment of the accuracy of subunit counting under different simulated experimental conditions. Measurement of the error against the (a) density of particles, (b) signal-to-noise ratio (SNR), (c) maximum number of subunits per complex, (d) number of monomeric particles selected for calibration, (e) intercomplex variation in photon count, (f) kernel probability distribution function (pdf) bin size, (g) ratio of the σ, or standard deviation, of the point spread function (PSF) of the underlying particles to ROI radius (SRR), and (h) pixel size. Base parameters used across all simulations (except for those varied): number of time frames, 500; number of movies for calibration and unknown species (each), at least 10; maximum photon count, 10; intercomplex variation in photon count, 0%; σ of the PSF of each complex, 130 nm; stoichiometry of the calibration species , 50% monomers, 25% dimers, and 25% trimers; stoichiometry of the unknown species, 50% monomers and 50% dimers. See the supplementary data for camera parameters.

time-dependent intensity traces of the detected molecules are extracted from the acquired frame stacks by measuring the background-corrected intensities in regions of interest (ROIs) centered around the centroids of each detected particle (Figure 1c,d; see Methods). In SAS, data to be processed need to be classified as either "calibration" or "unknown" (Figure 1b–d). The "calibration" data set will be used to find the brightness values of monomeric species. For this purpose, we fed the extracted intensity traces into a trace annotator that selects clean, single-step traces by calculating and normalizing the gradient (i.e., slope) of each trace and picking up traces with a single peak gradient above a preset threshold (Figure 1e and Figure S2; see Methods). The selected traces are then used to construct a distribution curve from a kernel density function and fitting it to a Gaussian mixture model (GMM) to account for the fact that some of the selected single-step traces are not monomeric due to the photobleaching of two, or more, fluorophores at the same time within the same complex (Figure 1f; see Methods). The mean and standard deviation of the intensity values in the fitted Gaussian curve corresponding to the monomeric population are, subsequently, used to construct an idealized Gaussian mixture that represents the distribution of the higher-order oligomeric species. By overimposing these multiple Gaussians on the intensity distribution of all detected particles from the "unknown" data set, we calculate the proportion of each species from the area of each Gaussian curve (Figure 1g; see Methods). Finally, the calculated proportions are corrected for incomplete labeling using a binomial probability density function to yield the true stoichiometry of the underlying biological complex (Figure 1h; see Methods). The quality of the monomeric calibration Gaussian curve is critical in the brightness analysis approach as the width of the intensity distribution defines the maximum number of species that can be resolved. The selection of monomeric traces by SAS is reliable even for wide and complex simulated and experimental intensity distributions (see, for example, the calibration distribution of experimental data in Figure S3). However, this step needs particular attention and scrutiny by the final end user.

We then assessed the performance of the software and the accuracy of counting using single-molecule brightness analysis by simulating ground-truth data under a wide range of experimental conditions (see Methods). To this end, we evaluated the error in the calculated versus simulated proportions of species when varying the density of particles, SNR, number of subunits per complex (at a constant particle density), number of monomeric particles selected for calibration, variation in the intensity of each molecule, the bin size of the kernel probability distribution function (pdf), the particle intensity distribution width (i.e., σ) to ROI radius (SRR) from which the intensity traces are extracted, and the pixel size (Figure 2a–h). Under all simulated conditions, the error in the assignment of oligomeric species did not exceed 15% while reaching, in many cases, <5%. Variations in the density of particles, number of subunits per complex, and pixel size did not result in substantial changes to the error (<3%) within the simulated ranges.

Our analysis shows that the bin size for generating a kernel pdf, as well as the number of calibration particles, may be a critical parameter to consider for fitting the intensity distributions, as increasing the bin size further increases the error rate while decreasing the number of calibration particles decreases the error rate. SAS employs a bin size of five photons, which provides an error of 3%, to ensure that the intensity information is not lost and the fitting procedure is not oversensitive to fine fluctuations in the intensity curve.

Expectedly, decreasing the SNR to 3.54, which is remarkably low for single-molecule experiments, affects the fidelity of the stoichiometry measurements, resulting in an error of 13.96%. A marginal improvement of the SNR to 5.68 yields a large improvement in the error (=5.01%). Any improvement to the SNR beyond 5–10 yields diminishing returns on the error (>2%). This result indicates that while the use of bright fluorophores and efficient detection setups is necessary to improve the detection efficiency, beyond a certain point, it is

https://doi.org/10.1021/acs.jpclett.1c03835
J. Phys. Chem. Lett. 2022, 13, 822–829

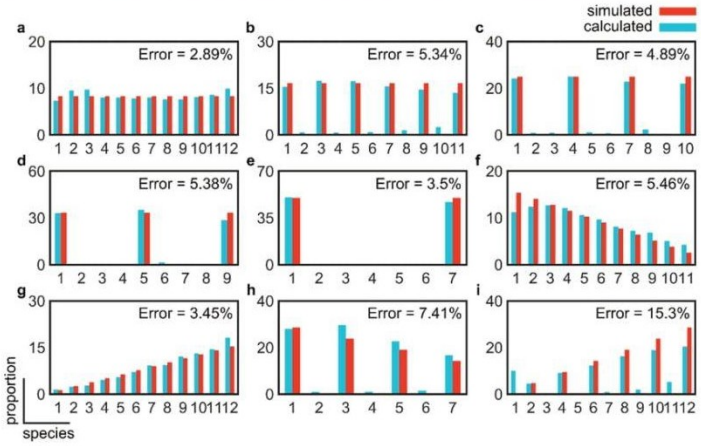

Figure 3. Assessment of the accuracy of subunit counting under different simulated stoichiometric configurations. Starting from a monomer as the basic unit, we assessed the measurement of the error for equal proportions (8.33%) of (a) monomeric species, (b) dimeric species, (c) trimeric species, (d) tetrameric species, (e) hexameric species, (f) decreasing proportions (15.4% monomers, 14.1% dimers, 12.8% trimers, 11.5% tetramers, 10.3% pentamers, 9.0% hexamers, 7.7% heptamers, 6.4% octamers, 5.1% 9-mers, 3.8% 10-mers, 2.6% 11-mers, and 1.3% 12-mers) based on monomeric units, (g) increasing proportions (same as panel f but in reverse order) based on monomeric units, (h) decreasing proportions (28.6% monomers, 23.9% trimers, 19.0% pentamers, 14.3% heptamers, 9.5% 9-mers, and 4.8% 11-mers) based on the addition of dimeric units, and (i) increasing proportions (same as panel h but in reverse order) based on the addition of dimeric units.

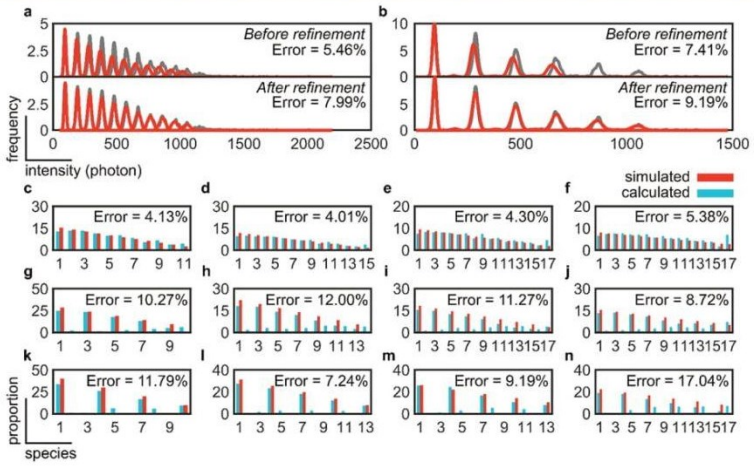

Figure 4. Assessment of the accuracy of subunit counting under real experimental conditions and challenging stoichiometric configurations. Kernel density distribution functions and error measurements for 12-mer stoichiometries based on the addition of (a) monomeric or (b) dimeric units before and after refinement simulated at an SNR of 10.74 (photon count of 10) and intercomplex variation in photon count of 0%. Kernel density distributions are colored gray, and the Gaussian mixture is colored red. Error measurements based on the addition of (c–f) monomeric, (g–j) dimeric, or (k–n) trimeric units of high-order oligomers: (c, g, and k) 12-mer, (d, h, and l) 16-mer, (e, i, and m) 20-mer, and (f, j, and n) 24-mer. Simulations were performed at an SNR of 5.68 (photon count of 5) and an intercomplex variation in photon count of 20%. Proportions of each species can be found in the supplementary data.

not necessarily correlated with improved counting accuracy by SAS. In contrast, our simulations indicate that intensity variation is a critical parameter to the accuracy of counting. Intensity variations of >25% can yield error values of >5%. These results favor the use of stable fluorophores that exhibit a narrow emission spectrum and minimal photoblinking, as well as flat-field illumination schemes that minimize spatial variations in the excitation profile and unpolarized light as the excitation source to ensure fluorophores under different orientations are equally excited.

Finally, the SRR affects the accuracy of counting. Surprisingly, however, our simulations indicate an optimal ratio of 0.75 at which the error is minimized to 1.69%. One possible explanation for this important finding is that for ROIs smaller than the full width of the particles the extracted intensities are inaccurate given that a large portion of the point spread function (PSF) lies outside of the borders of the ROIs, yet for ROIs much larger than the full width of the particles, noise affects the extracted intensities. Our simulations point to the importance of accurately measuring the mean standard

https://doi.org/10.1021/acs.jpclett.1c03835
J. Phys. Chem. Lett. 2022, 13, 822–829

deviation of the underlying particles in choosing the ROI radius.

Then, we assessed the accuracy of subunit counting for different stoichiometric configurations (Figure 3a–i). To do this, we simulated nine different stoichiometric configurations with a maximum of 12 subunits where the proportion of species is constant (Figure 3a–e), decreasing (Figure 3f,h), or increasing (Figure 3g,i) with the number of subunits. The underlying species were also allowed to take monomeric up to hexameric units. Under all simulated configurations, the error did not exceed 15%. The accuracy of counting was particularly minimized when the proportion of species was held constant under all stoichiometries (Figure 3a–e). Although the error of the measurements was excellent throughout, we have noticed that, particularly where we have simulated increasing or decreasing proportions, a large fraction of the species was not recognized. This finding suggested that in a typical experiment, where not all single molecules assemble into higher-order oligomers and where these oligomers add dimeric or higher-order units, larger complexes might not be recognized in the analysis.

To investigate the reason behind the poorer performance of the software in quantifying the number of subunits in the mentioned stoichiometric configurations, we paid closer attention to the fittings of the idealized Gaussian mixture to the kernel density function of the unknown species. We found that marginal shifts in the mean intensity values of the calibration curves would propagate to high-order oligomers beyond 8–10 subunits causing obvious misfits to the idealized mixture of Gaussians as suggested in Figure 1g. Furthermore, this issue could be more severe in a real, experimental setting where the intensity distribution of the underlying species might not follow the idealized Gaussian mixture due to imaging artifacts or photoquenching.

To solve this issue, we implemented a fitting refinement step in which the mean intensity value of the calibration curve is scanned in a ±10 photons region, with one-photon resolution, and the residual error is calculated after fitting with the Gaussian mixture model. The refined mean intensity value of the calibration curve is chosen where the residual error is minimum. Given that the mean intensity value of the monomer species is changed, we expect that the error would increase (i.e., be worsened) at the expense of recovering a larger number of species. Following this improvement, we first assessed two challenging configurations (Figure 3f,h). As expected, our assessments reveal an increase in the error from 5.46% to 7.99%, for the configuration based on the addition of monomers, and from 7.41% to 9.19%, for the configuration based on the addition of dimers (Figure 4a,b). The advantages of using a refinement step were particularly observed in this last configuration where the number of recognized species increased from 7 to 11 out of a simulated 12 (Figure 4b). In all of the above, the SNR was set to 10.74 and the intercomplex variation in photon count was set to 0% to ensure that none of these important photophysical parameters would complicate or affect our assessment of the accuracy of counting.

Next, we conducted a final round of assessment to establish the absolute limits of accurate counting with single-molecule brightness analysis using the introduced refinement step for more challenging experimental conditions (i.e., an SNR of 5.68 and an intercomplex variation in photon count of 20%) and stoichiometric configurations (from 12- to 24-mers with a decreasing proportion of species) (Figure 4c–n). On average, the error was lowest for the configurations based on monomeric, followed by dimeric, and finally trimeric units. All error measurements were <15% except for the 24-mer in trimeric configuration, where the measured error was 17.04%. Finally, and because of the refinement step, high-order species were recognized in all cases; however, low proportions of species that were not simulated in the configurations based on the addition of dimeric and trimeric units were also produced.

Importantly, the end user needs to be aware that the refinement step helps to increase the accuracy at the expense of sensitivity. This step can be included in or excluded from the analysis, as illustrated in the GUI (Figure S1), thus leaving to the end user the choice between accuracy or sensitivity, according to the specific experimental and analytical need.

In summary, this extensive analysis has shown the following.

(1) The SNR and intercomplex variation in photon count play an important role in dictating the accuracy as well as the number of recognized species within a complex of interest. While marginal improvements in the SNR yield noticeable improvements to the accuracy of counting quickly followed by diminishing returns, the intercomplex variation in photon count has to be minimized at all times to maximize the accuracy of counting and number of recognized species.

(2) The ROI size has to be optimized manually by the user in case the mean standard deviation in the PSF of the imaged complexes is known.

(3) The stoichiometric occurrence does not affect the accuracy of measurements, but relevant factors are the basic unit (i.e., monomeric, dimeric, or trimeric) and whether the proportion of species increases or decreases with the number of subunits.

(4) Refining the mean intensity value of the calibration species can recover high-order species, but at the expense of a reduced counting sensitivity as well as uncovering additional species that are absent in reality. The use of the refinement step is dependent on whether the user is interested in accurate or more comprehensive measurements of stoichiometry.

Having extensively assessed the accuracy of counting with single-molecule brightness analysis, we, finally, validated SAS on biological samples whose stoichiometry is known *a priori*, as reported from either structural studies or prior subunit counting measurements performed manually. In addition, the chosen samples had to satisfy the following requirements: (1) The labeling efficiency had to be previously reported to ensure that any unlabeled species are accurately accounted for. Furthermore, the labeling efficiency had to be reported under exactly the same labeling conditions and using the same fluorophore as label in our experimental validation. (2) Highly compacted structures, in which the underlying fluorophores are located close to one another, were avoided. In doing so, we wanted to ameliorate the hard to simulate effects of fluorophore quenching on the measured intensity of the complex of interest. (3) For the purpose of validation, the complex of interest would be known to take stable stoichiometries that would not change during the course of an experiment or under slightly different conditions. This is to ensure that our results would, to the best of our knowledge, match those reported. (4) The complex of interest has to be assembled from its individual components *in vitro* and *in situ*. Oligomeric complexes that can be imaged only inside their physiological, cellular environment were excluded as their densities, as well as the behavior of the host cellular system, cannot be appropriately controlled.

https://doi.org/10.1021/acs.jpclett.1c03835
J. Phys. Chem. Lett. 2022, 13, 822–829

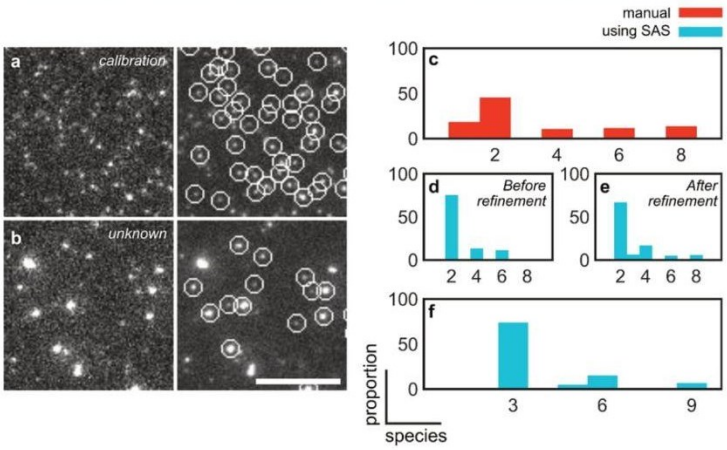

Figure 5. Comparison of subunit counting accuracy with a manual (semiautomated) pipeline and SAS applied on experimental data. (a) Calibration data set of monomeric Bax labeled with ATTO 488 dye. (b) Set of unknown stoichiometries of labeled BAX molecules. Scale bar, 5 μm. Subunit counting of BAX performed (c) manually and using SAS (d) before and (e) after refinement. (f) Subunit counting of Atg9 performed using SAS.

We identified the Bcl-2-associated-X-protein (BAX), which is known to assemble into multiple species based on dimer units,[17] and the lipid scramblase Atg9, which has been recently reported to assemble as a homotrimer,[26−29] as candidate systems. To this end, we reconstituted labeled BAX oligomers into a supported lipid bilayer (SLB) and imaged them under a TIRF microscope (see Methods). We then compared the proportion of species measured using SAS with those measured manually as reported in ref 17 (Figure 5a−e and Figure S3). Our measurements show excellent agreement with those reported, revealing the dimeric stoichiometry of BAX. Moreover, because of the entirely automated pipeline of SAS, it took us 3 min to process one data set, which typically took hours to days to process through the manual selection of clean traces, as well as optimization of detection under various experimental conditions. Similarly, stoichiometry experiments on Atg9 complexes processed by SAS showed excellent agreement with the literature data, with Atg9 assembling predominantly as a trimer [with minor high-order aggregates/complexes based on trimer units (Figure 5f)].

In summary, here we have systematically and extensively assessed the accuracy of subunit counting using brightness analysis. We have established the experimental conditions and assessed complex stoichiometric configurations, under which this method can count with accuracies exceeding 85%. Our analysis serves as an important resource for experimentalists in need of accurately counting the copy number of proteins in a variety of stoichiometric configurations and under a wide range of challenging experimental conditions. To perform this analysis, we developed a fully automated computational pipeline that is simple to use and serves as a fundamental tool for future experiments of this type. We expect our analysis, and software, to empower the use of optical microscopy in structural studies of complex, large, and heterogeneous macromolecular assemblies with single-molecule sensitivity.

■ ASSOCIATED CONTENT

Supporting Information

The Supporting Information is available free of charge at https://pubs.acs.org/doi/10.1021/acs.jpclett.1c03835.

Methods, including simulation of ground-truth data, workflow for single-molecule detection, calibration and particle analysis, and sample preparation for experimental validation; GUI of SAS (Figure S1); gallery of randomly accepted and rejected traces selected by SAS (Figure S2); graphs of the intensity distributions obtained from the experimental data (Figure S3); and stoichiometric configurations and experimental conditions simulated in this study (Table S1) (PDF)

Supplemental data (ZIP)

■ AUTHOR INFORMATION

Corresponding Authors

Katia Cosentino − *Interfaculty Institute of Biochemistry, University of Tübingen, Tübingen 72076, Germany; Department of Biology/Chemistry and Center for Cellular Nanoanalytics (CellNanOs), University of Osnabrück, Osnabrück 49076, Germany;* orcid.org/0000-0002-3796-3500; Email: kacosentino@uni-osnabrueck.de

John S. H. Danial − *Interfaculty Institute of Biochemistry, University of Tübingen, Tübingen 72076, Germany; Yusuf Hamied Department of Chemistry and UK Dementia Research Institute, University of Cambridge, Cambridge CB2 1EW, United Kingdom*; Email: js2494@cam.ac.uk

Ana J. Garcia-Saez − *Interfaculty Institute of Biochemistry, University of Tübingen, Tübingen 72076, Germany; Institute for Genetics and Cologne Excellence Cluster on Cellular Stress Responses in Aging-Associated Diseases (CECAD), Cologne 50931, Germany;* orcid.org/0000-0002-3894-5945; Email: ana.garcia@uni-koeln.de

Authors

Yuri Quintana − *Interfaculty Institute of Biochemistry, University of Tübingen, Tübingen 72076, Germany*

https://doi.org/10.1021/acs.jpclett.1c03835
J. Phys. Chem. Lett. 2022, 13, 822−829

Uris Ros − *Interfaculty Institute of Biochemistry, University of Tübingen, Tübingen 72076, Germany; Institute for Genetics and Cologne Excellence Cluster on Cellular Stress Responses in Aging-Associated Diseases (CECAD), Cologne 50931, Germany*

Raed Shalaby − *Interfaculty Institute of Biochemistry, University of Tübingen, Tübingen 72076, Germany; Institute for Genetics and Cologne Excellence Cluster on Cellular Stress Responses in Aging-Associated Diseases (CECAD), Cologne 50931, Germany*

Eleonora G. Margheritis − *Department of Biology/Chemistry and Center for Cellular Nanoanalytics (CellNanOs), University of Osnabrück, Osnabrück 49076, Germany*

Sabrina Chumpen Ramirez − *Department of Biology/Chemistry and Center for Cellular Nanoanalytics (CellNanOs), University of Osnabrück, Osnabrück 49076, Germany*

Christian Ungermann − *Department of Biology/Chemistry and Center for Cellular Nanoanalytics (CellNanOs), University of Osnabrück, Osnabrück 49076, Germany*

Complete contact information is available at: https://pubs.acs.org/10.1021/acs.jpclett.1c03835

Author Contributions

J.S.H.D. and Y.Q. contributed equally to this work. K.C. and A.J.G.-S. conceived the study. J.S.H.D., Y.Q., A.J.G.-S., and K.C. designed the study with the contributions of U.R. and R.S. K.C. performed BAX experiments. E.G.M. and S.C.R. performed Atg9 experiments. J.S.H.D. and Y.Q. wrote the software. K.C. performed the manual analysis. J.S.H.D. and E.G.M. performed the software analysis. K.C., J.S.H.D., U.R., and R.S. assessed performance. K.C., C.U., and A.J.G.S. provided supervision and infrastructure. All authors contributed to writing the manuscript.

Notes

The authors declare no competing financial interest.

Updated versions of the source code for SAS, as well as guiding instructions, can be obtained from https://github.com/jdanial/SAS.

■ ACKNOWLEDGMENTS

This work was supported by a research associateship from King's College, University of Cambridge, awarded to J.S.H.D., a scholarship from the International Max-Planck Research School and the University of Tubingen awarded to R.S., Deutsche Forschungsgemeinschaft (DFG) Grant UN111/13-1 awarded to C.U., DFG GA164/3-1, starting (Grant 309966) and consolidator (APOSITE) ERC grants awarded to A.J.G.S., and an Elite Postdoctoral Fellowship from the Baden-Wuerttemberg Foundation and DFG Grant INST 190/194-1 awarded to K.C.

■ REFERENCES

(1) Szymborska, A.; de Marco, A.; Daigle, N.; Cordes, V. C.; Briggs, J. A. G.; Ellenberg, J. Nuclear Pore Scaffold Structure Analyzed by Super-Resolution Microscopy and Particle Averaging. *Science* **2013**, *341* (6146), 655−658.

(2) Salvador-Gallego, R.; Mund, M.; Cosentino, K.; Schneider, J.; Unsay, J.; Schraermeyer, U.; Engelhardt, J.; Ries, J.; García-Sáez, A. J. Bax Assembly into Rings and Arcs in Apoptotic Mitochondria Is Linked to Membrane Pores. *EMBO J.* **2016**, *35* (4), 389−401.

(3) Song, L.; Hobaugh, M. R.; Shustak, C.; Cheley, S.; Bayley, H.; Gouaux, J. E. Structure of Staphylococcal α-Hemolysin, a Heptameric Transmembrane Pore. *Science* **1996**, *274* (5294), 1859−1865.

(4) Mund, M.; van der Beek, J. A.; Deschamps, J.; Dmitrieff, S.; Hoess, P.; Monster, J. L.; Picco, A.; Nédélec, F.; Kaksonen, M.; Ries, J. Systematic Nanoscale Analysis of Endocytosis Links Efficient Vesicle Formation to Patterned Actin Nucleation. *Cell* **2018**, *174* (4), 884−896.e17.

(5) Thevathasan, J. V.; Kahnwald, M.; Cieśliński, K.; Hoess, P.; Peneti, S. K.; Reitberger, M.; Heid, D.; Kasuba, K. C.; Hoerner, S. J.; Li, Y.; Wu, Y.-L.; Mund, M.; Matti, U.; Pereira, P. M.; Henriques, R.; Nijmeijer, B.; Kueblbeck, M.; Sabinina, V. J.; Ellenberg, J.; Ries, J. Nuclear Pores as Versatile Reference Standards for Quantitative Superresolution Microscopy. *Nat. Methods* **2019**, *16* (10), 1045−1053.

(6) Rust, M. J.; Bates, M.; Zhuang, X. Sub-Diffraction-Limit Imaging by Stochastic Optical Reconstruction Microscopy (STORM). *Nat. Methods* **2006**, *3* (10), 793−796.

(7) Xu, K.; Zhong, G.; Zhuang, X. Actin, Spectrin, and Associated Proteins Form a Periodic Cytoskeletal Structure in Axons. *Science* **2013**, *339* (6118), 452−456.

(8) Fricke, F.; Beaudouin, J.; Eils, R.; Heilemann, M. One, Two or Three? Probing the Stoichiometry of Membrane Proteins by Single-Molecule Localization Microscopy. *Sci. Rep.* **2015**, *5* (1), 14072.

(9) Hummer, G.; Fricke, F.; Heilemann, M. Model-Independent Counting of Molecules in Single-Molecule Localization Microscopy. *Mol. Biol. Cell* **2016**, *27* (22), 3637−3644.

(10) Karathanasis, C.; Fricke, F.; Hummer, G.; Heilemann, M. Molecule Counts in Localization Microscopy with Organic Fluorophores. *ChemPhysChem* **2017**, *18* (8), 942−948.

(11) Jungmann, R.; Avendaño, M. S.; Dai, M.; Woehrstein, J. B.; Agasti, S. S.; Feiger, Z.; Rodal, A.; Yin, P. Quantitative Super-Resolution Imaging with QPAINT. *Nat. Methods* **2016**, *13* (5), 439−442.

(12) Stein, J.; Stehr, F.; Schueler, P.; Blumhardt, P.; Schueder, F.; Mücksch, J.; Jungmann, R.; Schwille, P. Toward Absolute Molecular Numbers in DNA-PAINT. *Nano Lett.* **2019**, *19* (11), 8182−8190.

(13) Das, S. K.; Darshi, M.; Cheley, S.; Wallace, M. I.; Bayley, H. Membrane Protein Stoichiometry Determined from the Step-Wise Photobleaching of Dye-Labelled Subunits. *ChemBioChem* **2007**, *8* (9), 994−999.

(14) Thompson, J. R.; Cronin, B.; Bayley, H.; Wallace, M. I. Rapid Assembly of a Multimeric Membrane Protein Pore. *Biophys. J.* **2011**, *101* (11), 2679−2683.

(15) Anderluh, A.; Klotzsch, E.; Reismann, A. W. A. F.; Brameshuber, M.; Kudlacek, O.; Newman, A. H.; Sitte, H. H.; Schütz, G. J. Single Molecule Analysis Reveals Coexistence of Stable Serotonin Transporter Monomers and Oligomers in the Live Cell Plasma Membrane*. *J. Biol. Chem.* **2014**, *289* (7), 4387−4394.

(16) Hastie, P.; Ulbrich, M. H.; Wang, H.-L.; Arant, R. J.; Lau, A. G.; Zhang, Z.; Isacoff, E. Y.; Chen, L. AMPA Receptor/TARP Stoichiometry Visualized by Single-Molecule Subunit Counting. *Proc. Natl. Acad. Sci. U. S. A.* **2013**, *110* (13), 5163−5168.

(17) Subburaj, Y.; Cosentino, K.; Axmann, M.; Pedrueza-Villalmanzo, E.; Hermann, E.; Bleicken, S.; Spatz, J.; García-Sáez, A. J. Bax Monomers Form Dimer Units in the Membrane That Further Self-Assemble into Multiple Oligomeric Species. *Nat. Commun.* **2015**, *6* (1), 8042.

(18) Calebiro, D.; Rieken, F.; Wagner, J.; Sungkaworn, T.; Zabel, U.; Borzi, A.; Cocucci, E.; Zürn, A.; Lohse, M. J. Single-Molecule Analysis of Fluorescently Labeled G-Protein−Coupled Receptors Reveals Complexes with Distinct Dynamics and Organization. *Proc. Natl. Acad. Sci. U. S. A.* **2013**, *110* (2), 743−748.

(19) McGuire, H.; Aurousseau, M. R. P.; Bowie, D.; Blunck, R. Automating Single Subunit Counting of Membrane Proteins in Mammalian Cells. *J. Biol. Chem.* **2012**, *287* (43), 35912−35921.

(20) Jenner, A.; Shalaby, R.; Cosentino, K. Chapter Three - Quantitative Single-Molecule Imaging of Protein Assembly in Membranes. In *Advances in Biomembranes and Lipid Self-Assembly*;

Iglič, A., Rappolt, M., García-Sáez, A. J., Eds.; Advances in Biomembranes and Lipid Self-Assembly; Academic Press, 2020; Vol. *31*, pp 81−128. DOI: 10.1016/bs.abl.2020.02.004
(21) Ulbrich, M. H.; Isacoff, E. Y. Subunit Counting in Membrane-Bound Proteins. *Nat. Methods* **2007**, *4* (4), 319−321.
(22) Schmidt, T.; Schütz, G. J.; Gruber, H. J.; Schindler, H. Local Stoichiometries Determined by Counting Individual Molecules. *Anal. Chem.* **1996**, *68* (24), 4397−4401.
(23) Ulbrich, M. H. Counting Molecules: Toward Quantitative Imaging. In *Far-Field Optical Nanoscopy*; Tinnefeld, P., Eggeling, C., Hell, S. W., Eds.; Springer Series on Fluorescence; Springer: Berlin, 2015; pp 263−291.
(24) Xu, J.; Qin, G.; Luo, F.; Wang, L.; Zhao, R.; Li, N.; Yuan, J.; Fang, X. Automated Stoichiometry Analysis of Single-Molecule Fluorescence Imaging Traces via Deep Learning. *J. Am. Chem. Soc.* **2019**, *141* (17), 6976−6985.
(25) Danial, J. S. H.; Shalaby, R.; Cosentino, K.; Mahmoud, M. M.; Medhat, F.; Klenerman, D.; Garcia Saez, A. J. DeepSinse: Deep Learning Based Detection of Single Molecules. *Bioinformatics* **2021**, *37*, 3998.
(26) Matoba, K.; Kotani, T.; Tsutsumi, A.; Tsuji, T.; Mori, T.; Noshiro, D.; Sugita, Y.; Nomura, N.; Iwata, S.; Ohsumi, Y.; Fujimoto, T.; Nakatogawa, H.; Kikkawa, M.; Noda, N. N. Atg9 Is a Lipid Scramblase That Mediates Autophagosomal Membrane Expansion. *Nat. Struct. Mol. Biol.* **2020**, *27* (12), 1185−1193.
(27) Maeda, S.; Yamamoto, H.; Kinch, L. N.; Garza, C. M.; Takahashi, S.; Otomo, C.; Grishin, N. V.; Forli, S.; Mizushima, N.; Otomo, T. Structure, Lipid Scrambling Activity and Role in Autophagosome Formation of ATG9A. *Nat. Struct. Mol. Biol.* **2020**, *27* (12), 1194−1201.
(28) Guardia, C. M.; Tan, X.-F.; Lian, T.; Rana, M. S.; Zhou, W.; Christenson, E. T.; Lowry, A. J.; Faraldo-Gómez, J. D.; Bonifacino, J. S.; Jiang, J.; Banerjee, A. Structure of Human ATG9A, the Only Transmembrane Protein of the Core Autophagy Machinery. *Cell Rep.* **2020**, *31* (13), 107837.
(29) Gómez-Sánchez, R.; Rose, J.; Guimarães, R.; Mari, M.; Papinski, D.; Rieter, E.; Geerts, W. J.; Hardenberg, R.; Kraft, C.; Ungermann, C.; Reggiori, F. Atg9 Establishes Atg2-Dependent Contact Sites between the Endoplasmic Reticulum and Phagophores. *J. Cell Biol.* **2018**, *217* (8), 2743−2763.

https://doi.org/10.1021/acs.jpclett.1c03835
J. Phys. Chem. Lett. 2022, 13, 822−829

Supplementary information

Systematic Assessment of the Accuracy of Subunit Counting in Biomolecular Complexes Using Automated Single Molecule Brightness Analysis

John S H Danial[1,2,3,6]*, Yuri Quintana[1,6], Uris Ros[1,4], Raed Shalaby[1,4], Eleonora G Margheritis[5], Sabrina Chumpen Ramirez [5], Christian Ungermann[5], Ana J Garcia-Saez[1,4]* and Katia Cosentino[1,5]*

[1] Interfaculty Institute of Biochemistry, University of Tübingen, Tübingen 72076, Germany

[2] Yusuf Hamied Department of Chemistry, University of Cambridge, Cambridge CB2 1EW, United Kingdom

[3] UK Dementia Research Institute, University of Cambridge, Cambridge CB2 1EW, United Kingdom

[4] Institute for Genetics and Cologne Excellence Cluster on Cellular Stress Responses in Aging-Associated Diseases (CECAD), Cologne 50931, Germany

[5] Department of Biology/Chemistry and Center for Cellular Nanoanalytics (CellNanOs), University of Osnabrück, Osnabrück 49076, Germany

[6] These authors contributed equally.

* To whom correspondence should be addressed: Katia Cosentino (kacosentino@uni-osnabrueck.de), John S H Danial (js2494@cam.ac.uk) and Ana J Garcia-Saez (ana.garcia@uni-koeln.de)

Methods

Simulating ground-truth data

To simulate the ground-truth data, a pre-set number of particles (i.e. complexes) were randomly scattered across images which are 256 by 256 pixels in size (except for those simulated in **Figures 4c-n** which were 1024 by 2024 pixels in size to accommodate for the larger number of complexes in the same field of view without significantly increasing the density) with pixel size of 100 nm. The standard deviation in the PSF of each particle was fixed at 130 nm. Each complex contained a pre-set number of molecules with intensities sampled from a random number generator based on a normal distribution with a mean intensity of I_m and standard deviation of v, where v is the inter complex variation in the intensity. Each molecule had a photobleaching time that was randomly sampled from 1 to the maximum number of frames which in our simulation was set to 500 frames. The intensity of each molecule was set to the sampled intensity before the photobleaching time point and to 0 afterwards. Each molecule was convoluted with a 2D Gaussian Kernel. To account for the noise statistics of Electron-Multiplying Charge Coupled Detectors (EMCCDs), the produced images in counts I_c were modified as follows:

$$I_e = I_c * QE + DC + RO \tag{1}$$

where I_e is the image signal in electrons, QE is the quantum efficiency, DC is the dark current and RO is the readout noise. The quantum efficiency was set at 95%, dark current was set at 0.0002 electrons/second and readout noise was set to 1 electron. These values are typical of commercially available EMCCDs. To simulate noise, I_e was modified as follows:

$$I_e = gamma\left(I_e, G - 1 + \frac{1}{I_e}\right) + O \tag{2}$$

where G is the camera gain (corrected for conversion factor) and O is the camera bias offset. The gain was set to 58.8 (electron gain of 300 and conversion factor of 5.1) and offset to 100. This noise model was chosen to best replicate the electron-multiplication feature in EMCCDs[1]. The produced images were saved in the big TIFF format at 16 bits for further processing using SAS.

Detecting single molecule using a deep convolutional network

Detection of each complex / molecule was carried out as described in[2]. Briefly, we developed and used DeepSinse, a simple, multi-layer Convolutional Neural Network (CNN) architecture to enable fast detection of single molecules using as few parameters as possible. Our neural network is composed of a CNN, a dense layer and a SoftMax (classification) layer. The neural network was first trained to classify simulated ground-

truth datasets of noise and Gaussian bursts in pre-labelled Regions Of Interest (ROIs), then validated on different, unseen, datasets of pre-labelled ROIs. We then tested it on ground-truth generated ROIs. The neural network is finally deployed by feeding an image into a peak-finding algorithm based on identifying regional maxima. The peak-finding algorithm outputs hundreds of noise- and burst- containing ROIs which are then fed into the trained network for classification, thus, resulting in an annotated image. Burst-containing, and pure-noise, images were simulated with the formers' peak burst intensities varying from 50 to 100 counts corresponding to signal-to-noise ratios from 24.85 to 45.81 and 100 images were simulated with pure noise. Pre-annotated ROIs were picked from each of these images, intensity scaled between 0 and 1 to avoid subjective segmentation parameters such as the intensity threshold, shuffled and fed into the neural network for training. To optimize performance, the neural network was trained using different ROI radii and number of ROIs. The lowest false negative rate FNR (61.45%) and false positive rate FPR (0.3%) were achieved at a ROI radius of 5 pixels and 10,000 training ROIs. The trained network was then integrated into SAS for immediate use. Particles that are less than 6 pixels away from the borders of each image, as well as those which are less than 5 pixels apart from each other are rejected. Finally, the detected particles were fed into a least-squares solver to fit a Gaussian function to the PSF of each particle using the cpufit plugin[3] and extract a value to the standard deviation which was compared to a user-specified value (200 nm for the simulated and experimental data as commonly used in single molecule microscopy[4]). Particles exhibiting a standard deviation value smaller than the user-set value are accepted and, otherwise, rejected. This approach allows for discarding multiple particles present in the same ROI.

Extraction of intensity traces

The intensity of the detected and accepted molecules were extracted from the movies by drawing ROI with a user-specified radius around each of these molecules at each time point. The local background at each time point is calculated by extracting the intensity in a region around the ROI, 2 pixels larger than the ROI. Intensity traces are used for both, the selection of monomeric complexes for calibration (see "Selection of monomeric traces for calibration"), and for the extraction of the intensity value for the detected molecule. In this last case, the maximum intensity of each trace is calculated by taking the median of the first 5 time points of the intensity trace, and the background is subtracted by taking the median of the intensity of the last 5 time points of the background trace (which, theoretically, should yield the same result as the first 5 time points).

Selection of monomeric traces for calibration

The traces extracted for particles belonging to the calibration sample are fed into a trace annotator which calculates the absolute gradient of each intensity trace, normalizes the calculated gradient between 0 and 1 and, finally, extracts the number of peaks in the normalized gradient above a threshold value, known as the minimum peak height, which we set at 0.5 (for simulated data), 0.9 (for experimental data). The value of the minimum peak height was optimized once for each dataset by inspection of the calibration curve so that,

ideally, a single peak corresponding to the monomeric traces was dominant. Gradients with a single peak were chosen as monomeric traces (i.e. arising from a complex with a single molecule).

Calculating the proportion of labelled species

After measuring the intensity for each detected and accepted particle (measured as described in "Extraction of intensity traces"), a kernel probability distribution function (pdf) with a bandwidth of 5 photons was calculated from the intensity values of the calibration species and normalized between 0 and 1. A peak finder was subsequently used to find peaks in the normalized kernel pdf with a minimum height of 0.8 (normalized value). The first peak, corresponding to the intensity distribution of monomers, was selected and its mean intensity value (I_m) was used to fit the following Gaussian Mixture Model (GMM) using a non-linear curve fitting solver to the kernel pdf to extract the standard deviation in the intensity values of the population of monomers (σ_m):

$$f(I) = \sum_{n=1}^{n} \quad a_i e^{-\left(\frac{I-I_i}{2\sigma_i}\right)^2} \tag{3}$$

Where $a_i, I_i and\ \sigma_i$ are the amplitude, mean intensity value and standard deviation in intensity value of each Gaussian. n is the number of Gaussians and was set to 2 to account for any dimers present in the sample used for calibration. In this case, $I_m \stackrel{\text{def}}{=} I_1$ and $\sigma_m \stackrel{\text{def}}{=} \sigma_1$. Following, a kernel pdf was constructed from the sample of unknown species with a bandwidth of 5 photons which was fit, using a non-linear curve fitting solver, with an idealized GMM:

$$f(I) = \sum_{n=1}^{n_{max}} \quad \frac{p_i}{\sigma_m\sqrt{2\pi n}} e^{-\left(\frac{I-(I_m n)}{2\sigma_m\sqrt{n}}\right)^2} \tag{4}$$

Where p_i is the proportion of each species corresponding to the area below each Gaussian curve and n_{max} is the maximum number of Gaussians. n_{max} was calculated as described in[22] from I_m and σ_m using the following formula:

$$n_{max} = floor\left[\left(\frac{I_m}{\sigma_m}\right)^2\right] \tag{5}$$

Constraining the maximum number of Gaussians as such does not prevent overfitting. To account for overfitting, we performed non-linear curve fitting with n from 1 to n_{max}. In each time we performed a fit, we calculated the root sum squared residual and whenever this was less than 95% of the minimum calculated value, this last was set as the minimum value and the used number of Gaussians as n_{max}. Finally, an optional

refinement step was performed were I_m was scanned in a $\pm$ 10 photons region with 1 photon resolution and modified to where the root sum squared residual was minimized.

The residual error is calculated in an ascending order of Gaussians. The minimum residual error is also calculated in that specific order. For configurations where the proportion of species decreases with increasing the species number (as in figure 3h) a minimum residual error is reached with low species numbers which have higher proportions. This is not the case with configurations where the proportion of species increases with increasing the specie number (as in figure 3i).

Correcting for labelling efficiency to calculate the true proportion of labelled and unlabelled species

Labelling efficiency was corrected for as described in[5]. Briefly, each molecule was assumed to be either labelled (1) or not labelled (0). To uncover the true proportion of species from those measured above, we constructed a binomial probability distribution function of the following form:

$$f(n,p) = \binom{n}{x} p^x q^{n-x} I_{0,1,\ldots,n}(x) \tag{6}$$

Where x is the species number, n is the number of trials, p is the probability of a molecule being labelled (set to the labelling efficiency) and q is the probability of a molecule not being labelled ($= 1 - p$). x and n took values from 1 to the number of measured species. A linear least-squares problem solver was then used to calculate the true proportion of species taking the constructed binomial probability distribution function as the multiplier matrix and the measured proportion of species as the constant vector. The solver was constrained between 0 and 100% across all species.

Preparing BAX reference sample and imaging setup used for experimental validation

The sample was prepared as described in[5]. Briefly, egg phosphatidylcholine and cardiolipin (Avanti Polar Lipids, US) were mixed in a 7:3 ratio and dissolved in chloroform that was evaporated under reduced pressure for 3 hours. The lipid film was then resuspended with 150 mM NaCl, 10 mM Hepes (pH7.4) to a final concentration of 1 mg/mL. The lipid solution was subjected to five cycles of freezing and thawing after which they were manually extruded through a polycarbonate membrane with a defined pore size (100 nm) using glass syringes. The formed large unilamellar vesicles (LUVs) were then incubated with 10 nM Atto488 labelled Bax (labelling efficiency 84%) for 1 hour at 43°C to give proteoliposomes which were subsequently diluted 1:10 with untreated liposomes. The supported lipid bilayer (SLB) was formed by incubating the diluted proteoliposomes on a glass slide, previously cleaned with a piranha solution, at 37 °C for 2 minutes in the presence of 3 mM $CaCl_2$ and then washed several times with 150 mM NaCl, 10 mM Hepes (pH7.4) to remove non-fused vesicles. Samples were imaged on the setup described below for a total of 1200 frames under a 35 ms exposure time and 25 ms delay between frames with a power density of ~ 1 kW/cm^2.

The sample was imaged on a Total Internal Reflection Fluorescence (TIRF) microscope. The laser excitation from a 4-wavelengths (405 nm, 488 nm, 561 nm and 647 nm) laser engine (iChrome MLE, Toptica Photonics AG, DE) was coupled into a multi-mode fibre onto a TIRF-alignment module (Laser TIRF 3, Carl Zeiss AG, DE) inserted into the side port of an upright microscope (Axiovert 200, Carl Zeiss AG). Using the TIRF-alignment module, the excitation light was focused onto the back focal plane of a 100x, 1.46 Numerical Aperture (NA) objective (Apo-TIRF, Carl Zeiss AG) after passing through a triple-band clean-up filter (TBP 483 + 564 + 642 (HE), Carl Zeiss AG) and being reflected off a quad-band dichroic filter (TFT 506 + 582 + 659 (HE), Carl Zeiss AG). Image was additionally magnified by 1.6x to obtain a final pixel size of 100 nm. The emission was collected using the same objective, passed through a triple-band emission filter (TBP 526 + 601 + 688 (HE), Carl Zeiss AG) and focused on an EMCCD camera (iXon 88X, Andor, IE) cooled at -70 degC.

Preparing Atg9 reference sample and imaging setup used for experimental validation

Atg9 was overexpressed in yeast as GFP-3xFLAG fusion protein and purified as previously described[6]. For the generation of Atg9 containing liposomes or protein free liposomes, 50% DOPC, 30% DOPE and 20% DOPS (Avanti Polaris) were mixed and dried under vacuum 1h at 37°C. The lipid film was resuspended in buffer A (300 mM KCl, 50 mM HEPES, pH 7.4) to a concentration of 20 mg/ml and sonicated 15 min. Generated SUVs were destabilized by adding 35 mM CHAPS followed by incubation 1h at 23°C. 1.5mg of lipids were mixed with 10 µg of the purified protein or with lysis buffer (for protein free liposomes) and the mixes were incubated 1h at 4°C. Then, samples were diluted 10 times in buffer A to reduce the concentration of detergent below the critical micelle concentration (CMC). Samples were dialyzed using Slide-A-Lyzer dialysis cassettes 20 MWCO (Thermo Scientific) against buffer A plus 0.2 g of Bio-beads SM2 adsorbent Media (BIO-RAD) per liter of buffer. Reconstituted liposomes were freeze-thawed two times. The SLB was formed by incubating 1:10 diluted proteoliposomes on a glass slide, cleaned with a piranha solution, at 37°C for 10min with 3mM $CaCl_2$, and washed 15 times with 150 mM NaCl, 10mM Hepes (pH7.4) buffer to remove non-fused vesicles.

Samples were imaged on a custom-designed TIRF microscope for a total of 2000 frames under a 30 ms exposure time. Laser excitation from a 488 nm laser, max. power 400 mW (Sapphire, Coherent) was coupled into a single mode polarization maintaining fiber to a TIRF module connected to an Olympus IX83 inverted microscope with hardware autofocus system (IX3-ZDC, Olympus) and 100x oil-immersion objective ((UPLAPO100xOHR). Image was additionally magnified by 1.6x (IX3-CAS, Olympus) to obtain a final magnification of 160x and a pixel size of 100 nm. Fluorescence was filtered by a four-line polychroic mirror (zt405/488/561/640rpc, Chroma, 3 mm) and rejection band filter (zet405/488/561/647 TIRF, Chroma), and the emission was focussed on an iXon Ultra EMCCD Camera (Andor Technologies).

Supplementary Figure 1

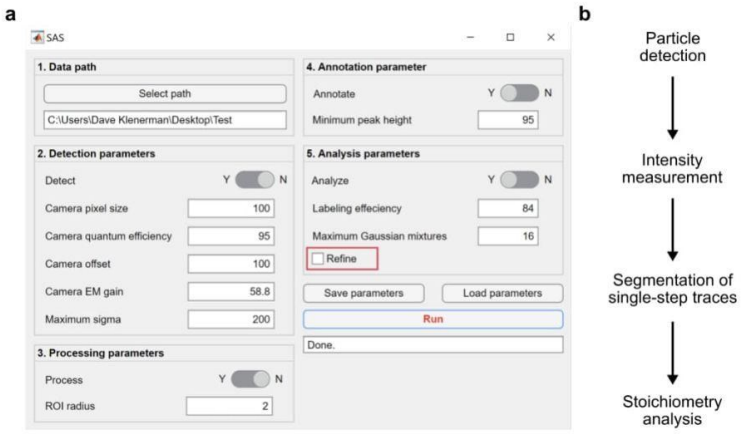

Figure S1. (a) Graphical user interface (GUI) of SAS. The GUI is divided into five panels: 1. Data import; 2. Detection parameters to be fed with the experimental parameters used by the experimenter during data acquisition; 3. Processing parameters that allows the user to select the ROI radius based on the experimental parameters used; 4. Annotation of parameters in a text file and choice of the threshold value (minimum peak height) for appropriate monomeric curves selection; 5. Analysis parameters that allow to introduce the values of the protein labelling efficiency and of the maximum number of Gaussian mixtures the user aims to resolve. Importantly, the refinement step can be selected in this panel (red box). (b) SAS workflow.

Supplementary Figure 2

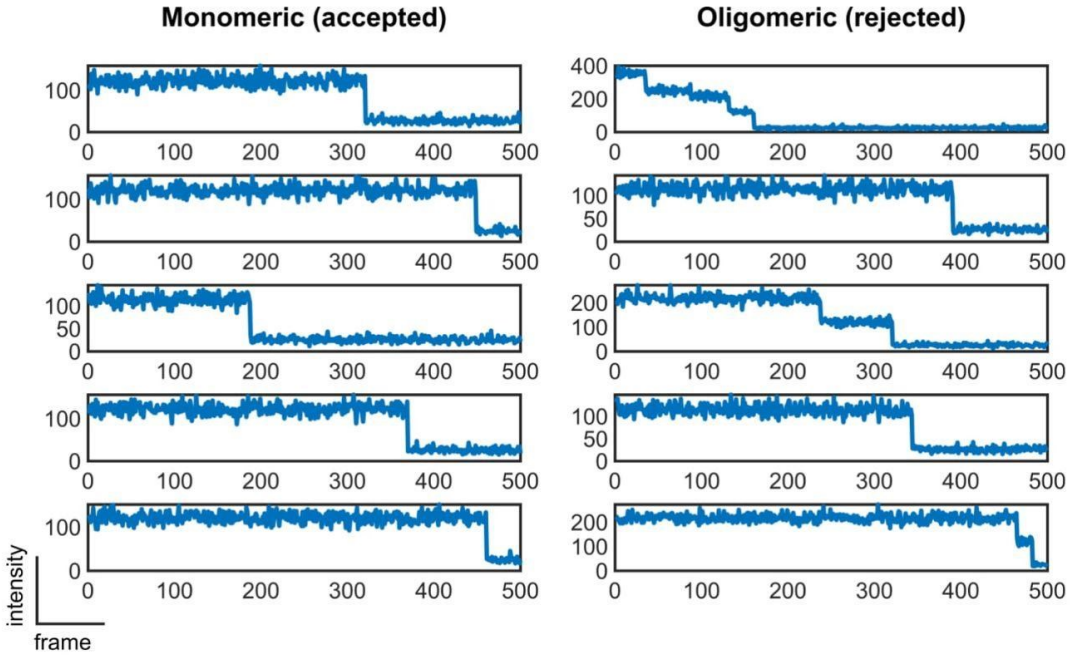

Figure S2. Gallery of randomly accepted (monomeric) and rejected (oligomeric) traces selected by the trace annotator tool of SAS.

Supplementary Figure 3

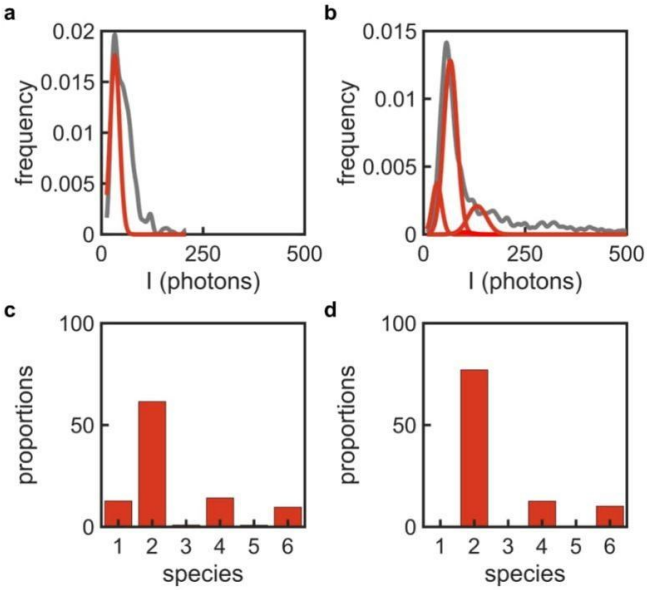

Figure S3. Graphs of the (a) calibration, and (b) unknown ~~(c)~~ intensity distributions obtained from the experimental data to measure the stoichiometry of BAX complexes. Percentage of occurrence of Bax species (c) before~~,~~ and (d) after labelling correction (labelling efficiency 84%). Illustrated data are without refinement. Results after refinement are shown in figure 5.

Supplementary Table 1

Figure	Stoichiometric configuration Experimental conditions (if applicable) Reference in supplementary data / reference dataset
Figure 2a	Calibration: 1-mer (50%), 2-mer (25%), 3-mer (25%) [varied from 20 to 320 particles per movie] Unknown: 1-mer (50%), 2-mer (50%) [varied from 20 to 320 particles per movie]
	# frames = 500, # movies = 10, max. photon count = 10, variation in photon count = 0%, lateral sigma = 130 nm, frame size = 256 pixels x 256 pixels
	Columns A to O / dataset # 2 to 5
Figure 2b	Calibration: 1-mer (50%), 2-mer (25%), 3-mer (25%) [80 particles per movie] Unknown: 1-mer (50%), 2-mer (50%) [80 particles per movie]
	# frames = 500, # movies = 10, max. photon count = 2 to 50, variation in photon count = 0%, lateral sigma = 130 nm, frame size = 256 pixels x 256 pixels
	Columns P to AI / dataset # 6 to 10
Figure 2c	Calibration: 1-mer (50%), 2-mer (25%), 3-mer (25%) [80 particles per movie] Unknown: varied from 1-mer (50%), 2-mer (50%) [80 particles per movie] to 1-to-16-mers (3.125% each)
	# frames = 500, # movies = 10, max. photon count = 10, variation in photon count = 0%, lateral sigma = 130 nm, frame size = 256 pixels x 256 pixels
	Columns AJ to BC / dataset # 11 to 14
Figure 2d	Calibration: 1-mer (50%), 2-mer (25%), 3-mer (25%) [80 particles per movie] Unknown: 1-mer (50%), 2-mer (50%) [80 particles per movie]
	# frames = 500, # movies = varied from 5 to 40, max. photon count = 10, variation in photon count = 0%, lateral sigma = 130 nm, frame size = 256 pixels x 256 pixels
	Columns BD to BW / dataset # 15 to 18
Figure 2e	Calibration: 1-mer (50%), 2-mer (25%), 3-mer (25%) [80 particles per movie] Unknown: 1-mer (50%), 2-mer (50%) [80 particles per movie]
	# frames = 500, # movies = 10, max. photon count = 10, variation in photon count = 0% to 50%, lateral sigma = 130 nm, frame size = 256 pixels x 256 pixels
	Columns BX to CL / dataset # 19 to 22
Figure 2f	Calibration: 1-mer (50%), 2-mer (25%), 3-mer (25%) [80 particles per movie] Unknown: 1-mer (50%), 2-mer (50%) [80 particles per movie]
	# frames = 500, # movies = 10, max. photon count = 10, variation in photon count = 0%, lateral sigma = 130 nm, frame size = 256 pixels x 256 pixels. Analysis bin sized varied from 1 to 20.
	Columns HP to IR / dataset # 45 to 49
Figure 2g	Calibration: 1-mer (50%), 2-mer (25%), 3-mer (25%) [80 particles per movie] Unknown: 1-mer (50%), 2-mer (50%) [80 particles per movie]
	# frames = 500, # movies = 10, max. photon count = 10, variation in photon count = 0%, lateral sigma = varied from 100 nm to 200 nm, frame size = 256 pixels x 256 pixels
	Columns CM to DA / dataset # 23 to 25
Figure 2h	Calibration: 1-mer (50%), 2-mer (25%), 3-mer (25%) [80 particles per movie] Unknown: 1-mer (50%), 2-mer (50%) [80 particles per movie]
	# frames = 500, # movies = 10, max. photon count = 10, variation in photon count = 0%, lateral sigma = 130 nm, frame size = 256 pixels x 256 pixels, pixel size varied from 100 nm to 160 nm.
	Columns IT to JJ / dataset # 50 to 52
Figure 3a	Calibration: 1-mer (50%), 2-mer (25%), 3-mer (25%) [80 particles per movie] Unknown: 1-to-12-mers (8.33% each) [96 particles per movie]

	# frames = 500, # movies = 10, max. photon count = 10, variation in photon count = 0%, lateral sigma = 130 nm, frame size = 256 pixels x 256 pixels
	Columns DB to DF / dataset # 26
Figure 3b	Calibration: 1-mer (50%), 2-mer (25%), 3-mer (25%) [80 particles per movie] Unknown: 1,3,5,7,9 and 11-mers (16.67% each) [96 particles per movie]
	# frames = 500, # movies = 10, max. photon count = 10, variation in photon count = 0%, lateral sigma = 130 nm, frame size = 256 pixels x 256 pixels
	Columns DG to DK / dataset # 27
Figure 3c	Calibration: 1-mer (50%), 2-mer (25%), 3-mer (25%) [80 particles per movie] Unknown: 1,4,7 and 10-mers (25% each) [96 particles per movie]
	# frames = 500, # movies = 10, max. photon count = 10, variation in photon count = 0%, lateral sigma = 130 nm, frame size = 256 pixels x 256 pixels
	Columns DL to DP / dataset # 28
Figure 3d	Calibration: 1-mer (50%), 2-mer (25%), 3-mer (25%) [80 particles per movie] Unknown: 1,5 and 9-mers (33.33% each) [96 particles per movie]
	# frames = 500, # movies = 10, max. photon count = 10, variation in photon count = 0%, lateral sigma = 130 nm, frame size = 256 pixels x 256 pixels
	Columns DQ to DU / dataset # 29
Figure 3e	Calibration: 1-mer (50%), 2-mer (25%), 3-mer (25%) [80 particles per movie] Unknown: 1 and 7-mers (50% each) [96 particles per movie]
	# frames = 500, # movies = 10, max. photon count = 10, variation in photon count = 0%, lateral sigma = 130 nm, frame size = 256 pixels x 256 pixels
	Columns DV to DZ / dataset # 30
Figure 3f	Calibration: 1-mer (50%), 2-mer (25%), 3-mer (25%) [80 particles per movie] Unknown: 1-mer (15.38%), 2-mer (14.10%), 3-mer (12.82%), 4-mer (11.54%), 5-mer (10.26%), 6-mer (8.97%), 7-mer (7.69%), 8-mer (6.41%), 9-mer (5.13%), 10-mer (3.85%), 11-mers (2.56% each) and 12-mer (1.28%) [312 particles per movie]
	# frames = 500, # movies = 10, max. photon count = 10, variation in photon count = 0%, lateral sigma = 130 nm, frame size = 256 pixels x 256 pixels
	Columns EA to EE / dataset # 31
Figure 3g	Calibration: 1-mer (50%), 2-mer (25%), 3-mer (25%) [80 particles per movie] Unknown: 1-mer (1.28%), 2-mer (2.56%), 3-mer (3.85%), 4-mer (5.13%), 5-mer (6.41%), 6-mer (7.69%), 7-mer (8.97%), 8-mer (10.26%), 9-mer (11.54%), 10-mer (12.82%), 11-mers (14.10% each) and 12-mer (15.38%) [312 particles per movie]
	# frames = 500, # movies = 10, max. photon count = 10, variation in photon count = 0%, lateral sigma = 130 nm, frame size = 256 pixels x 256 pixels
	Columns EF to EJ / dataset # 32
Figure 3h	Calibration: 1-mer (50%), 2-mer (25%), 3-mer (25%) [80 particles per movie] Unknown: 1-mer (28.57%), 3-mer (23.81%), 5-mer (19.10%), 7-mer (14.29%), 9-mer (9.52%) and 11-mer (4.76%) [168 particles per movie]
	# frames = 500, # movies = 10, max. photon count = 10, variation in photon count = 0%, lateral sigma = 130 nm, frame size = 256 pixels x 256 pixels
	Columns EK to EO / dataset # 33
Figure 3i	Calibration: 1-mer (50%), 2-mer (25%), 3-mer (25%) [80 particles per movie] Unknown: 2-mer (4.76%), 4-mer (9.52%), 6-mer (14.29%), 8-mer (19.05%), 10-mer (23.81%) and 12-mer (28.57%) [168 particles per movie]
	# frames = 500, # movies = 10, max. photon count = 10, variation in photon count = 0%, lateral sigma = 130 nm, frame size = 256 pixels x 256 pixels
	Columns EP to ET / dataset # 34
Figure 4a	Calibration: 1-mer (50%), 2-mer (25%), 3-mer (25%) [80 particles per movie]

	Unknown: 1-mer (15.38%), 2-mer (14.10%), 3-mer (12.82%), 4-mer (11.54%), 5-mer (10.26%), 6-mer (8.97%), 7-mer (7.69%), 8-mer (6.41%), 9-mer (5.13%), 10-mer (3.85%), 11-mers (2.56% each) and 12-mer (1.28%) [312 particles per movie]
	# frames = 500, # movies = 10, max. photon count = 5, variation in photon count = 20%, lateral sigma = 130 nm, frame size = 1,024 pixels x 1,024 pixels
	Columns EV to EZ (rows 1 to 14) / dataset # 31 copy
Figure 4b	Calibration: 1-mer (50%), 2-mer (25%), 3-mer (25%) [80 particles per movie] Unknown: 1-mer (28.57%), 3-mer (23.81%), 5-mer (19.10%), 7-mer (14.29%), 9-mer (9.52%) and 11-mer (4.76%) [168 particles per movie]
	# frames = 500, # movies = 10, max. photon count = 5, variation in photon count = 20%, lateral sigma = 130 nm, frame size = 1,024 pixels x 1,024 pixels
	Columns FB to FF (rows 1 to 14) / dataset # 33 copy
Figure 4c	Calibration: 1-mer (50%), 2-mer (25%), 3-mer (25%) [80 particles per movie] Unknown: 1-mer (15.38%), 2-mer (14.10%), 3-mer (12.82%), 4-mer (11.54%), 5-mer (10.26%), 6-mer (8.97%), 7-mer (7.69%), 8-mer (6.41%), 9-mer (5.13%), 10-mer (3.85%), 11-mers (2.56% each) and 12-mer (1.28%) [312 particles per movie]
	# frames = 500, # movies = 10, max. photon count = 5, variation in photon count = 20%, lateral sigma = 130 nm, frame size = 1,024 pixels x 1,024 pixels
	Columns EV to EZ (rows 22 to 34) / dataset # 31 copy (2)
Figure 4d	Calibration: 1-mer (50%), 2-mer (25%), 3-mer (25%) [80 particles per movie] Unknown: 1-mer (11.76%), 2-mer (11.03%), 3-mer (10.29%), 4-mer (9.56%), 5-mer (8.82%), 6-mer (8.09%), 7-mer (7.35%), 8-mer (6.62%), 9-mer (5.88%), 10-mer (5.15%), 11-mers (4.41%), 12-mer (3.68%), 13-mer (2.94%), 14-mer (2.21%), 15-mer (1.47%) and 16-mer (0.74%) [544 particles per movie]
	# frames = 500, # movies = 10, max. photon count = 5, variation in photon count = 20%, lateral sigma = 130 nm, frame size = 1,024 pixels x 1,024 pixels
	Columns FH to FL / dataset # 35
Figure 4e	Calibration: 1-mer (50%), 2-mer (25%), 3-mer (25%) [80 particles per movie] Unknown: 1-mer (9.52%), 2-mer (9.05%), 3-mer (8.57%), 4-mer (8.10%), 5-mer (7.62%), 6-mer (7.14%), 7-mer (6.67%), 8-mer (6.19%), 9-mer (5.71%), 10-mer (5.24%), 11-mers (4.76%), 12-mer (4.29%), 13-mer (3.81%), 14-mer (3.33%), 15-mer (2.86%), 16-mer (2.38%), 17-mer (1.90%), 18-mer (1.43%), 19-mer (0.95%), 20-mer (0.47%) [840 particles per movie]
	# frames = 500, # movies = 10, max. photon count = 5, variation in photon count = 20%, lateral sigma = 130 nm, frame size = 1,024 pixels x 1,024 pixels
	Columns FN to FR / dataset # 36
Figure 4f	Calibration: 1-mer (50%), 2-mer (25%), 3-mer (25%) [80 particles per movie] Unknown: 1-mer (8%), 2-mer (7.67%), 3-mer (7.33%), 4-mer (7%), 5-mer (6.67%), 6-mer (6.33%), 7-mer (6%), 8-mer (5.67%), 9-mer (5.33%), 10-mer (5%), 11-mers (4.67%), 12-mer (4.33%), 13-mer (4%), 14-mer (3.67%), 15-mer (3.33%), 16-mer (3%), 17-mer (2.67%), 18-mer (2.33%), 19-mer (2%), 20-mer (1.67%), 21-mer (1.33%), 22-mer (1%), 23-mer (0.67%), 24-mer (0.33%) [1200 particles per movie]
	# frames = 500, # movies = 10, max. photon count = 5, variation in photon count = 20%, lateral sigma = 130 nm, frame size = 1,024 pixels x 1,024 pixels
	Columns FT to FX / dataset # 37
Figure 4g	Calibration: 1-mer (50%), 2-mer (25%), 3-mer (25%) [80 particles per movie] Unknown: 1-mer (28.57%), 3-mer (23.81%), 5-mer (19.10%), 7-mer (14.29%), 9-mer (9.52%) and 11-mer (4.76%) [168 particles per movie]
	# frames = 500, # movies = 10, max. photon count = 5, variation in photon count = 20%, lateral sigma = 130 nm, frame size = 1,024 pixels x 1,024 pixels
	Columns EV to EZ (rows 22 to 34) / dataset # 33 copy (2)
Figure 4h	Calibration: 1-mer (50%), 2-mer (25%), 3-mer (25%) [80 particles per movie]

	Unknown: 1-mer (22.22%), 3-mer (19.44%), 5-mer (16.67%), 7-mer (13.89%) 9-mer (11.11%), 11-mer (8.33%), 13-mer (5.56%) and 15-mer (2.78%) [288 particles per movie]
	# frames = 500, # movies = 10, max. photon count = 5, variation in photon count = 20%, lateral sigma = 130 nm, frame size = 1,024 pixels x 1,024 pixels
	Columns FZ to GD / dataset # 38
Figure 4i	Calibration: 1-mer (50%), 2-mer (25%), 3-mer (25%) [80 particles per movie] Unknown: 1-mer (18.18%), 3-mer (16.36%), 5-mer (15.55%), 7-mer (12.73%) 9-mer (10.91%), 11-mer (9.09%), 13-mer (7.27%), 15-mer (5.45%), 17-mer (3.64%) and 19-mer (1.82%) [440 particles per movie]
	# frames = 500, # movies = 10, max. photon count = 5, variation in photon count = 20%, lateral sigma = 130 nm, frame size = 1,024 pixels x 1,024 pixels
	Columns GF to GJ / dataset # 39
Figure 4j	Calibration: 1-mer (50%), 2-mer (25%), 3-mer (25%) [80 particles per movie] Unknown: 1-mer (15.38%), 3-mer (14.10%), 5-mer (12.82%), 7-mer (11.54%) 9-mer (10.26%), 11-mer (8.97%), 13-mer (7.69%), 15-mer (6.41%), 17-mer (5.13%), 19-mer (3.84%), 21-mer (2.56%) and 23-mer (1.28%) [624 particles per movie]
	# frames = 500, # movies = 10, max. photon count = 5, variation in photon count = 20%, lateral sigma = 130 nm, frame size = 1,024 pixels x 1,024 pixels
	Columns GL to GP / dataset # 40
Figure 4k	Calibration: 1-mer (50%), 2-mer (25%), 3-mer (25%) [80 particles per movie] Unknown: 1-mer (40%), 4-mer (30%), 7-mer (20%) and 10-mer (10%) [120 particles per movie]
	# frames = 500, # movies = 10, max. photon count = 5, variation in photon count = 20%, lateral sigma = 130 nm, frame size = 1,024 pixels x 1,024 pixels
	Columns GR to GV / dataset # 41
Figure 4l	Calibration: 1-mer (50%), 2-mer (25%), 3-mer (25%) [80 particles per movie] Unknown: 1-mer (31.37%), 4-mer (25.49%), 7-mer (19.61%), 10-mer (13.73%), 13-mer (7.84%) and 16-mer (1.96%) [204 particles per movie]
	# frames = 500, # movies = 10, max. photon count = 5, variation in photon count = 20%, lateral sigma = 130 nm, frame size = 1,024 pixels x 1,024 pixels
	Columns GX to HB / dataset # 42
Figure 4m	Calibration: 1-mer (50%), 2-mer (25%), 3-mer (25%) [80 particles per movie] Unknown: 1-mer (25.97%), 4-mer (22.08%), 7-mer (18.18%), 10-mer (14.29%), 13-mer (10.39%), 16-mer (6.49%) and 19-mer (2.60%) [308 particles per movie]
	# frames = 500, # movies = 10, max. photon count = 5, variation in photon count = 20%, lateral sigma = 130 nm, frame size = 1,024 pixels x 1,024 pixels
	Columns HD to HH / dataset # 43
Figure 4n	Calibration: 1-mer (50%), 2-mer (25%), 3-mer (25%) [80 particles per movie] Unknown: 1-mer (22.22%), 4-mer (19.44%), 7-mer (16.67%), 10-mer (13.89%), 13-mer (11.11%), 16-mer (8.33%), 19-mer (5.56%), 22-mer (2.78%) [432 particles per movie]
	# frames = 500, # movies = 10, max. photon count = 5, variation in photon count = 20%, lateral sigma = 130 nm, frame size = 1,024 pixels x 1,024 pixels
	Columns HJ to HN / dataset # 44

Supplementary Table S1 Information on the stoichiometric configurations and experimental conditions simulated in this study.

References

(1) Hirsch, M.; Wareham, R. J.; Martin-Fernandez, M. L.; Hobson, M. P.; Rolfe, D. J. A Stochastic Model for Electron Multiplication Charge-Coupled Devices – From Theory to Practice. *PLOS ONE* **2013**, *8* (1), e53671. DOI: 10.1371/journal.pone.0053671.
(2) Danial, J. S. H.; Shalaby, R.; Cosentino, K.; Mahmoud, M. M.; Medhat, F.; Klenerman, D.; Garcia Saez, A. J. DeepSinse: deep learning-based detection of single molecules. *Bioinformatics* **2021**. DOI: 10.1093/bioinformatics/btab352 (acccessed 7/17/2021).
(3) Przybylski, A.; Thiel, B.; Keller-Findeisen, J.; Stock, B.; Bates, M. Gpufit: An open-source toolkit for GPU-accelerated curve fitting. *Scientific Reports* **2017**, *7* (1), 15722. DOI: 10.1038/s41598-017-15313-9.
(4) Thevathasan, J. V.; Kahnwald, M.; Cieśliński, K.; Hoess, P.; Peneti, S. K.; Reitberger, M.; Heid, D.; Kasuba, K. C.; Hoerner, S. J.; Li, Y.; et al. Nuclear pores as versatile reference standards for quantitative superresolution microscopy. *bioRxiv* **2019**, 582668. DOI: 10.1101/582668.
(5) Subburaj, Y.; Cosentino, K.; Axmann, M.; Pedrueza-Villalmanzo, E.; Hermann, E.; Bleicken, S.; Spatz, J.; García-Sáez, A. J. Bax monomers form dimer units in the membrane that further self-assemble into multiple oligomeric species. *Nature Communications* **2015**, *6* (1), 8042. DOI: 10.1038/ncomms9042.
(6) Gómez-Sánchez, R.; Rose, J.; Guimarães, R.; Mari, M.; Papinski, D.; Rieter, E.; Geerts, W. J.; Hardenberg, R.; Kraft, C.; Ungermann, C.; et al. Atg9 establishes Atg2-dependent contact sites between the endoplasmic reticulum and phagophores. *The Journal of cell biology* **2018**, *217* (8), 2743-2763. DOI: 10.1083/jcb.201710116 PubMed.